The investigation of negative thermal expansion and magnetic structure in $La_{0.5}Ba_{0.5}CoO_{3-x}$ by neutron powder diffraction

Zhijian TAN

Doctor of Philosophy

Department of Materials Structure Science
School of High Energy Accelerator Science
SOKENDAI (The Graduate University for Advanced Studies)

THESIS

The investigation of negative thermal expansion and magnetic structure in $La_{0.5}Ba_{0.5}CoO_{3-x}$ by neutron powder diffraction

Zhijian TAN

DOCTOR OF PHILOSOPHY

Department of Materials Structure Science
School of High Energy Accelerator Science
SOKENDAI (The Graduate University for Advanced Studies)

2018

The investigation of negative thermal expansion and magnetic structure in $La_{0.5}Ba_{0.5}CoO_{3-x}$ by neutron powder diffraction

(負の熱膨張を示す $La_{0.5}Ba_{0.5}CoO_{3-x}$ の結晶構造と磁気構造の研究)

Abstract:

Negative thermal expansion (NTE) describes the phenomenon of lattice contraction as temperature increase. Since thermal expansion may cause significant problems in engineering fields, NTE is very important for industrial application, from large structural components such as railroad tracks and bridges, to precision instruments and electronic devices such as optical instruments and sensors [1, 2]. Recently, our group observed large NTE in cobaltite perovskite, $PrBaCo_2O_{5.74}$ below Neel temperature T_N=120 K [3]. Moreover, NTE in $PrBaCo_2O_{5.5+x}$ can be tuned by changing the hole doping level x. Through the comprehensive study with multiple techniques, it is found this NTE is closely associated with the ferromagnetic (FM) and antiferromagnetic (AFM) competition. Now I am motivated to investigate NTE in the A-site disordered $La_{0.5}Ba_{0.5}CoO_{3-x}$. Firstly, the isotropic NTE is more important for industry application, since for the anisotropic NTE, microcracking may occur during repeated thermal cycling. In contrast to the anisotropic NTE in A-site ordered $PrBaCo_2O_{5.5+x}$, the NTE in A-site disorder $La_{0.5}Ba_{0.5}CoO_{3-x}$ is isotropic owing to the cubic crystal structure. Furthermore, from Tokura's report [4] A-site disordered can enhance phase fluctuation, even lead to phase separation, which shows that A-site ordering imposes significant effect on the competition strength. Therefore, in this research I study the A-site disordered $La_{0.5}Ba_{0.5}CoO_{3-x}$ and compare with the A-site ordered counterpart. By investigating the A-site disordered effect on the NTE in the cobaltite perovskite, I expect to obtain deeper understanding of the microscopic origin of NTE in this cobaltite.

This thesis is concerned with sample synthesis and investigation of magnetic structure and NTE property of the A-site disordered $La_{0.5}Ba_{0.5}CoO_{3-x}$. The present thesis contains five chapters. In the first chapter the application of NTE material as well as the common NTE material are introduced. Then the detailed properties and magnetism of NTE are reviewed. This chapter also includes the structure and the unusual properties of the cobaltite perovskites.

For the second chapter the focus changes to the experimental part. I prepared high-quality $La_{0.5}Ba_{0.5}CoO_{3-x}$ polycrystalline samples by solid-state reaction method and controlled the oxygen content by annealing as-synthesized sample in pure Ar atmosphere at various temperatures. The oxygen content is determined by the iodometric titration method. A combination of X-ray powder diffraction (XRD), high resolution neutron powder diffraction (NPD) and the superconducting quantum interference device (SQUID) magnetometer (MPMS) was used to investigate the crystal structure and magnetic structure.

In the third chapter, the experiment results are presented. The crystal and magnetic structures are determined by the Z-Rietveld refinement. Based on the magnetization data and NPD data, the phase diagram of this $La_{0.5}Ba_{0.5}CoO_{3-x}$ is obtained. From the temperature dependence of volume, the large NTE is observed in the hole doping A-site disordered $La_{0.5}Ba_{0.5}CoO_{3-x}$. This NTE can be tuned by changing the oxygen content and the largest NTE occurs near the boundary between FM and AFM phases in the phase diagram. The phase separation of AFM and FM state or paramagnetic (PM) state was observed in very large range of oxygen content from 2.82 to 2.89. It is found that this NTE is related to the magnetic ordering. The transition of LV phase with AFM state to SV phase with FM or paramagnetic state results in the NTE. The results of NPD under magnetic field confirm that the large volume (LV) phase is related to the AFM and small volume (SV) phase is related to the FM. It is also found that the average volume is suppressed under magnetic field, which reveals that the NTE can be tuned by the magnetic field.

In the fourth chapter, I discuss about the new phenomenon of this sample. From the phase diagram of $La_{0.5}Ba_{0.5}CoO_{3-x}$ and $Pr_{0.5}Ba_{0.5}CoO_{3-x}$, the phase separation is observed in a much larger range of oxygen content from 2.82 to 2.89 in $La_{0.5}Ba_{0.5}CoO_{3-x}$. The Curie temperatures T_C of the two samples are very close while the T_N in $La_{0.5}Ba_{0.5}CoO_{3-x}$ is much high than that of $Pr_{0.5}Ba_{0.5}CoO_{3-x}$. The phase diagram shows large differences in the two samples. It may come from the different radius of La and Pr or from the A-site disordered effect. I also found that the relative difference of volume between the LV and SV ($\Delta V_{LV\text{-}SV}/V$) in $La_{0.5}Ba_{0.5}CoO_{3-x}$ is much larger than that in $Pr_{0.5}Ba_{0.5}CoO_{3-x}$. From the phase diagram and the analysis of the volume in AFM and FM phase between these two samples, it is suggested that the much larger $\Delta V_{LV\text{-}SV}/V$ is related to the much stronger AFM in $La_{0.5}Ba_{0.5}CoO_{3-x}$.

In the last chapter, the summary and future work of the thesis are presented.

Contents

Abstract: I

Contents III

1 Introduction 1

1.1 Negative thermal expansion 1

1.2 Mechanism of NTE 2

1.3 Cobaltite perovskites 5

1.4 Research aim 8

2 Experiment 11

2.1 Sample synthesis methods 11

2.2 Iodometric titration method 12

2.3 X-ray diffraction measurement 12

2.4 Magnetization measurements 15

2.5 Neutron powder diffraction (NPD) 16

3 Magnetization and neutron powder diffraction results 23

3.1 Magnetization results 23

3.2 NPD patterns and crystal structure analysis 29

3.3 Magnetic structure analysis 40

3.4 NTE in $La_{0.5}Ba_{0.5}CoO_{3-x}$ 50

3.5 Phase diagram of $La_{0.5}Ba_{0.5}CoO_{3-x}$ 56

3.6 Relation of NTE and magnetic ordering 57

3.7 Effect of high magnetic field 60

4 Discussion 65

4.1 Phase diagram in $La_{0.5}Ba_{0.5}CoO_{3-x}$ and $Pr_{0.5}Ba_{0.5}CoO_{3-x}$ 65

4.2 $\Delta V_{LV\text{-}SV}/V$ in $La_{0.5}Ba_{0.5}CoO_{3-x}$ and $Pr_{0.5}Ba_{0.5}CoO_{3-x}$ 66

4.3 β in $La_{0.5}Ba_{0.5}CoO_{3-x}$ and $Pr_{0.5}Ba_{0.5}CoO_{3-x}$ 67

5 Summary and outlook 69

References 71

1 Introduction

1.1 Negative thermal expansion

Most of the materials expand upon heating originating from the anharmonic vibration of atoms [5]. However, some materials show contraction upon heating. Negative thermal expansion (NTE) is the phenomenon of lattice contraction as temperature increase. Thermal expansion, though small, is far from negligible, since thermal expansion may cause significant problems in engineering fields from structural components such as railroad tracks and bridges, to optical and electronic devices such as telescopes and sensors [1, 2]. Bridges and elevated highways, have to include expansion joints to avoid the roadway from bending when it expands in hot weather. In the microelectronic devices, the heat generated by the silicon chip will heat up surrounding components and lead to thermal cycling. The mismatched coefficient of thermal expansion in integrated circuits will cause cracking and deterioration of devices. In the high precision optical instrument, thermal expansion will change the thickness of the lens and consequently affect the focal length and optical property. Suppressing thermal expansion is important for device to improve the reliability, lifetime and performance. The discovery of NTE materials provide a good opportunity to control thermal expansion. The NTE materials are being widely used in manufacturing industry [6-8].

The coefficient of thermal expansion (CTE) can be expressed by the following equations [1, 2]:

$$\alpha = (\partial \ln l / \partial T)_P = (\partial l / \partial T)_P / l \,, \qquad (1)$$

$$\beta = (\partial \ln V / \partial T)_P = (\partial V / \partial T)_P / V \,, \qquad (2)$$

where α and β are linear and volumetric CTE, respectively. And l is the length, V is volume, T is Temperature and P is Pressure. In the case of a cubic material, there is a relation of $\alpha = 1/3 \cdot \beta$. However, for the material with an anisotropic nuclear crystal structure it shows different

thermal expansion along different axes. The thermal expansion of materials can be categorized into different groups according to the thermal expansion coefficient [9]. Thermal expansion coefficients of typical thermal expansion materials [10, 11] are presented in Table 1.1.1. In this work we focus on the Negative thermal expansion material.

Table 1.1.1. Thermal expansion coefficients of typical thermal expansion materials.

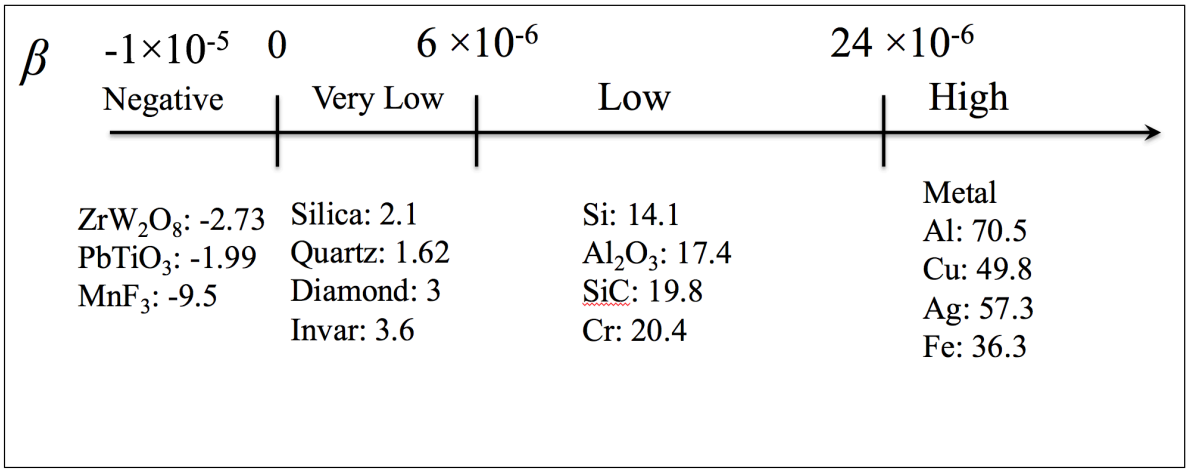

Negative thermal expansion has been investigated for decades, in a wide range of materials including metallic, inorganic and organic. Practical use has been made of the phenomenon in the development of low expansion materials, starting with the discovery of Invar in 1897 by Guillaume [12, 13]. The discovery of volume shrinkage in $LiAlSiO_4$ (β-eucryptite) [14, 15] in 1951 attracted much attention of research in the NTE material. But it was the strongly isotropic NTE in ZrW_2O_8 with $\beta = -2.73 \times 10^{-5}\ K^{-1}$over a wide temperature window from 0.3 to 1050 K [16-18] that attracted widespread attention and renewed considerable interest in NTE material during the last decade.

1.2 Mechanism of NTE

NTE is of fundamental interest since it may be caused by various mechanisms. NTE materials can arise from flexible framework structures with a common feature of M_1-O-M_2 linkages for polyhedra. Framework structures are crystal structures consisting of polyatomic units such as AO_4 tetrahedra and/or AO_6 octahedra, which are joined together by shared O

atoms at the corners. The transverse vibration about M_1-O-M_2 linkages is the key factor for the occurrence of NTE with a flexible framework structure, since the transverse vibrations need less energy than longitudinal ones. The NTE of ZrW_2O_8 is origin from the low energy transverse vibration of O atom in Zr-O-W linkage [16-20]. There are a number of classes of materials with a flexible framework structure, for example, ScF_3 [21-23], AM_2O_7(A = Ti, Zr, Hf, M = P, V) [15, 24] and Cd $(CN)_2$ [25]. NTE materials with a flexible framework structure is correlated with the low energy transverse vibrational modes.

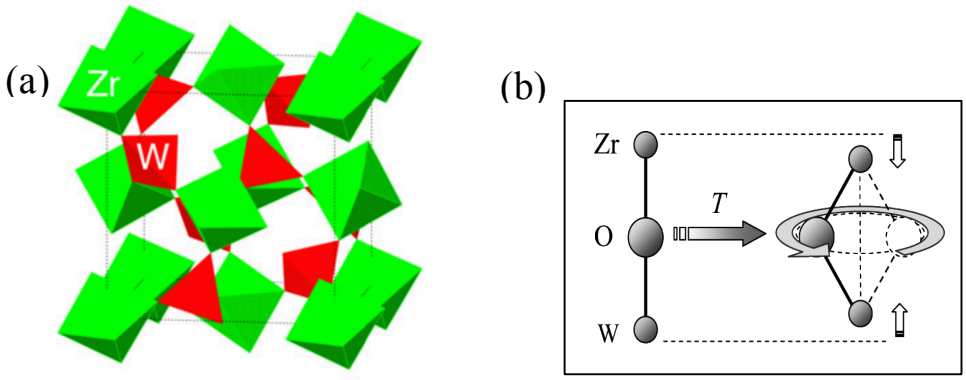

Fig. 1.2.1. (a) Schematic crystal structure of ZrW_2O_8 and (b) The transverse vibration of O in Zr-O-W [19].

NTE also can couple with the electronic properties. In NTE ferroelectrics, NTE originates from ferroelectric order which occurs due to the strong hybridization between cations and oxygen. For example, the negative thermal expansion in $PbTiO_3$ is related to the ferroelectric to paraelectric phase transition [26-31].

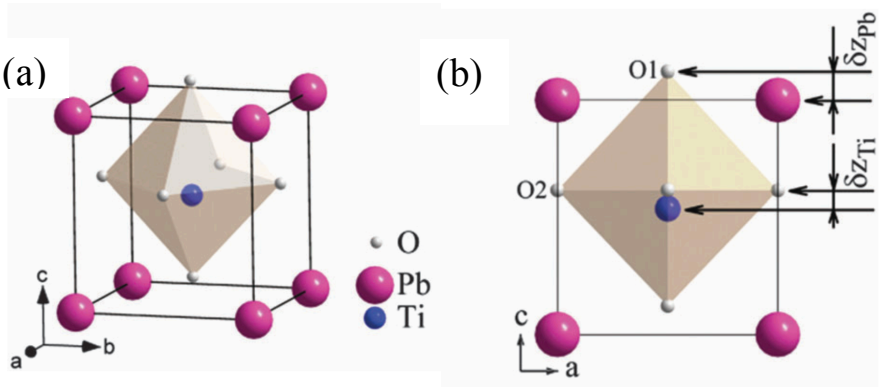

Fig. 1.2.2. Schematic crystal structure of PbTiO3 (a) and (b) spontaneous polarization displacements of δ_{Ti} in the TiO_6 octahedron and δ_{Pb} in the PbO_{12} polyhedron which are along the c axis [1].

The mechanism responsible for the nearly zero thermal expansion in $LaCu_3Fe_4O_{12}$ is an electronic transition between Cu and Fe ions [19, 32-34]. The valence state of these ions are Cu^{3+} and Fe^{3+} at room temperature. The charge transfers between Cu^{3+} and Fe^{3+} occurs on heating above 393 K resulting in Cu^{2+} and $Fe^{3.75+}$. Because of the constriction of Fe-O bonds, the unit cell volume shrinks by 1%. $SrCu_3Fe_4O_{12}$ shows similar behavior at about 200 K [35, 36]. The crystal structure of $LaCu_3Fe_4O_{12}$ and $SrCu_3Fe_4O_{12}$ is shown in Fig. 1.2.3.

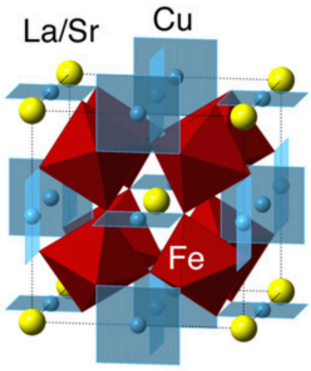

Fig. 1.2.3. Schematic crystal structure of $LaCu_3Fe_4O_{12}$ and $SrCu_3Fe_4O_{12}$ [19].

The anomalous thermal expansion resulting from magnetic ordering is called the magnetovolume effect (MVE) and was first found in the Invar alloy $Fe_{0.65}Ni_{0.35}$ [37-39]. Mn_3AN (A =Zn, Ga, etc.) [1, 40-43] are well known for their large MVE. The negative thermal expansion in Mn_3ZnN is related to the AFM to paramagnetic (PM) phase transition. At low temperature, it is in AFM state with large volume. And at high temperature, it is in PM state with small volume. The volume shrinks during the transition from PM to AFM upon cooling. The Γ^{5g} AF spin configuration and the cubic crystal structure are key factor for the pronounced magnetovolume effect in these manganese antiperovskites [44, 45]. The Mn_6X octahedron has three-dimensional geometrical frustration when the nearest-neighbor magnetic interaction J_1 is antiferromagnetic and the next-nearest-neighbor interaction J2 is ferromagnetic [46], as shown in Fig. 1.2.4. When the frustration prevents the system from gaining magnetic energy due to short-range ordering above T_N, the system may earn kinetic energy by shrinking its volume. This effect would enhance the MVE in this sample. Qu et. al [47] reported that by the first-principles calculation, the magnetic configuration Γ^{5g} has the largest lattice constant and lowest energy. When the magnetic transition from Γ^{5g} to the PM state occurs, large volume contraction would occur.

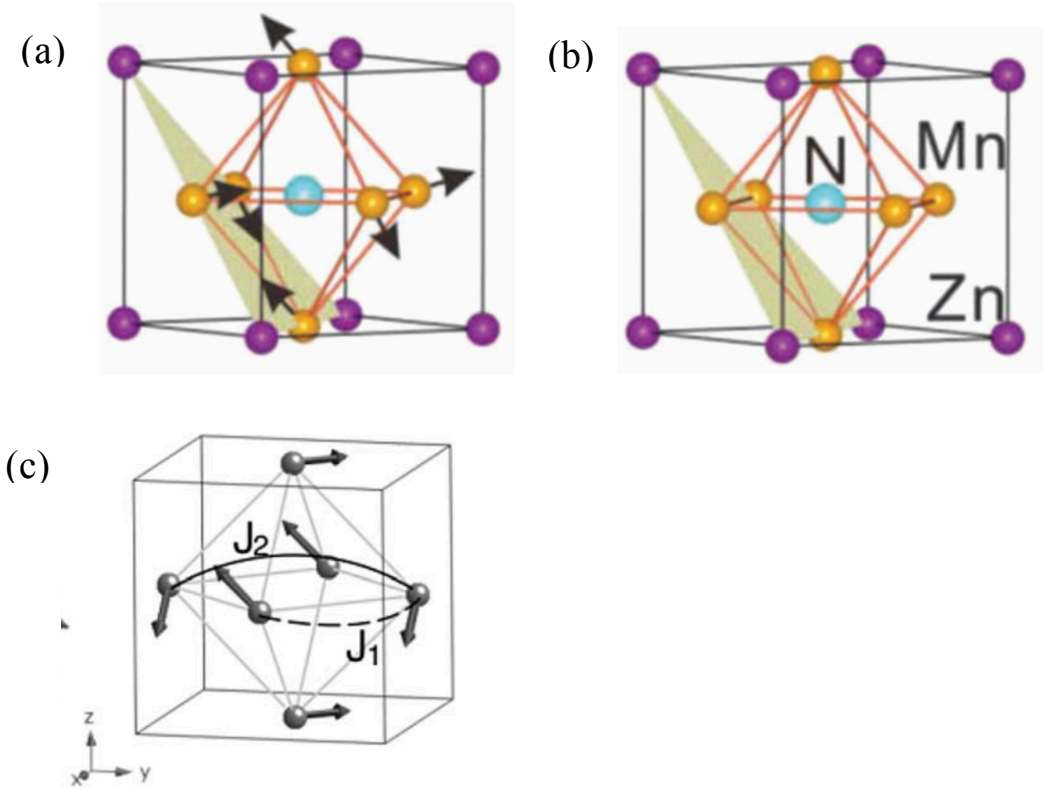

Fig. 1.2.4. Schematic crystal and magnetic structure of Mn_3ZnN (a)AFM state, (b) PM state [1] and (c) Γ^{5g} AF spin configuration.

1.3 Cobaltite perovskites

The cobaltite perovskites have attracted much attention due to their unusual properties such as metal–insulator transition, large magnetoresistance and spin-state transition, *etc*. The large magnetoresistance effect has been observed in $La_{1-x}A_xCoO_3$ (A = Ca, Sr, Ba) [48, 49]. The discovery of spin-state transition of Co^{3+} ion in $LaCoO_3$ has leaded to considerable interest in the cobaltite perovskites system, where the Co^{3+} ion is found to exhibit transition from low-spin state (LS, t_{2g}^6, $S = 0$) to the high-spin state (HS, $t_{2g}^4e_g^2$, $S = 2$) via the intermediate-spin state (IS, $t_{2g}^5e_g^1$, $S = 1$) as the temperature increases [50-52]. These properties originate from the interplay between the lattice, charge, spin and/or orbital degrees of freedom, so that the properties of cobaltite perovskites are very sensitive to chemical compositions (oxygen content, rare-earth element *etc.*) or external stimulus (temperature, pressure, magnetic field *etc.*).

The layered perovskites $RBaCo_2O_{5.5+x}$ (R: rare-earth elements with the valence 3+) are

also attractive because long-range spin-state ordering has been found to occur in conjunction with the metal–insulator transition induced by either temperature or hole doping (x) in RBaCo$_2$O$_{5.5+x}$ [53-58]. Moreover, recently our group observe strong negative thermal expansion (NTE) in PrBaCo$_2$O$_{5.5+x,}$ which is triggered by changing the hole doping level x [3]. Through the comprehensive study with NPD and Muon spin relaxation (μSR) *etc.*, we find this NTE is coupled with the spontaneous antiferromagnetic ordering, which is known as the MVE. And we consider this MVE is closely associated with the ferromagnetic (FM) and antiferromagnetic (AFM) competition.

There are two kind of cobaltite perovskite A-site ordered and A-site disordered. In the A-site order sample, the LaO and BaO layers alternate along the c axis. The schematic crystal structure of La$_{0.5}$Ba$_{0.5}$CoO$_{3-x}$ is illustrated in Fig. 1.3.1. The La/BaO and CoO layers alternate along the c axis. Co ions is in the center of octahedral. The La^{3+} and Ba^{2+} cations were distributed randomly in the same layer. The difference of size between La^{3+} and Ba^{2+} cations is very small, so that the disorder of these cations in the same layer is easy to achieve. The randomly distribution of oxygen vacancies in the La/BaO layer leads to the randomly distribution of corner- sharing CoO_5 pyramids (Pyr) and CoO_6 octahedra (Oct) along the b axis.

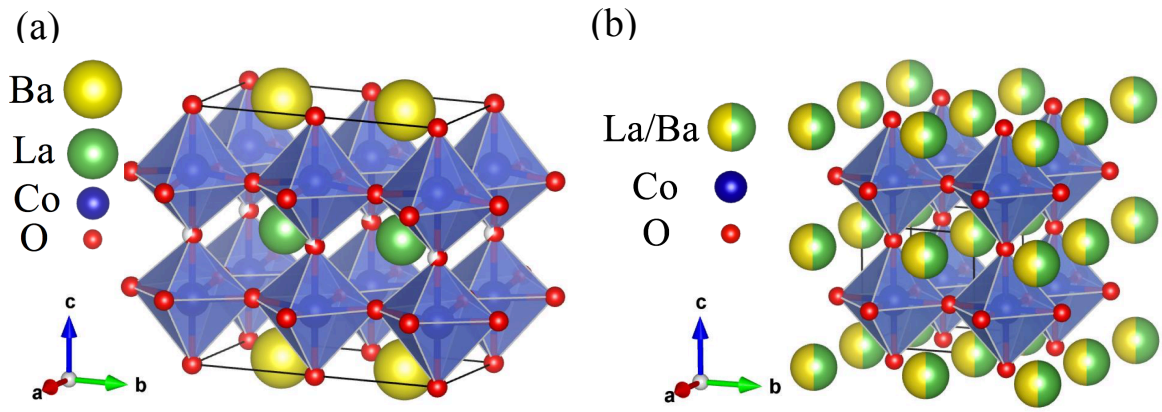

Fig. 1.3.1. Schematic crystal structure of (a) A-site ordered LaBaCoO$_{6-x}$ and (b) A-site disordered La$_{0.5}$Ba$_{0.5}$CoO$_{3-x}$.

In this research I am motivated to investigate NTE in the A-site disordered La$_{0.5}$Ba$_{0.5}$CoO$_{3-x}$ for the following reason. Firstly, the isotropic NTE is more important for industry application, since for the anisotropic NTE, microcracking may occur during repeated thermal cycling. In contrast to the anisotropic NTE in A-site ordered PrBaCo$_2$O$_{5.5+x}$, presented in Fig. 1.3.2, the NTE in A-site disorder La$_{0.5}$Ba$_{0.5}$CoO$_{3-x}$ is isotropic owing to the cubic crystal structure.

Furthermore, tremendous works on the manganites with colossal magnetoresistance, which originates from the competition between AFM-insulating phase and FM-metallic phase, have shown that A-site ordering imposes significant effect on the competition strength [4, 59]. From Tokura's report [4] A-site disordered can enhance phase fluctuation, even lead to phase separation, shown in Fig1.3.3, which reveals the strong phase competition. Since the NTE in cobaltite perovskite is related to the competition of AFM and FM, the A-site disordered may affect the NTE. Therefore, in this research I study the A-site disordered $La_{0.5}Ba_{0.5}CoO_{3-x}$ and compare with the A-site ordered counterpart. By investigating the A-site disordered effect on the NTE in the cobaltite perovskite, I expect to obtain deeper understanding of the microscopic origin of NTE in this cobaltite.

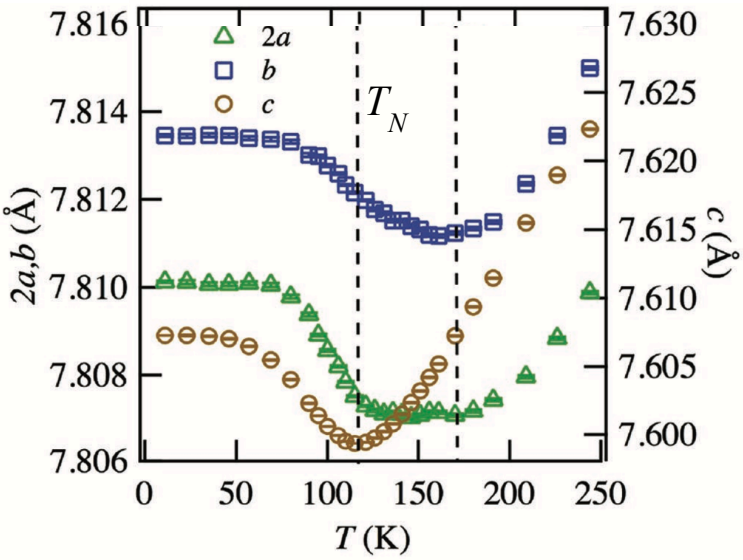

Fig. 1.3.2. Anisotropic NTE in A-site ordered $PrBaCo_2O_{5.5+x}$ [3].

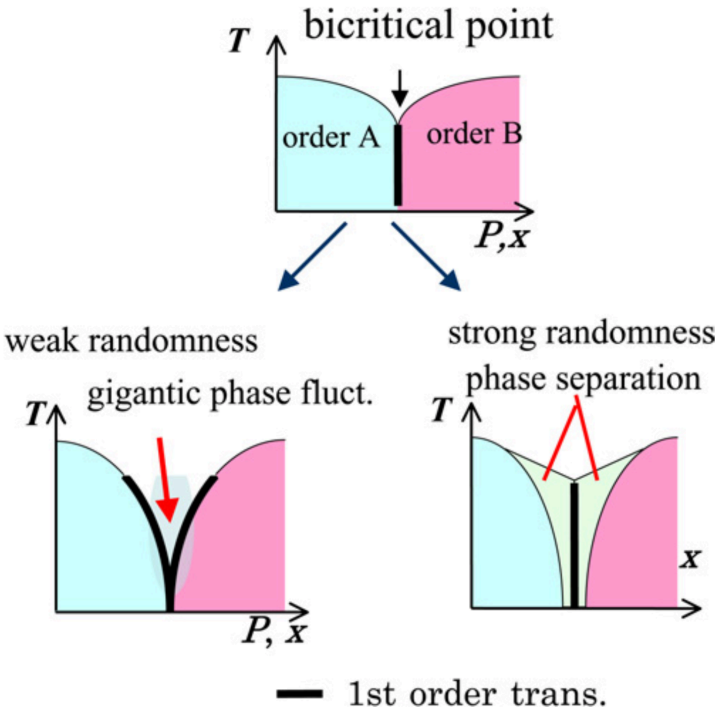

Fig. 1.3.3. The A-site disordered enhances the phase fluctuation [4].

There are extensive investigations on the hole-doping effect to $LaCoO_3$ through substitution of divalent ion *A* (*A* = Ca, Sr, Ba) for La [60, 61]. However, the hole doping to Co^{3+} ion can also be introduced by varying the oxygen content, which has not been widely exploited. For example, the nominal valence of Co ion in $La_{0.5}A_{0.5}CoO_{2.75}$ is 3+, and holes can be filled to the band by increasing the oxygen content. In previous report [62-67], the A-site disordered $La_{0.5}Ba_{0.5}CoO_{3-x}$ (x = 0), shows FM transition at Curie temperature (T_C) 180 K. As the oxygen decreases to x = 0.13, the antiferromagnetic (AFM) correlation develops coexists with the FM state at low temperature. When the oxygen content is further lowered to an electron doping side (x = 0.4), it shows pure AFM state with the Neel temperature (T_N) above room temperature. The properties of cobaltite perovskites $La_{0.5}Ba_{0.5}CoO_{3-x}$ are very sensitive to chemical compositions (rare-earth element, oxygen content *etc.*) or external stimulus (temperature and pressure etc.).

1.4 Research aim

In this work, I expect to search possible NTE in A-site disordered $La_{0.5}Ba_{0.5}CoO_{3-x}$ and investigate the A-site disordered effect on the NTE in the cobaltite perovskite. The A-site

disordered perovskite cobaltite $La_{0.5}Ba_{0.5}CoO_{3-x}$ was synthesized by solid state reaction and the oxygen content was control by annealing the sample under Ar gas at different temperature. In order to find NTE and study the underlying mechanism of the NTE in these samples, a combination of X-ray powder diffraction (XRD), neutron powder diffraction (NPD) and the superconducting quantum interference device (SQUID) magnetometer (MPMS) was used to investigate the crystal structure and magnetic structure. The NTE is related to the competition between AFM phase and FM phase. It is important to further study the mechanism of NTE in $La_{0.5}Ba_{0.5}CoO_{3-x}$ by changing the competition of FM and AFM by magnetic field. Therefore, we performed the NPD under magnetic field and investigate the relation of NTE and magnetism.

2 Experiment

2.1 Sample synthesis methods

The samples of $La_{0.5}Ba_{0.5}CoO_{3-x}$ were prepared by standard solid-state reaction. The process is similar as the methods described in references [63, 68]. The raw material La_2O_3 was pre-annealed at 900 °C in order to eliminate possible traces of carbon dioxide and water. The raw materials La_2O_3, $BaCO_3$ and CoO were mixed with the stoichiometric ratio. The mixed powder was ground adequately and pressed into pellet, followed by heating at 1200 °C in air for 12 h using the furnace of MSFT-1530 of Yamada Denki, showed in Fig.2.1.1(a). Temperature increasing and decreasing rate were 2 °C/min. Grinding and heating were repeated for 3 times. We could obtain the single-phase A-site disordered sample $La_{0.5}Ba_{0.5}CoO_{3-x}$ (x = 0.09). The oxygen contents were controlled by annealing the as-synthesized compound under a flow of pure Ar gas at different temperature using the tube furnace of Koyo at the Comprehensive Research Organization for Science and Society (CROSS) user laboratories in Tokai, Japan, shown in Fig. 2.1.1(b). The samples of x = 0.11, 0.13, 0.14, 0.18 and 0.34 were obtained by annealing the attained samples x = 0.09 under Ar gas flowing for 12 hours at 200°C, 250 °C, 270°C, 350°C and 800°C, respectively. The oxygen content was determined by analysis of neutron powder diffraction pattern and iodometric titration method.

(a) (b)

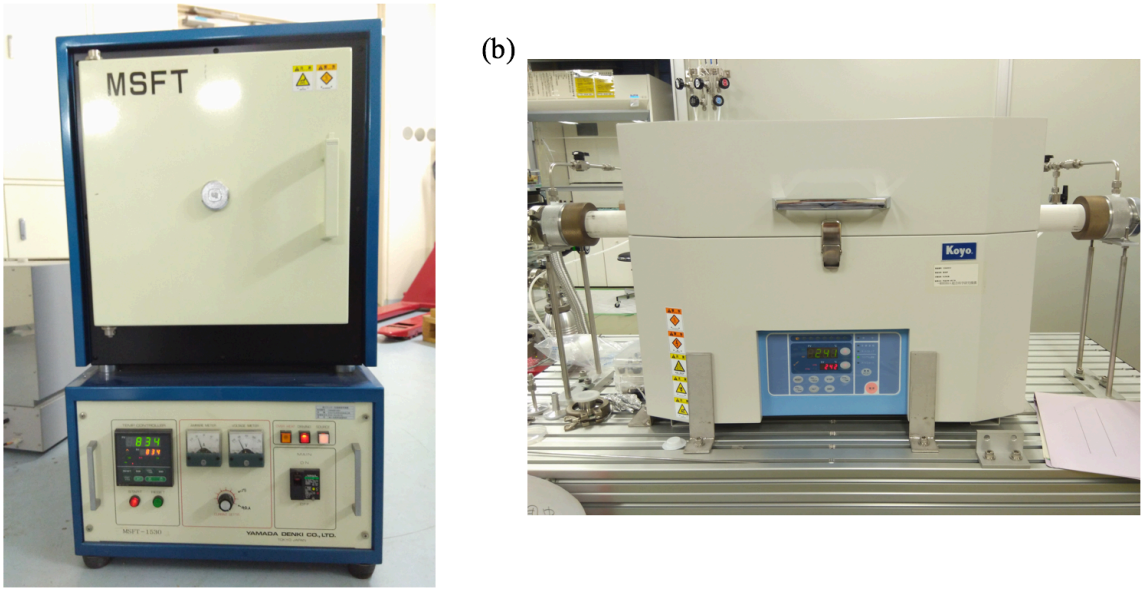

Fig. 2.1.1. Pictures of furnace of MSFT-1530 and tube furnace of Koyo.

2.2 Iodometric titration method

Since it is crucial to know the exact value *x* of oxygen deficit in the samples, we determined the x by iodometric titration method. Iodometric titration method is an analytical technique in which the $La_{0.5}Ba_{0.5}CoO_{3-x}$ samples are dissolved in diluted hydrochloric acid in the presence of potassium iodide. As a result, the reduction reaction of Co^{3+} or Co^{4+} to Co^{2+} ions take place while the I^- ions are oxidized to iodide. The amount of the iodide is determined by titration with sodium thiosulfate, $Na_2S_2O_3$. The starch which produces a blue color in a contact with iodine molecules, is used as an indicator for detecting the end of titration. From the amount of the iodine we can calculate the average oxidation state of cobalt cations and consequently the oxygen index.

2.3 X-ray diffraction measurement

The phase purity of the samples was checked by X-ray diffraction (XRD) measurements. The XRD measurements were performed by a Rigaku SmartLab diffractometer with secondary monochromator using Cu $K_{\alpha 1}$ X-radiation with λ = 1.540560Å, shown in Fig. 2.3.1(a). All the patterns were collected in a continuous scanning mode. The sample is prepared on a glass

holder and fixed on the sample platform, shown in Fig. 2.3.1(b) and (c). Only a small amount of powder about 1g is necessary. The X-ray generator, detector and the sample holder are in the same vertical plane. The X-ray generator and detector enable to revolves round the sample within the same vertical plane.

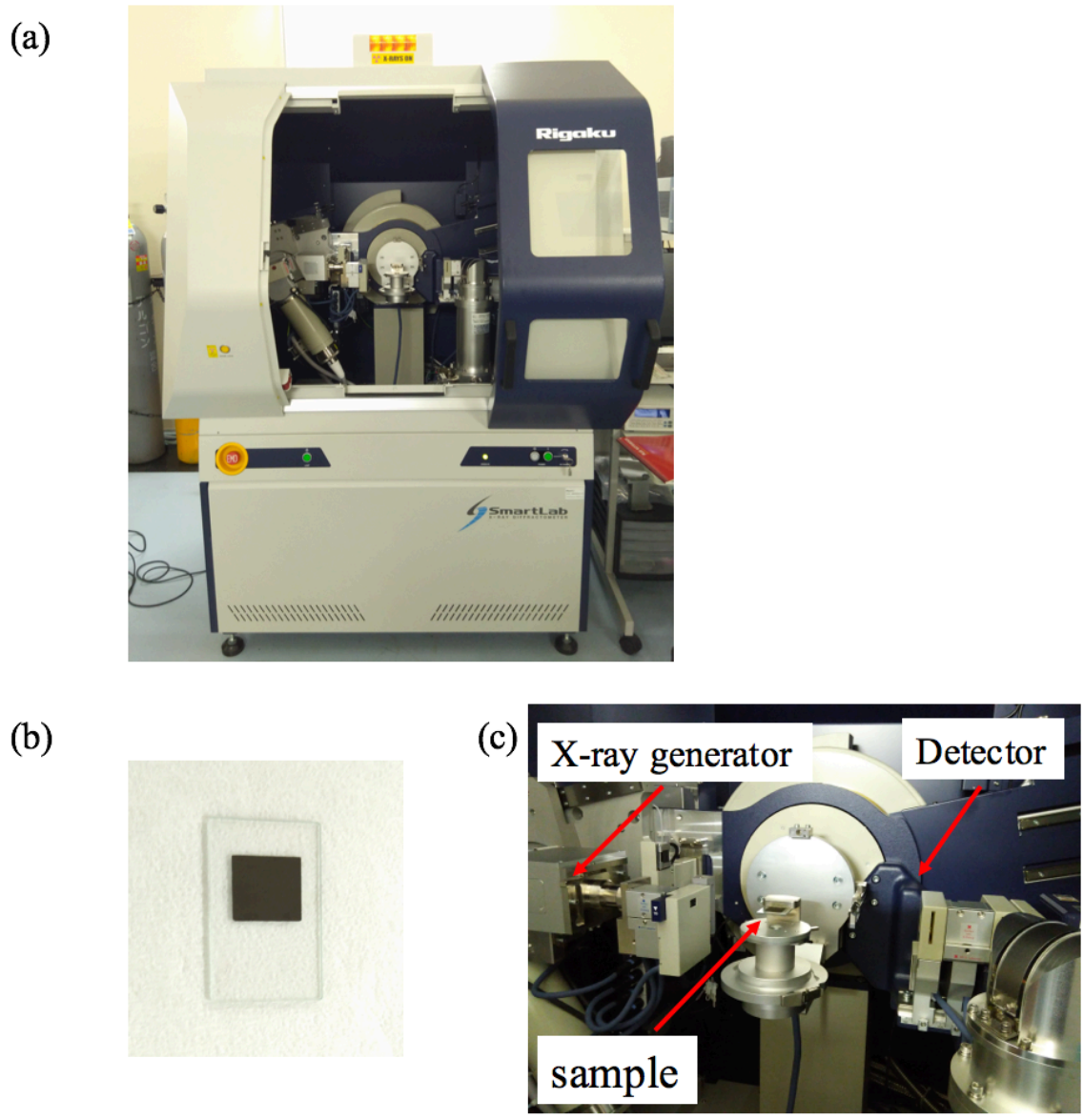

Fig. 2.3.1. Pictures of (a) Rigaku SmartLab diffractometer, (b) sample preparation and (c) sample installation.

All the XRD patterns of the samples were collected at room temperature. The patterns annealing at different temperature are exhibited in Fig. 2.1.3. As the annealing temperature increase, the patterns shift to the low 2θ, which indicates the lattice constant increases. Fig.

2.3.3 shows the Rietveld refinement of the pattern for the sample without annealing (x = 0.09). The pattern can be refined well by the cubic space group $Pm\bar{3}m$ with χ^2 = 1.41. All the Bragg peak of the pattern can be indexed and not any spurious Bragg peak is observed, revealing the good crystallization of the sample.

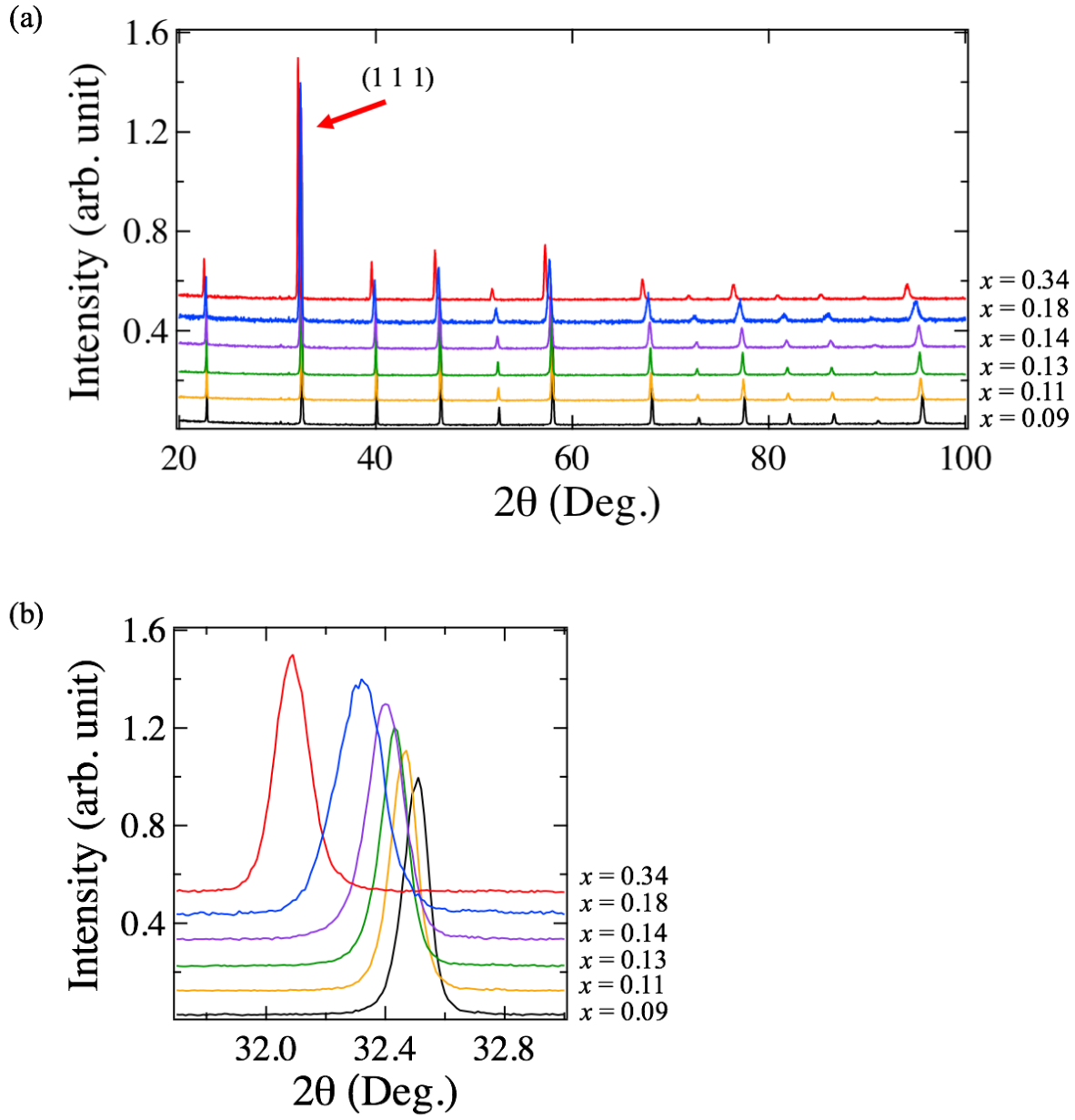

Fig. 2.3.2. (a) XRD patterns of the samples annealing at different temperature, (b) 111 reflection of the patterns.

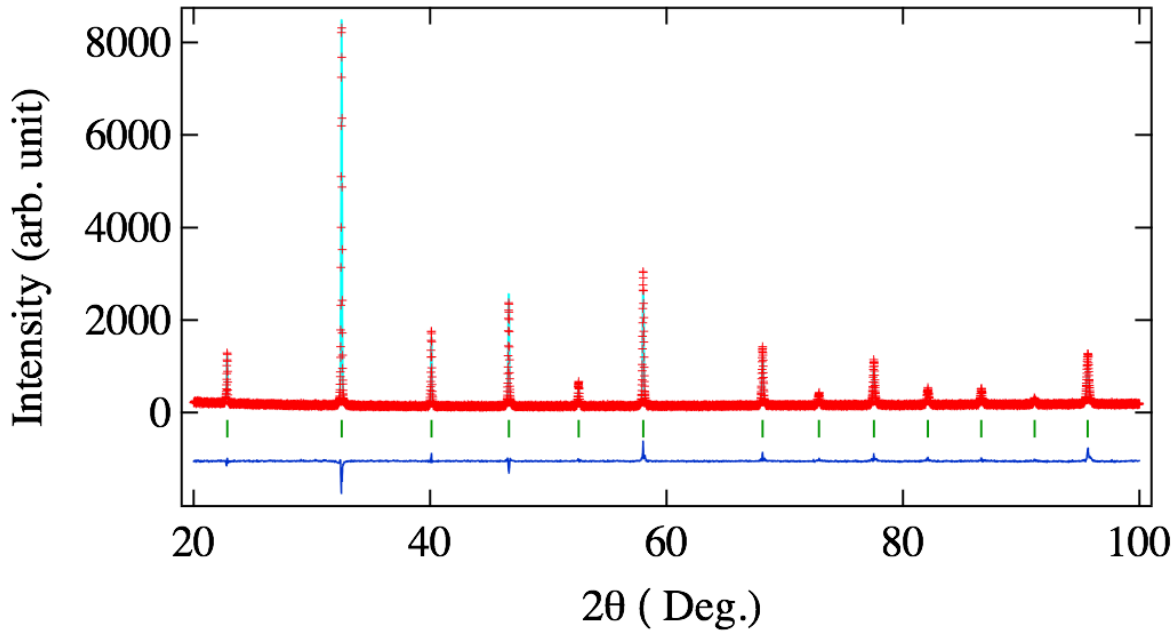

Fig. 2.3.3. The observed and calculated patterns of the sample without annealing (x = 0.09) are shown at the top with the cross markers and the solid blue line, respectively. The vertical green marks in the middle show positions calculated of Bragg reflections for nuclear. The bottom blue line represents the difference between observed and calculated intensities.

2.4 Magnetization measurements

The temperature and field dependence of magnetization measurements presented in this work were conducted by using a dc superconducting quantum interference device (SQUID) magnetometer (MPMS) at CROSS-Tokai user laboratories, shown in Fig. 2.4.1(b). This system enables to measure the direct magnetization (DC) of a sample in the temperature range of 2K to 400K under an external magnetic field which can change from 0 to 1 Tesla. The sample with 100 - 200 mg is filled in a diamagnetic capsule and fixed at the end of a long rod which can move longitudinally along the direction of the magnetic field, shown in Fig. 2.4.1(a). The temperature dependences of magnetization measurements were performed under field cooled (FC) and zero-field cooled (ZFC) mode.

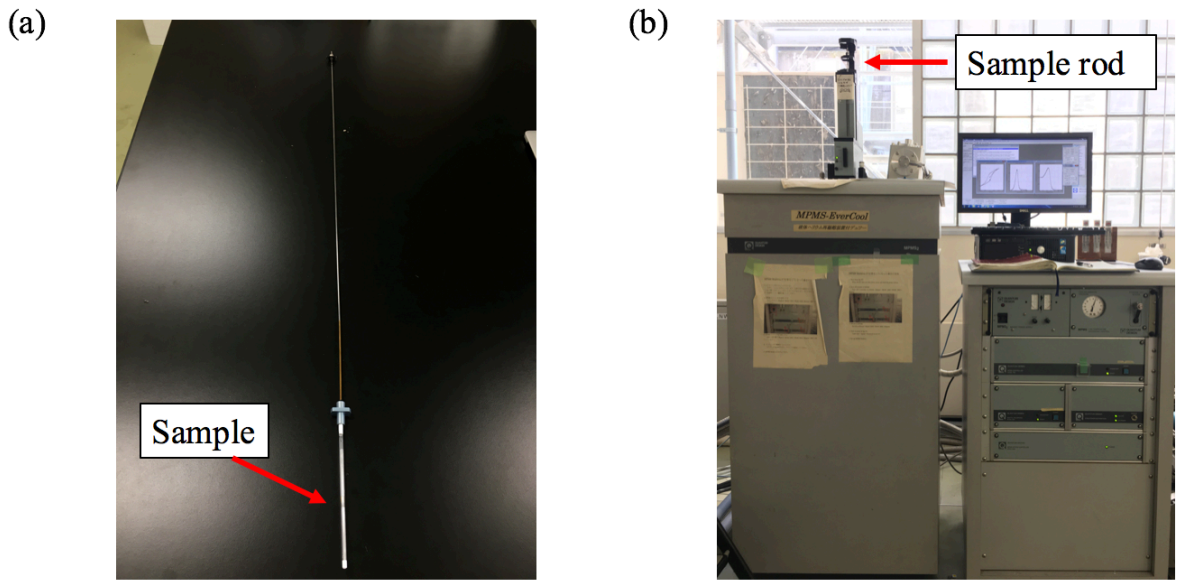

Fig. 2.4.1. Pictures of (a) sample and sample rod, (b) dc superconducting quantum interference device (SQUID) magnetometer (MPMS).

2.5 Neutron powder diffraction (NPD)

The neutrons are particles with mass of 1.675 x 10^{-27} kg and have a spin S =1/2. The neutron has no electric charge but a magnetic moment of about -1.9130 μ_N with μ_N = 3.152 x 10^{-14} MeV/T. Neutrons possess magnetic moments giving rise to magnetic contribution to the scattering. A weak interaction between neutron (which is a charge free) and nuclei allow studies of bulk materials. There are two contributions observed in the diffraction pattern [69, 70]:

(1) Nuclear scattering given by the interaction between neutron and nucleus.

(2) Magnetic neutron scattering given by the neutron interaction with the magnetic moment of an atom.

There are some advantages for neutron [69-72], compared to the X-ray:

(1) With the spin S =1/2, the neutron can interact with the spin of any unpaired electrons of an atom, which results in so-called magnetic scattering. So it can reveal the magnetic property of the material, such as magnetic structure and magnetic excitation.

(2) Unlike X-ray, neutron scattering length are independent of the atomic number. X-rays interact with the electron cloud surrounding each atom while neutrons interact directly with the nucleus of the atom. Some light (low Z) atoms contribute strongly to the diffracted intensity. So Neutron scattering plays an irreplaceable role in the field of biological and energy materials, which contain the light elements, such as hydrogen, lithium and oxygen. And also neutron scattering and absorption cross sections vary from each isotope. It can be used to investigate the isotope, for example hydrogen and deuterium.

The neutron powder diffraction (NPD) has been used in order to study nuclear and magnetic structure in cobaltite perovskites $La_{0.5}Ba_{0.5}CoO_{3-x}$. The neutron diffraction pattern can provide detail information of the structure of the materials, such as crystal and magnetic structure, atomic displacement and occupancy. The diffraction pattern can be observed only when the magnitude of radiation wavelength is in the same order as the atomic sizes. For the time-of-flight technique (TOF), from the de Broglie relation($\lambda = \frac{h}{mv}$, where h is the Planck constant, m is the neutron mass and v is the neutron velocity), we can obtain the neutron wavelength λ:

$$\lambda = \frac{ht}{mL}, \tag{2.1}$$

where L is the flight path and t is the time of flight. The measurement principle of neutron diffraction is based on the Bragg Equation [73]:

$$2d_{hkl}sin\theta = n\lambda, \tag{2.2}$$

where d_{hkl} is the inter-plane distance, *h, l and k* are the Miller indices denoting the lattice planes, θ is the scatting angle and n is an integer indicating the order of the diffraction peak.

The von Laue condition equivalently describes the diffraction process. In the case of diffraction (elastic neutron scattering), without energy transfer, incoming and outcoming beam are of the same absolute value and $k_i = k_f$. The scattering vector **Q** is defined by $\mathbf{k}_i + \mathbf{Q} = \mathbf{k}_f$. The scattered intensity I is proportional to the square of the scattering amplitude A,

$$I(\mathbf{Q}) \propto |A(\mathbf{Q})|^2 = \left| \sum_{\mathbf{G}} n_{\mathbf{G}} \int e^{i(\mathbf{G}-\mathbf{Q})\cdot\mathbf{r}} dV \right|^2, \tag{2.3}$$

where G is the reciprocal lattice vector and n_G are the Fourier components of the scattering density $n(r)$. The scattering condition $Q = G$ is analog to Bragg's law. For the sample with a certain volume V_Z and N unit cells we can get

$$I(\mathbf{Q}) \propto |A(\mathbf{Q})|^2 = \left| N \int_{V_Z} n(\mathbf{r}) e^{i\mathbf{Q}\cdot\mathbf{r}} dV \right|^2 = |NF(\mathbf{G})|^2, \tag{2.4}$$

For neutron scattering the atom form factor is $F(\mathbf{G}) = \sum_j b_j e^{i\mathbf{Q}\cdot\mathbf{r}}$, where b_j is the scattering length. The intensity $I(\mathbf{Q})$ is the function of atomic position. So we can obtain the structure information by analyzing the position and intensity of the Bragg peak. More detail descriptions of neutron scattering can be found in references [74, 75].

The high-resolution neutron powder diffraction (NPD) measurement was carried out by Super High Resolution Powder Diffractometer (SuperHRPD) at Materials and Life Science Experimental Facility (MLF), Japan Proton Accelerator Research Complex (J-PARC) [76]. As shown in Fig. 2.5.1., this neutron powder diffractometer has three groups of detectors, called high-angle bank, 90 degree bank and low-angle bank. These three banks enable to collect pattern at 150° - 175° with d range of 0.3 - 4.0 Å, at 60° - 120° with d range of 0.3 - 4.0 Å and at 10° - 40° with d range of 0.3 - 4.0 Å, respectively. The Optimal resolution of SuperHRPD is $\Delta d / d = 0.0353 \pm 0.0003\%$ at $2\theta = 172^\circ$ [77]. As exhibited in Fig. 2.5.2, compared the Bragg peaks of Si measured by Sirius diffractometer and SuperHRPD, SuperHRPD has much higher resolution, which enable us to investigate more complex structures and detect slight structural changes. The neutron diffraction patterns were analyzed by the Rietveld refinement method using both Z-Rietveld [78, 79] and FULLPROF [80].

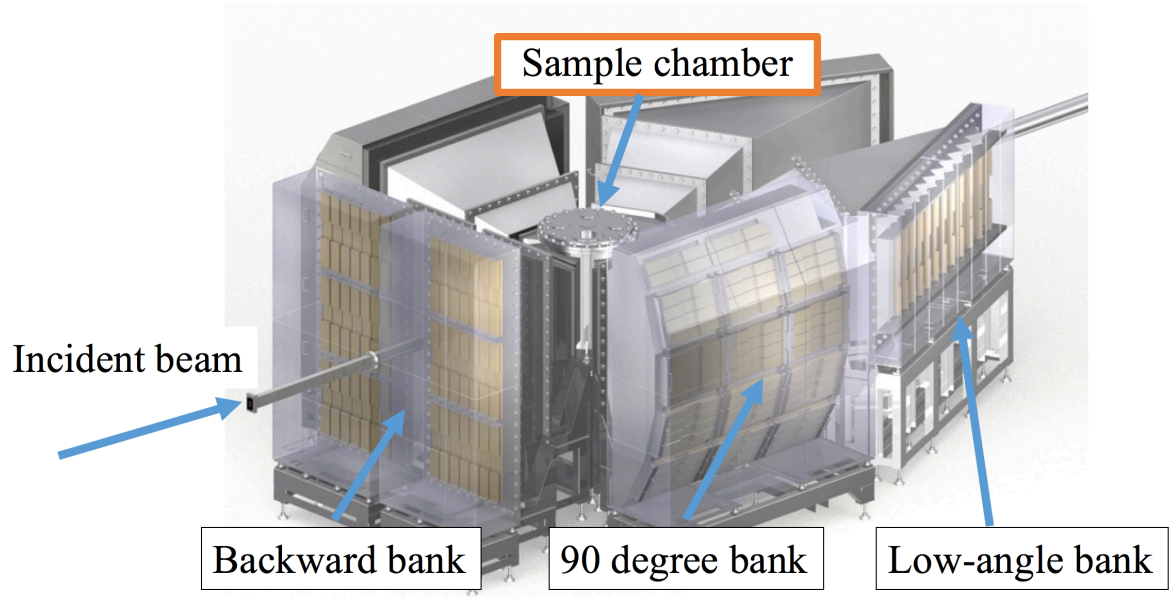

Fig. 2.5.1. Schematic picture of SuperHRPD

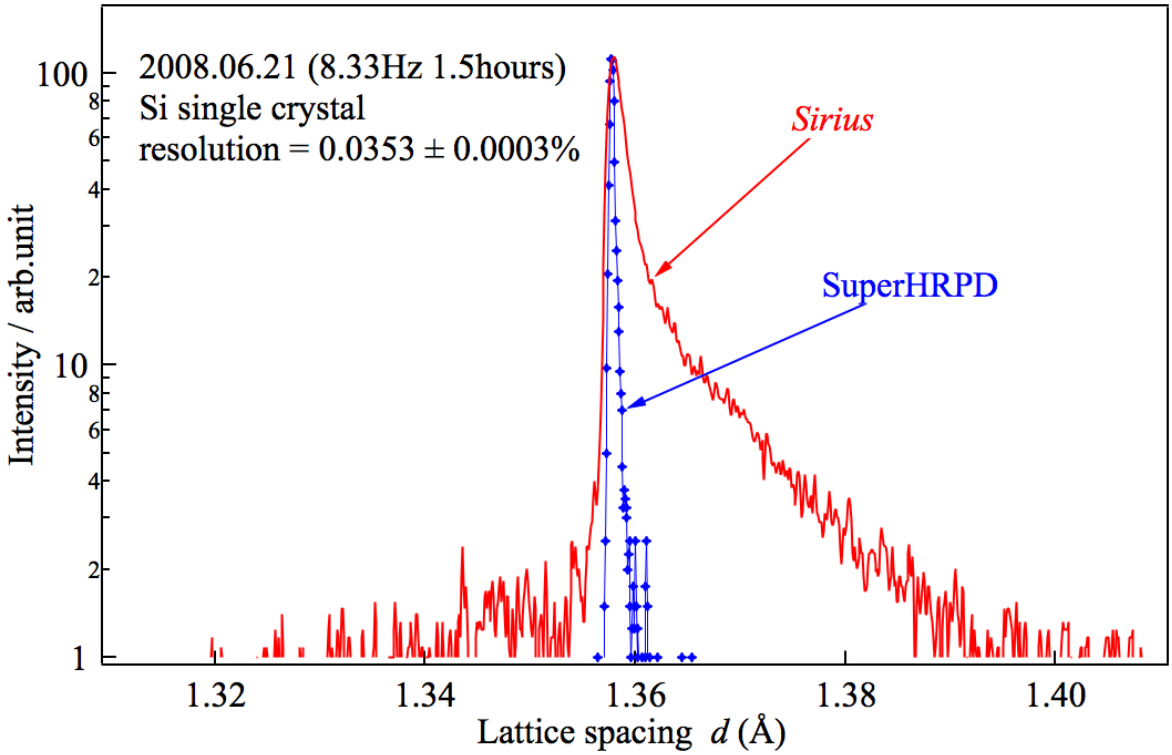

Fig. 2.5.2. Si (400) reflection measured by Sirius and Super-HRPD [69].

There are 5 options of sample environment for measuring under different condition, including auto sample changer (room temperature), 4K-type closed cycle refrigerator (4 - 300 K), Top-loading refrigerator (10 - 300K), high temperature furnace (~950°C) and refrigerator

of magnet option (0 - 14 Tesla). All the options use the same Vanadium sample can. In this work the temperature dependence of NPD measurements without magnetic field were performed by using Top-loading refrigerator, shown in Fig. 2.54. The sample can be inserted from the top along the vertical direction whilst neutron beam access is in the horizontal plane. The diameter of Vanadium sample can is 6mm. The sample, usually of the height above 4cm, is set in the Vanadium sample holder. The sample holder was enclosed after filled with He gas for thermal conduction at low temperature. Then the Vanadium sample holder was fixed at the end of a long sample rod, as shown in Fig. 2.5.4.

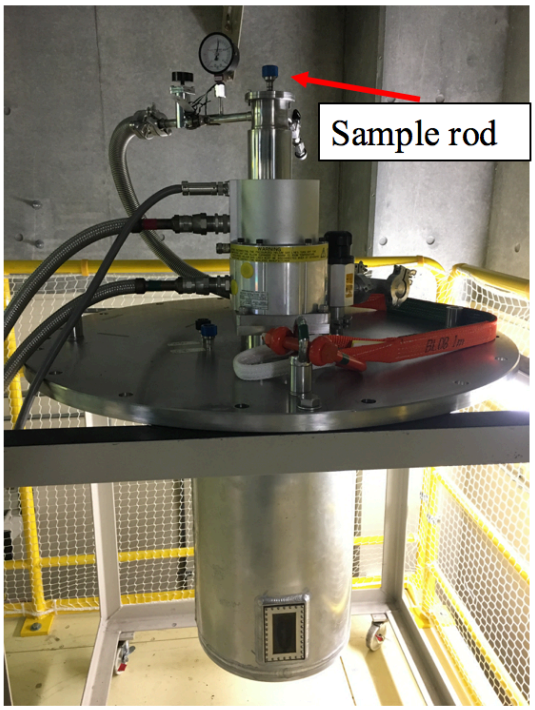

Fig. 2.5.3. Pictures of Top-loading refrigerator.

(a)

(b)

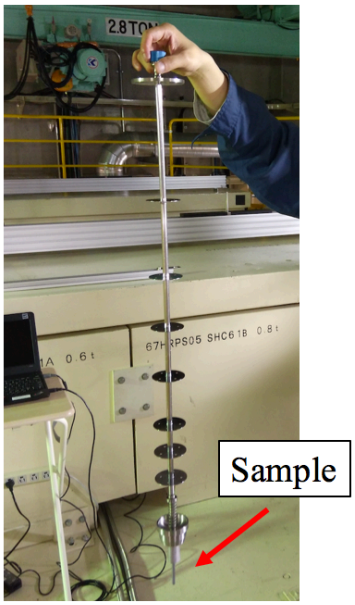

Fig. 2.5.4. Pictures of (a) Vanadium sample holder and (b) sample rod for Top-loading refrigerator.

The high-resolution neutron powder diffraction measurements under magnetic field were performed by SuperHRPD with a newly installed refrigerator of magnet option. A liquid Helium cryostat with the superconducting magnet of Oxford Instruments was recently installed on SuperHRPD, shown in Fig. 2.5.5. Neutron beam access is in the horizontal plane of the cryostat. The superconducting magnet is in the form of split pairs with magnetic field vector in the vertical plane of the cryostat. Sample environment access is along the vertical magnetic field direction. The measuring temperature range is from 1.5 K to room temperature with magnetic field up to 14 Tesla throughout the temperature range. The data was collected from the middle part of the high-angle bank, offering profile collection of -7.5º to +7.5º in the vertical direction and 150º to 175º in the horizontal direction. By virtue of high resolution (Δd / d = 0.0353 ± 0.0003% at 2θ = 172º) of SuperHRPD, we attained high quality neutron powder diffraction profiles under magnetic-field environment.

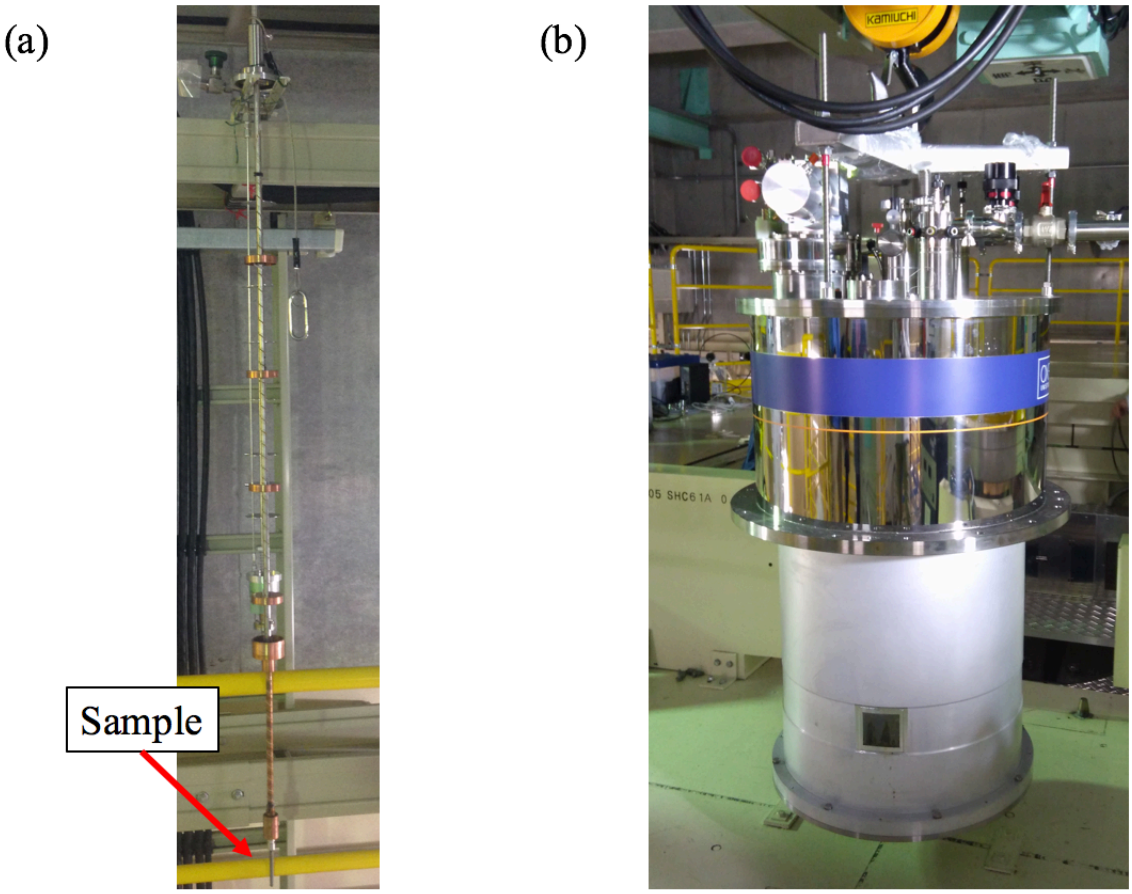

Fig. 2.5.5. Pictures of (a) sample rod and (b) refrigerator of magnet option.

3 Magnetization and neutron powder diffraction results

3.1 Magnetization results

The magnetization as a function of temperature (M / T curve) measured under 100 Oe magnetic field under both zero-field cooling (ZFC) and field cooling (FC) processes for $La_{0.5}Ba_{0.5}CoO_{3-x}$ (x = 0.09) are presented in Fig. 3.1.1(a). The large difference between the magnetization of ZFC and FC process in Fig. 3.1.1(a) and the hysteresis loop in the magnetization as a function of magnetic field (M / H curve) at 10 K in Fig. 3.1.1(b) indicate that FM component exists at base temperature. The FC magnetization of x = 0.09 exhibits a ferromagnetic transition at about 170 K. This Curie temperature is slightly lower than that in stoichiometric $La_{0.5}Ba_{0.5}CoO_3$ in which the ferromagnetic transition occurs near 180 K [63,81]. The M / H curve for $La_{0.5}Ba_{0.5}CoO_{3-x}$ (x = 0.09) (see in Fig. 3.1.1(b)) shows that the magnetization under 1 T achieves 1.80 μ_B/Co at 10K.

Fig. 3.1.2(a) show the temperature dependence of magnetization under 100 Oe for x = 0.11. Compared to the M/T curve of x = 0.09, below 130 K the decrease of magnetization under FC process with decreasing temperature suggests the AFM component occurs at base temperature. However, the difference between the magnetization of ZFC and FC process suggests that FM component exists at base temperature. And the hysteresis loop of the M/H curve (see in Fig. 3.1.2(b)) at 10 K also indicates that FM component exists at base temperature. So the AFM and FM component coexist in the sample x = 0.11. The FC magnetization of x = 0.11 exhibits a ferromagnetic transition at about 160 K. The M/H curve for $La_{0.5}Ba_{0.5}CoO_{3-x}$ (x = 0.11) (see in Fig. 3.1.2(b)) shows that the magnetization under 1 T achieves 0.34 μ_B/Co at 10K.

Similarly, the temperature dependence and field dependence of magnetization under 100 Oe for x = 0.13, 0.14 and 0.18 (see in Fig. 3.1.3, Fig. 3.1.4 and Fig. 3.1.5, respectively) indicate the AFM and FM component coexist at base temperature. The cusp in the FC curve indicates the AFM component exists at base temperature. However, the difference between the magnetization of ZFC and FC process and the hysteresis loop of the M/H curve at 10 K suggest

that FM component also exists at base temperature. The M/H curves show that the magnetization under 1 T is about 0.05, 0.04 and 0.02 μ_B/Co at 10K for x = 0.13, 0.14 and 0.18, respectively.

The temperature dependence and field dependence of magnetization for x = 0.34 under 100 Oe is shown in Fig. 3.1.6. The hysteresis loop was not observed in the M/H curves. This suggests the ground state is in the AFM state.

The magnetization at 1T decrease from 1.80 μ_B/Co at x = 0.09 to 0.005 μ_B/Co at x = 0.34. All these results indicate that the ground state of sample with high oxygen content is FM and the decrease of the oxygen content introduces AFM interaction.

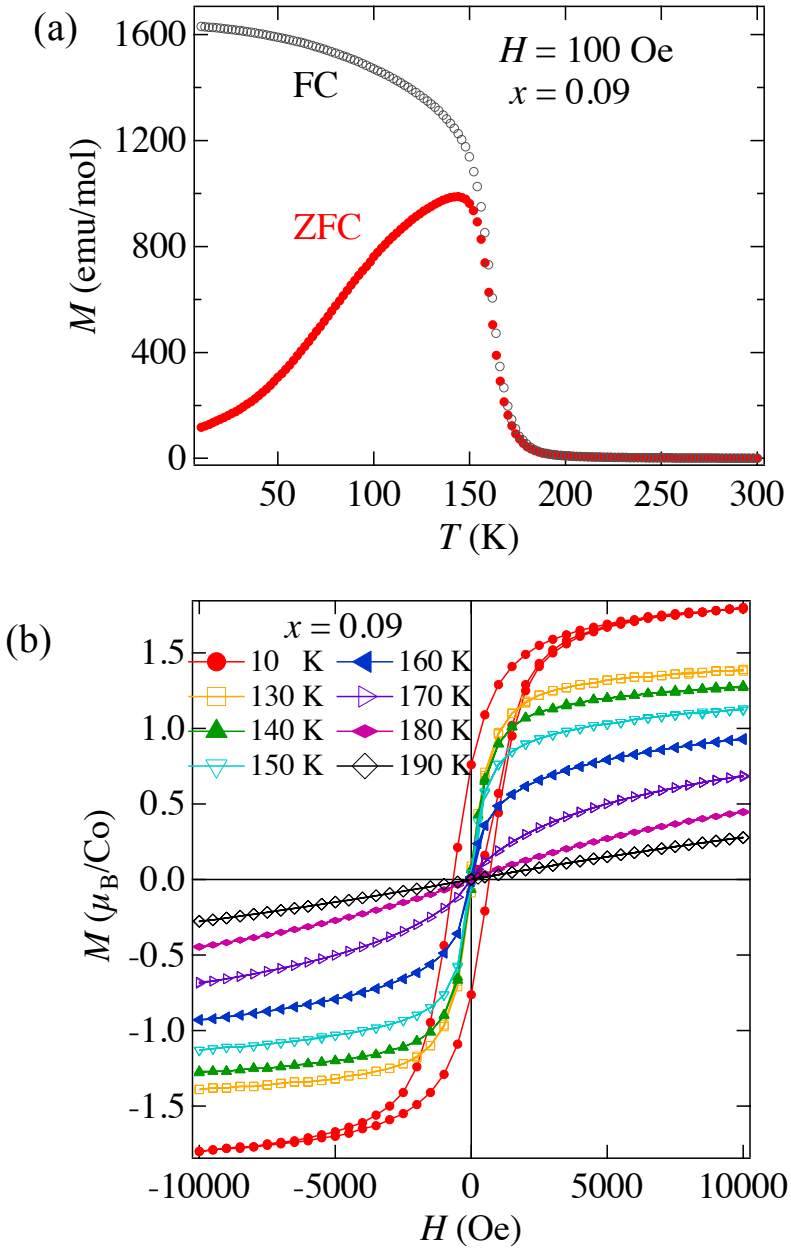

Fig. 3.1.1. (a) Temperature dependence of magnetization for $La_{0.5}Ba_{0.5}CoO_{3-x}$ (x = 0.09) under 100 Oe in the ZFC and FC processes respectively. (b) M / H curve at different temperature.

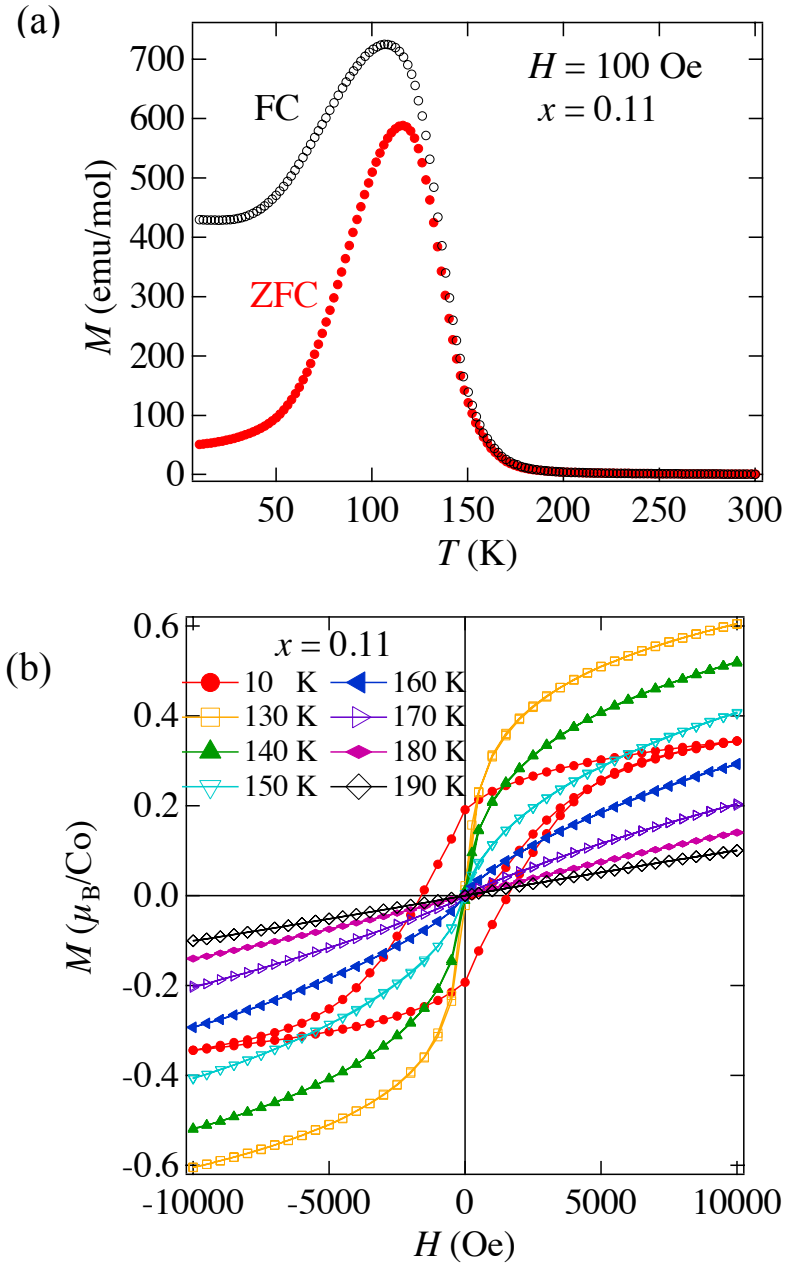

Fig. 3.1.2. (a) Temperature dependence of magnetization for $La_{0.5}Ba_{0.5}CoO_{3-x}$ (x = 0.11) under 100 Oe in the ZFC and FC processes respectively. (b) M/H curve at different temperature.

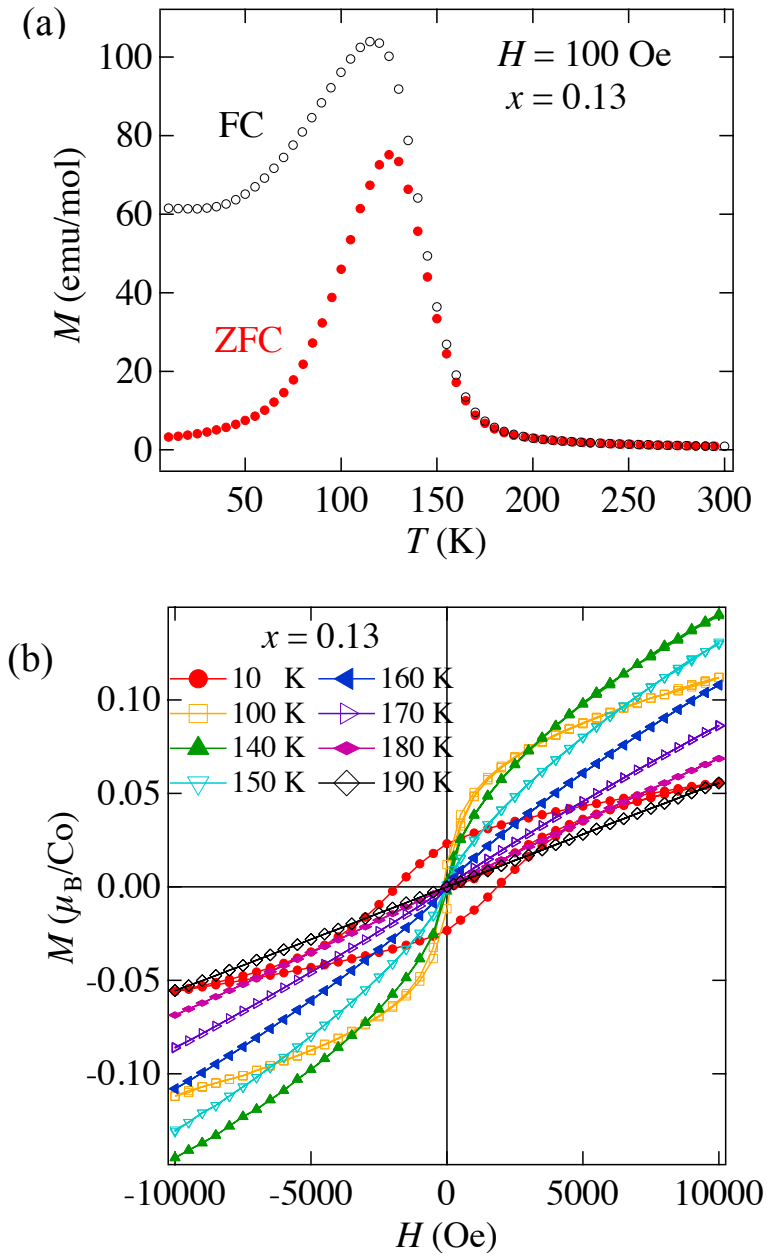

Fig. 3.1.3. (a) Temperature dependence of magnetization for $La_{0.5}Ba_{0.5}CoO_{3-x}$ ($x = 0.13$) under 100 Oe in the ZFC and FC processes respectively. (b) M/H curve at different temperature.

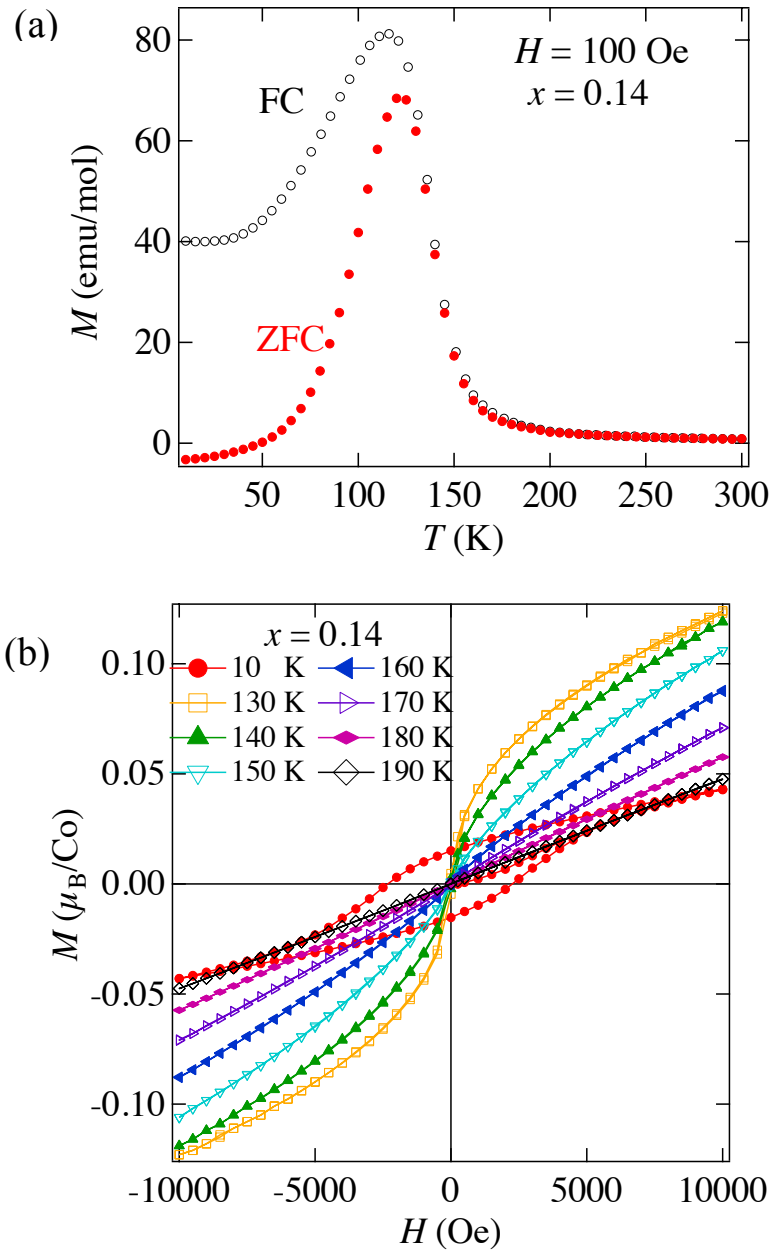

Fig. 3.1.4. (a) Temperature dependence of magnetization for $La_{0.5}Ba_{0.5}CoO_{3-x}$ (x = 0.14) under 100 Oe in the ZFC and FC processes respectively. (b) M/H curve at different temperature.

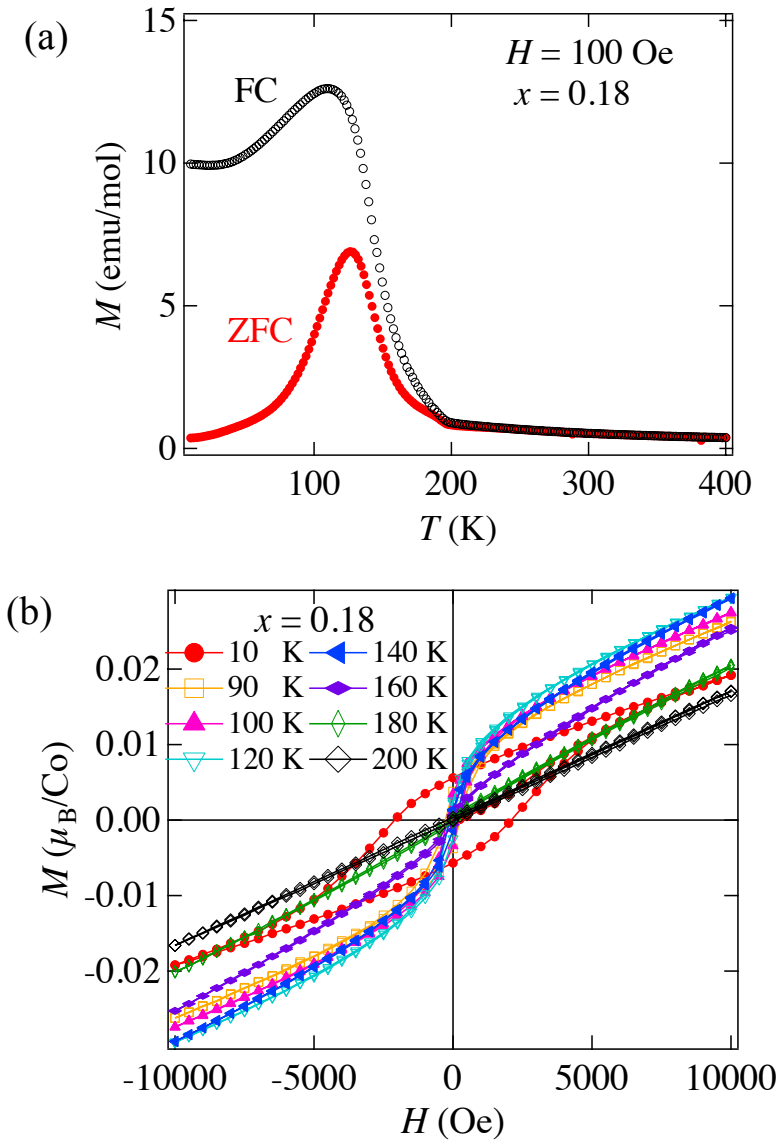

Fig. 3.1.5. (a) Temperature dependence of magnetization for $La_{0.5}Ba_{0.5}CoO_{3-x}$ (x = 0.18) under 100 Oe in the ZFC and FC processes respectively. (b) M/H curve at different temperature.

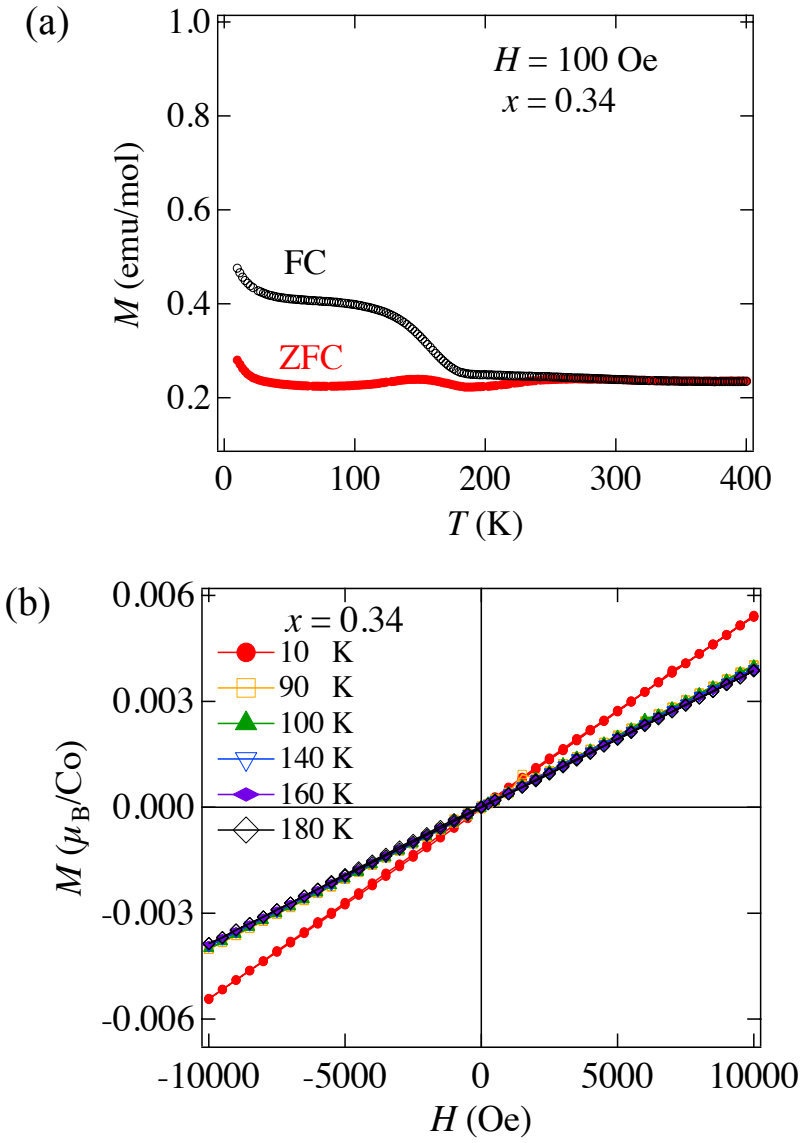

Fig. 3.1.6. (a) Temperature dependence of magnetization for $La_{0.5}Ba_{0.5}CoO_{3-x}$ (x = 0.34) under 100 Oe in the ZFC and FC processes respectively. (b) M/H curve at different temperature.

3.2 NPD patterns and crystal structure analysis

The NPD patterns of $La_{0.5}Ba_{0.5}CoO_{3-x}$ were collected by SuperHRPD from 13K to room temperature. The NPD patterns of $La_{0.5}Ba_{0.5}CoO_{3-x}$ (x=0.09) were shown in Fig. 3.2.1. According to the magnetization data, at room temperature the sample is in the paramagnetic state and only nuclear crystal structure contributes to the diffraction pattern. Therefore, the

room-temperature pattern of the sample can be described solely by the nuclear crystal structure. The Rietveld refinement leads to the cubic structure of the space group $Pm\bar{3}m$ with $\chi^2 = 1.44$, as shown in Fig. 3.2.2(a). No additional peak or peak splitting is observed at base temperature, indicating that the crystal structure does not change and remains in one phase with the cubic structure of space group $Pm\bar{3}m$ during the whole temperature range. The increase of the intensity of reflection (1 0 0) upon cooling, suggests the ferromagnetic state with propagation vector $\boldsymbol{k_F} = (0, 0, 0)$.

Fig. 3.2.3, Fig. 3.2.5 and Fig. 3.2.7 show the NPD patterns of $La_{0.5}Ba_{0.5}CoO_{3-x}$ ($x = 0.11$, 0.13 and 0.14) measuring from 13K to room temperature. Fig. 3.2.9 shows the NPD patterns of $La_{0.5}Ba_{0.5}CoO_{3-x}$ ($x = 0.18$) measuring from 13K to 543K. At highest temperature the patterns of all the samples show single phase. The patterns can be fitted well by the cubic structure of the space group $Pm\bar{3}m$ with $\chi^2 = 2.10$, 1.54, 1.50 and 2.22 for the sample $x = 0.11$, 0.13, 0.14 and 0.18, respectively, as shown in Fig. 3.2.4(a), Fig. 3.2.6(a), Fig. 3.2.8(a) and Fig. 3.2.10(a).

However, as the temperature decreases, the diffraction peak becomes asymmetric and broader. By merit of the high resolution of BS bank, we can observe the peak splitting initiates from about 162, 179, 199 and 323 K for the sample $x = 0.11$, 0.13, 0.14 and 0.18, respectively, as shown in Fig. 3.2.3, Fig. 3.2.5, Fig. 3.2.7 and Fig. 3.2.9. The unusual peak splitting is occurred in all Bragg peaks, which reveals the appearance of a new phase with unit cell parameter larger than that for the parent phase. The Rietveld refinements are greatly improved by using two phases (large-volume (LV) phase and small-volume (SV) phase with different unit cell parameters) with cubic structure of space group $Pm\bar{3}m$. It can be considered that the crystal structures of all the samples keep in the cubic structure of space group $Pm\bar{3}m$ during the whole temperature range.

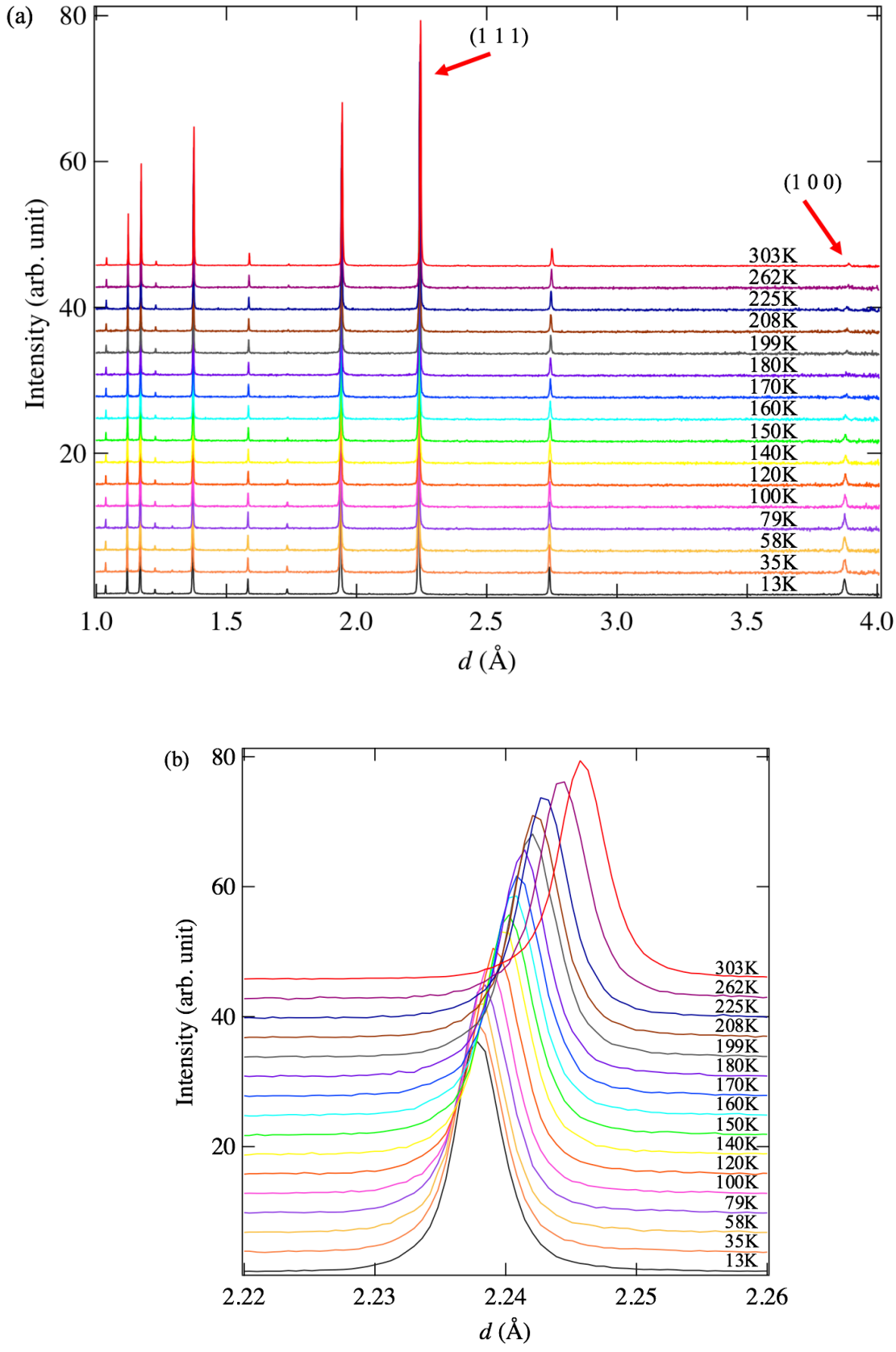

Fig. 3.2.1. (a) NPD patterns and (b) 111 reflection of $La_{0.5}Ba_{0.5}CoO_{3-x}$ (x=0.09) sample by high-angle bank.

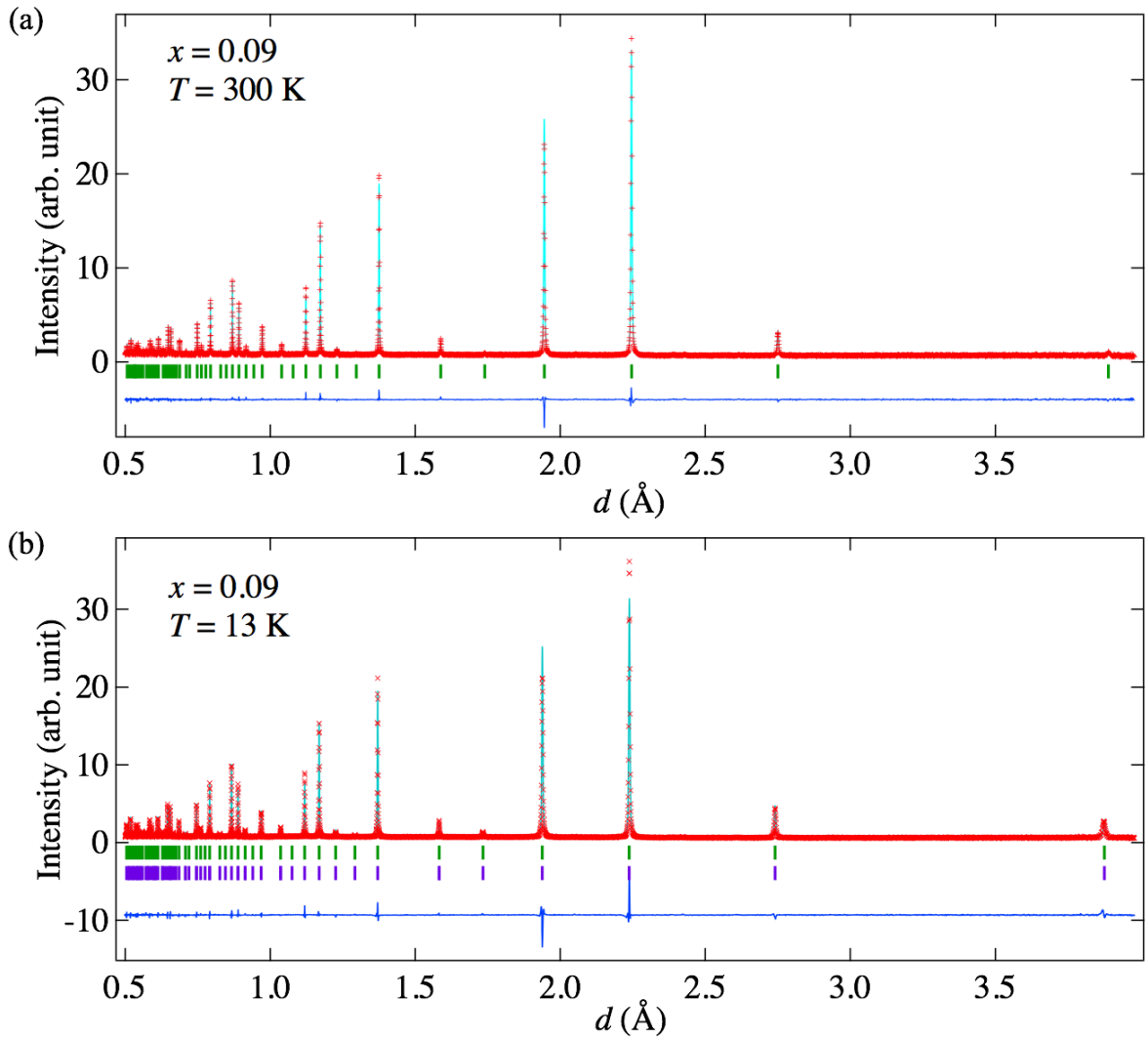

Fig. 3.2.2. The NPD patterns of $La_{0.5}Ba_{0.5}CoO_{3-x}$ (x = 0.09) at (a) 300K and (b) 13K refined by the Rietveld method. The observed and calculated patterns are shown at the top with the cross markers and the solid line, respectively. The vertical green and purple marks in the middle show positions calculated of Bragg reflections for nuclear and magnet diffraction, respectively. The bottom blue line represents the difference between observed and calculated intensities.

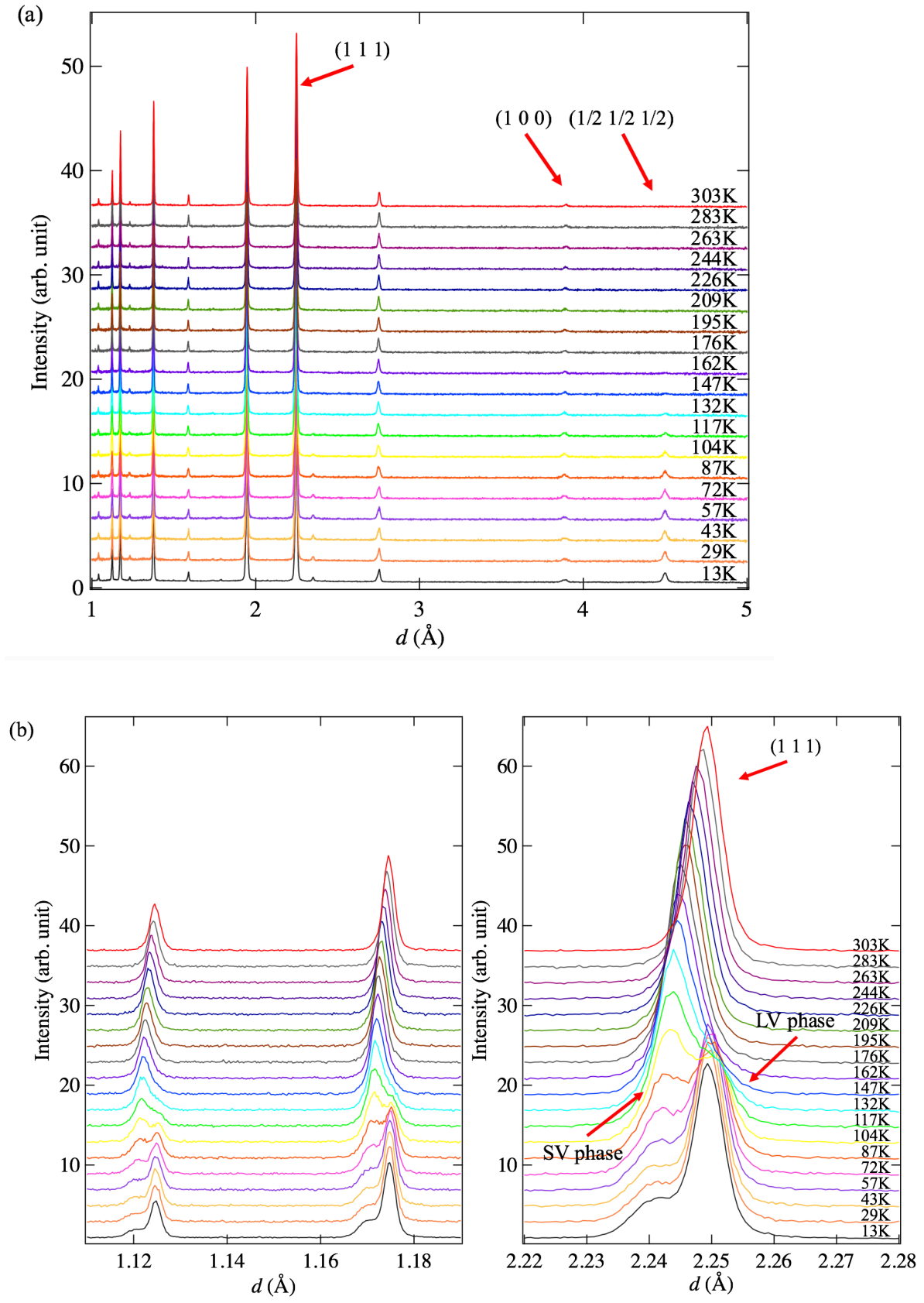

Fig. 3.2.3. (a) NPD patterns of $La_{0.5}Ba_{0.5}CoO_{3-x}$ (x = 0.11) sample collected by 90degree bank, (b) the magnified parts of the patterns at selected d range by high-angle bank.

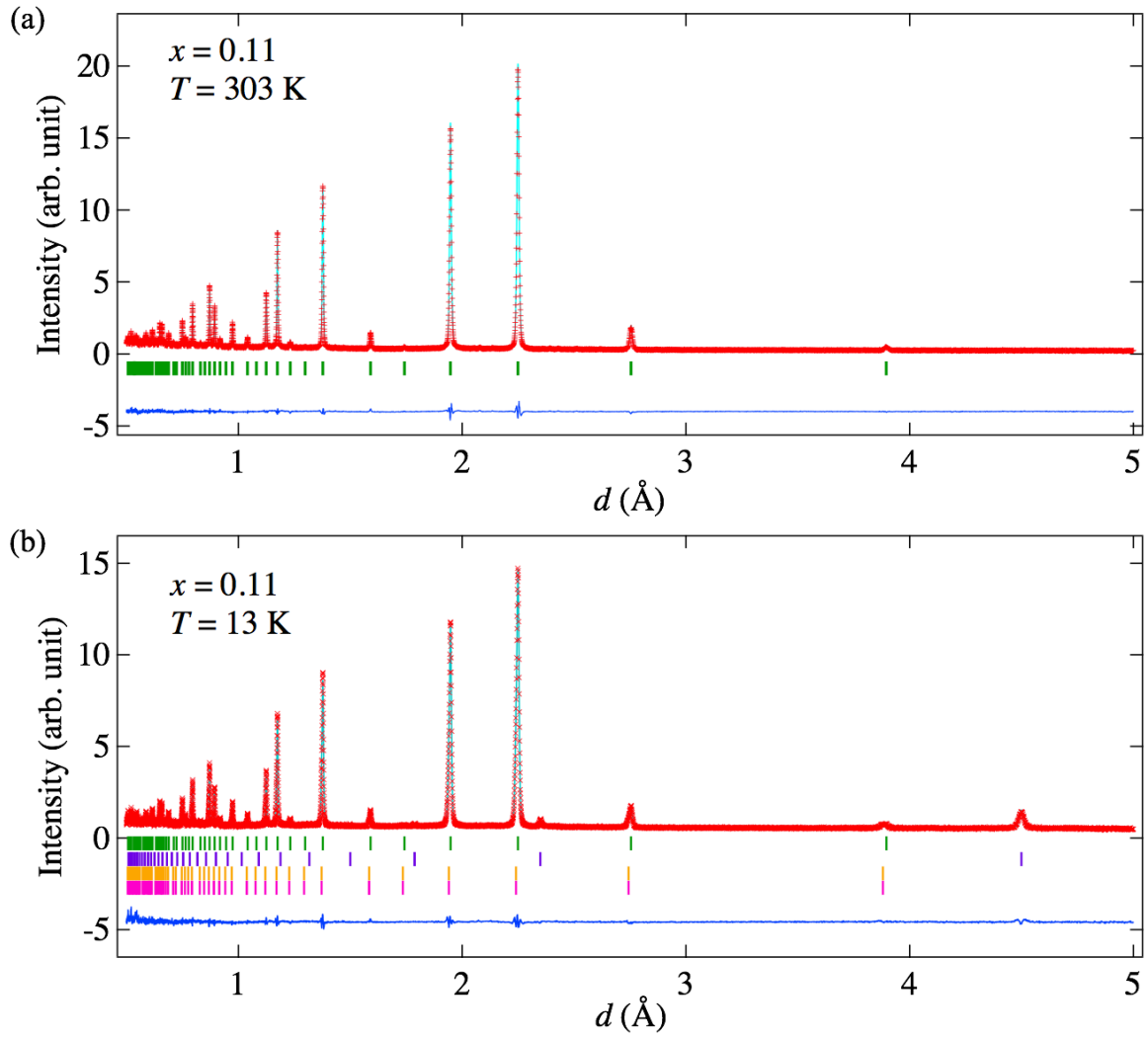

Fig. 3.2.4. Rietveld refinement on the patterns of $La_{0.5}Ba_{0.5}CoO_{3-x}$ (x = 0.11) at (a) 303K by one phase and (b) 13K by the model of double phase (LV and SV). The observed and calculated patterns are shown at the top with the cross markers and the solid line, respectively. At (a) the vertical green marks in the middle show positions calculated of Bragg reflections for nuclear. At (b) the vertical green (purple) marks in the middle denote the indices from nuclear (magnetic) structures of LV phase while the vertical orange (magenta) marks represent the indices from nuclear (magnetic) structures of SV phase. The bottom blue line represents the difference between observed and calculated intensities.

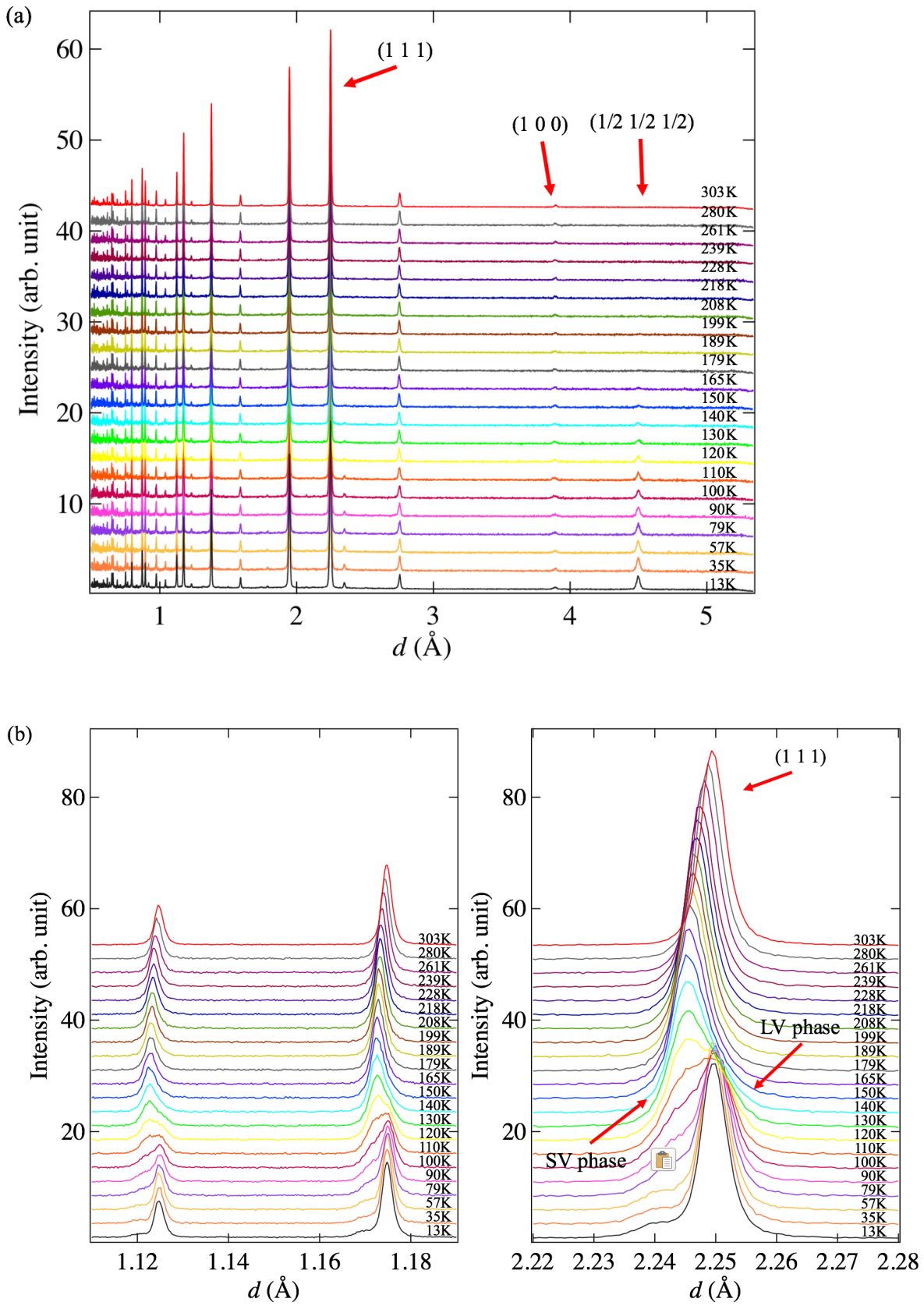

Fig. 3.2.5. (a) NPD patterns of $La_{0.5}Ba_{0.5}CoO_{3-x}$ ($x = 0.13$) sample collected by 90degree bank, (b) the magnified parts of the patterns at selected d range by high-angle bank.

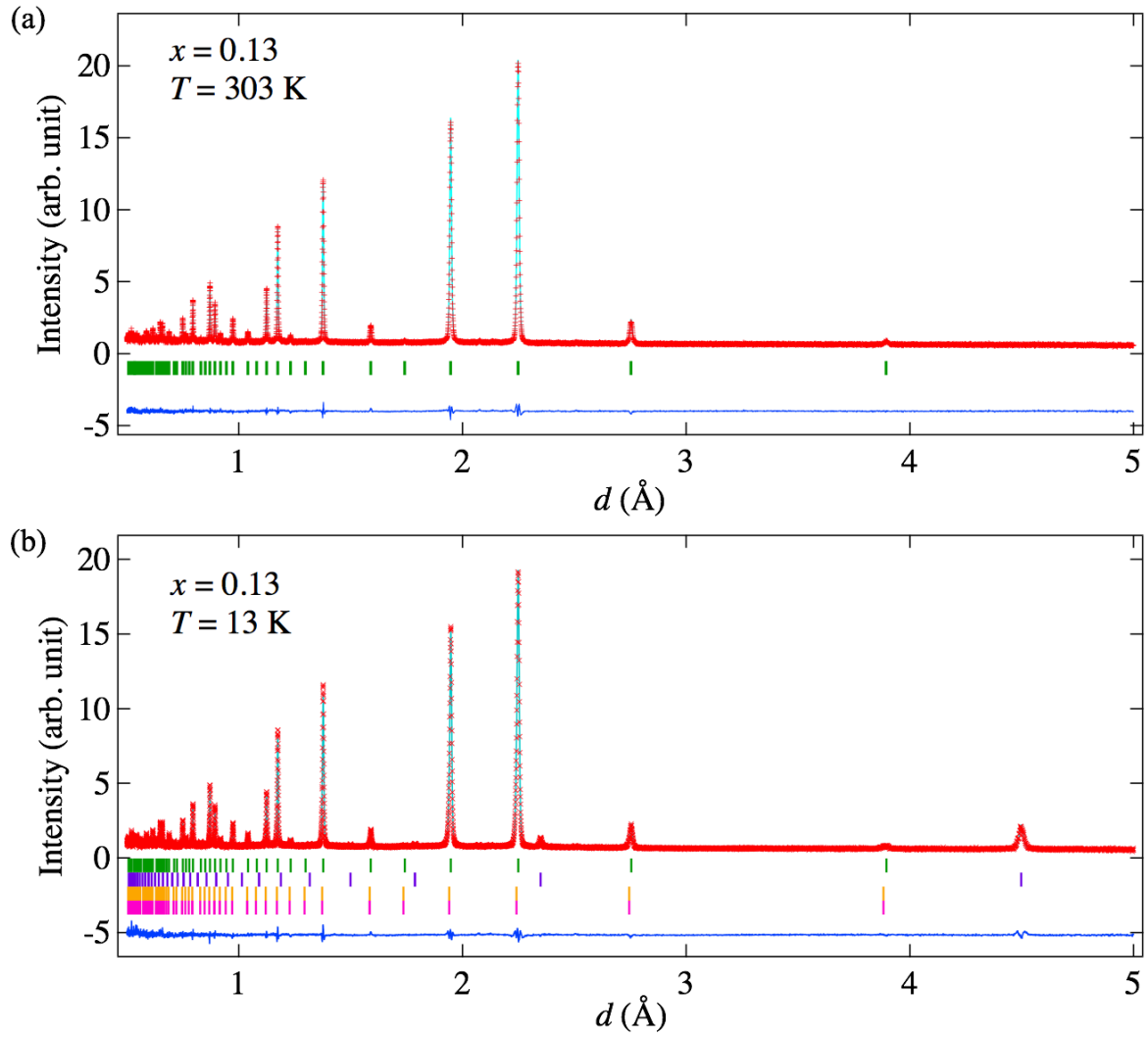

Fig. 3.2.6. Rietveld refinement on the patterns of $La_{0.5}Ba_{0.5}CoO_{3-x}$ (x = 0.13) at (a) 303K by one phase and (b) 13K by the model of double phase (LV and SV). The observed and calculated patterns are shown at the top with the cross markers and the solid line, respectively. At (a) the vertical green marks in the middle show positions calculated of Bragg reflections for nuclear. At (b) the vertical green (purple) marks in the middle denote the indices from nuclear (magnetic) structures of LV phase while the vertical orange (magenta) marks represent the indices from nuclear (magnetic) structures of SV phase. The bottom blue line represents the difference between observed and calculated intensities.

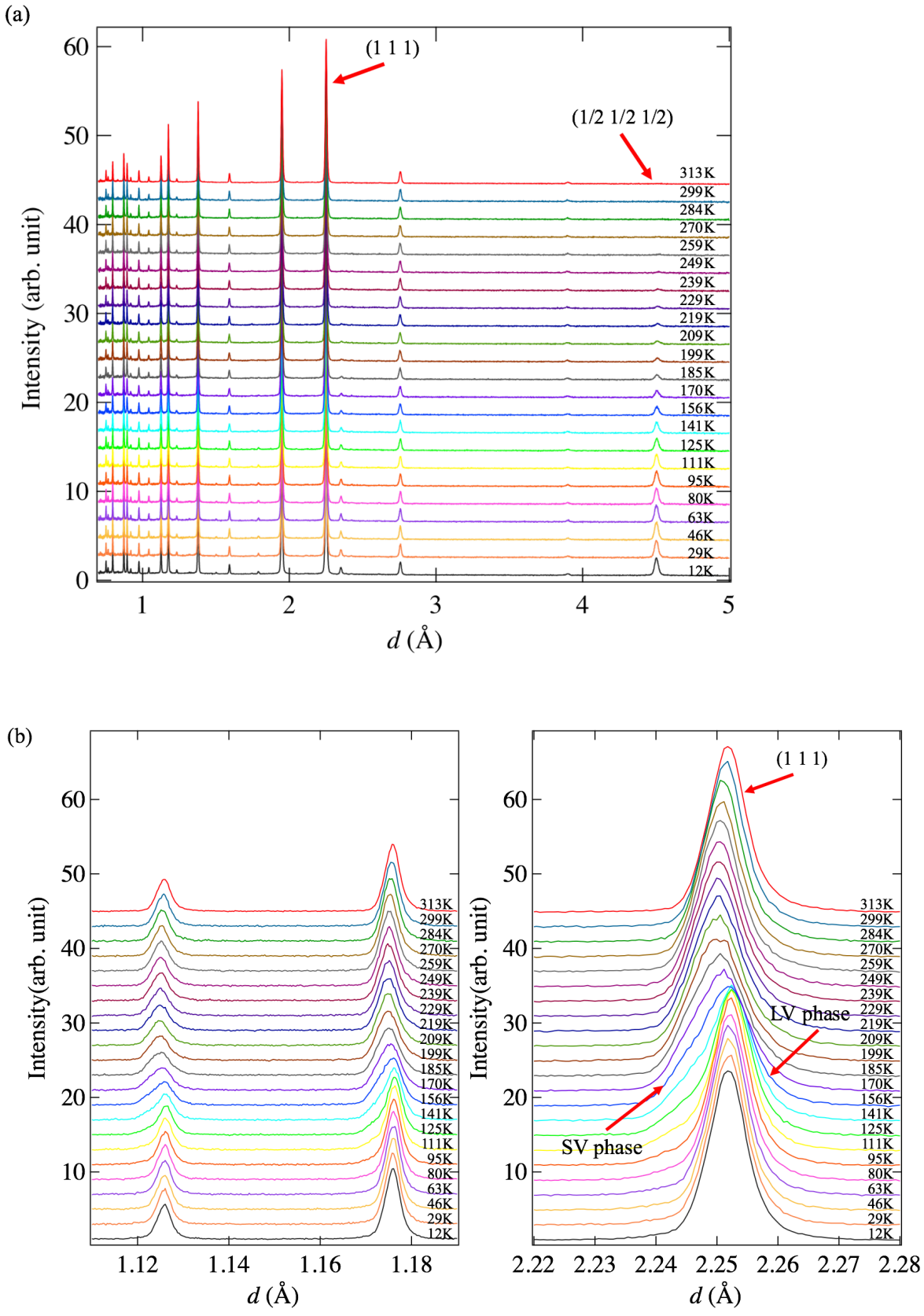

Fig. 3.2.7. (a) NPD patterns of $La_{0.5}Ba_{0.5}CoO_{3-x}$ ($x = 0.14$) sample collected by 90degree bank, (b) the magnified parts of the patterns at selected d range by high-angle bank.

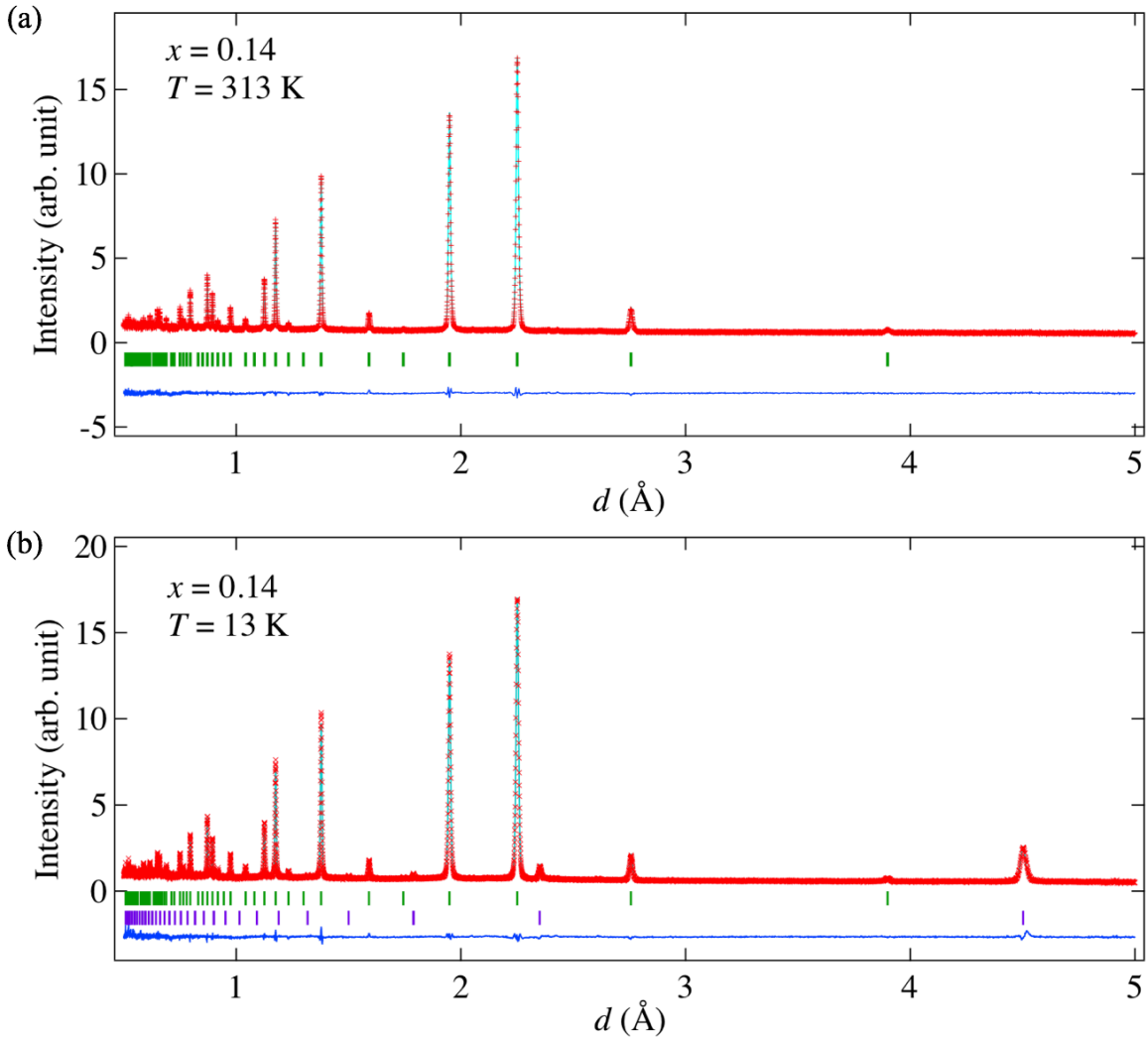

Fig. 3.2.8. Rietveld refinement on the patterns of $La_{0.5}Ba_{0.5}CoO_{3-x}$ (x = 0.14) at (a) 313K and (b) 13K. The observed and calculated patterns are shown at the top with the cross markers and the solid line, respectively. The vertical green and purple marks in the middle show positions calculated of Bragg reflections for nuclear and magnet diffraction, respectively. The bottom blue line represents the difference between observed and calculated intensities.

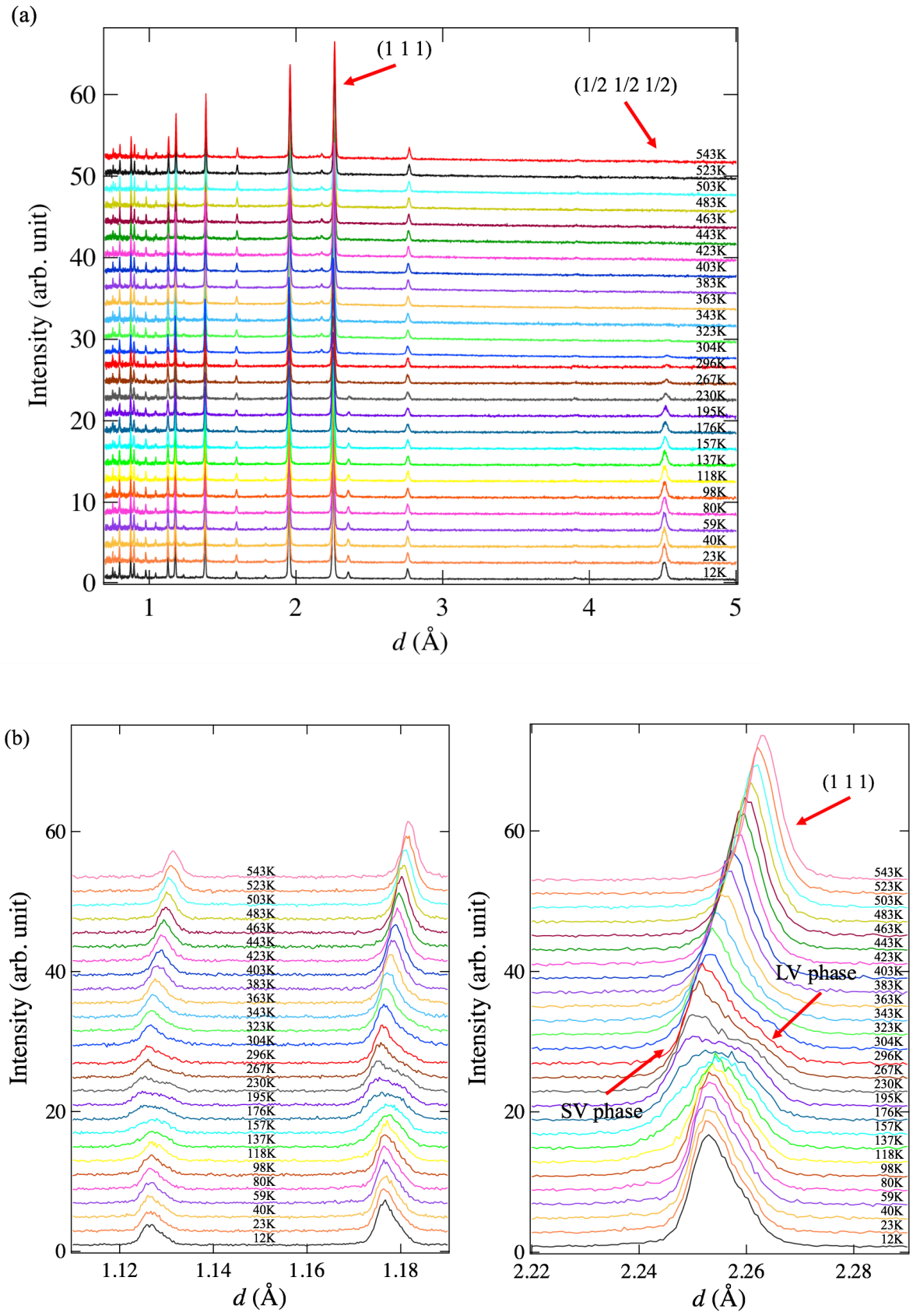

Fig. 3.2.9. (a) NPD patterns of $La_{0.5}Ba_{0.5}CoO_{3-x}$ (x = 0.18) sample collected by 90degree bank, (b) the magnified parts of the patterns at selected d range by high-angle bank.

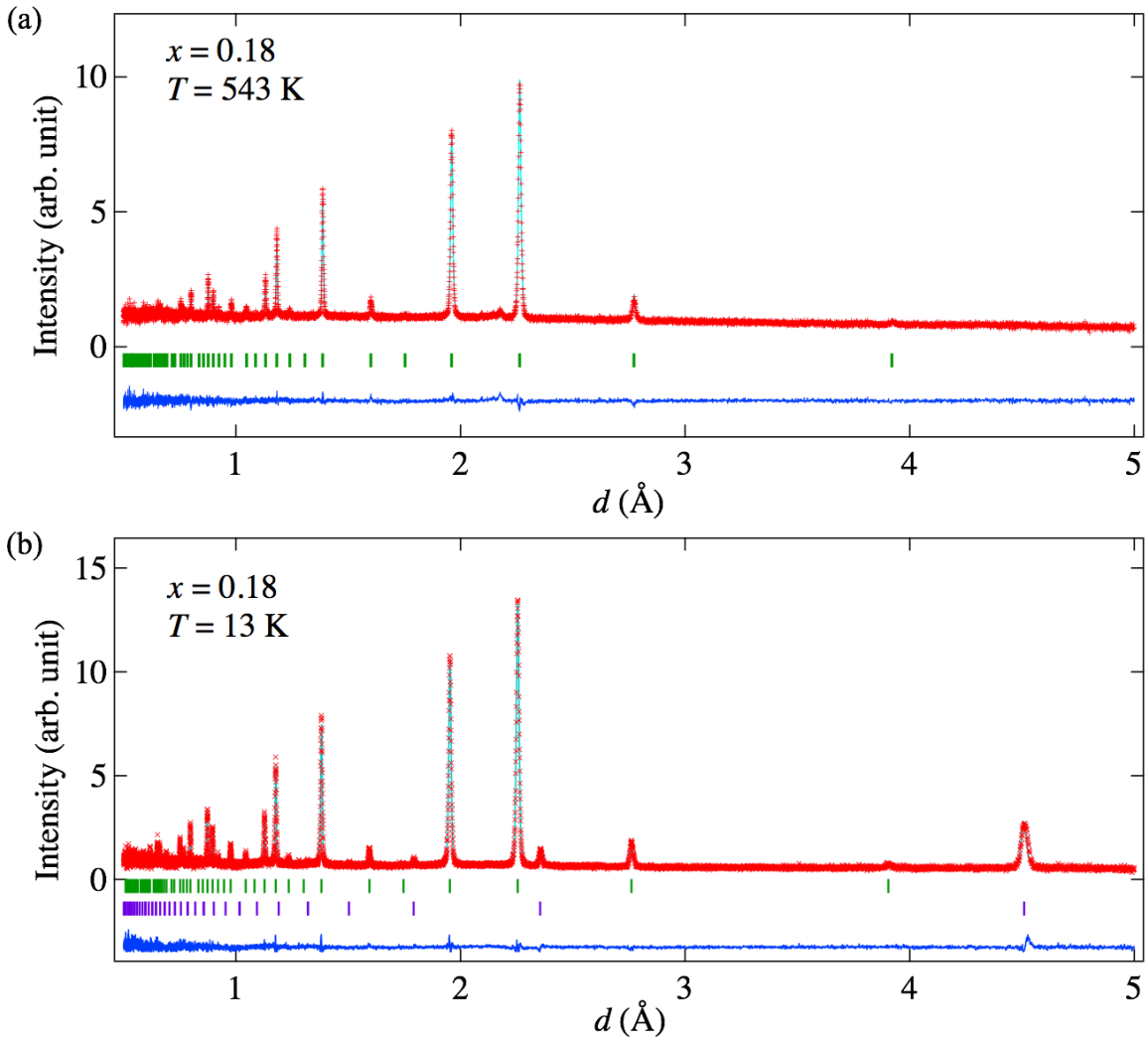

Fig. 3.2.10. Rietveld refinement on the patterns of $La_{0.5}Ba_{0.5}CoO_{3-x}$ (x = 0.18) at (a) 296K and (b) 13K. The observed and calculated patterns are shown at the top with the cross markers and the solid line, respectively. The vertical green (purple) marks in the middle denote the indices from nuclear (magnetic) structures of LV phase while the vertical orange marks represent the indices from nuclear structures of SV phase. The bottom blue line represents the difference between observed and calculated intensities.

3.3 Magnetic structure analysis

In this part, the magnetic transition temperature and magnetic structure are analyzed. The magnetic transition temperature is estimated from the integrated intensity of magnetic

reflection. The integrated intensity is calculated by summarizing the intensity of the magnetic peak and subtracting the intensity of background. The average intensity of background is calculated by averaging 10 points below and above the magnetic peak.

From the temperature-dependent NPD pattern of x = 0.09, the magnetic reflection (1 0 0) is observed at low temperature. The transition temperature T_C = 160 K for x = 0.09 are estimated from the temperature dependence of integrated intensity of the magnetic reflection (1 0 0), as shown in Fig. 3.3.1. The increase of the magnetic reflection (1 0 0) intensity in $La_{0.5}Ba_{0.5}CoO_{3-x}$ (x = 0.09) upon cooling, indicates the ferromagnetic state with propagation vector $\boldsymbol{k}$ = (0, 0, 0) initiates from T_C =170 K.

Using the $Pm\bar{3}m$ cubic crystal structure and magnetic propagation vector $\boldsymbol{k}$, we carried out the symmetry analysis for the magnetic structures based on the representation theory. We first determined the space group symmetry elements, g, which leaves the propagation vector $\boldsymbol{k}$ invariant. These elements form the little group G_k. Then the magnetic representation of a crystallographic site can be decomposed in terms of the irreducible representations (IRs) of G_k:

$$\Gamma_{Mag} = \sum n_\upsilon \Gamma_\upsilon^\mu, \qquad (1)$$

where n_υ is the number of times that the IR Γ_υ of order μ appears in the magnetic representation Γ_{Mag} for the Co crystallographic site (0.5, 0.5, 0.5). According to Landau theory, the magnetic ordering from a second-order phase transition will condense to a single IR. So the symmetry-allowed magnetic structures corresponds to the non-zero ($n_\upsilon \neq 0$) IRs of G_k, from which we can calculated its magnetic basis vectors, ψ_n. The whole calculation was performed using the program *Sarah* [82].

We perform the symmetry analysis with propagation vector $\boldsymbol{k}$ = (0, 0, 0) for x = 0.09. The resultant non-zero IRs and the corresponding basis vectors, ψ_n are presented in Table 3.3.1. Next we carried out the Rietveld refinement using the different combinations of ψ_n so as to determine the magnetic structure. The result of Rietveld refinement using the different combinations of ψ_n are listed in Table 3.3.2 and fitted pattern is shown in Fig. 3.2.2(b). Finally, the simple FM structure with all the Co-ion spins pointing along the same direction was found for x = 0.09 as depicted in Fig. 3.3.7(a). However, we cannot determine the spin orientation by neutron powder diffraction (Table 3.3.2). In the NPD pattern of $La_{0.5}Ba_{0.5}CoO_{3-x}$ (x = 0.09) at base temperature we could not observe reflections (1/2 1/2 1/2) and (3/2 1/2 1/2). So there is

no long-range ordered AFM state at base temperature in this sample. It has been reported that FM state and small AFM clusters coexist in ground state in $La_{0.5}Ba_{0.5}CoO_{3-x}$ (x = 0) [81]. In case of x = 0.09, a short-range ordered AFM state, which cannot be detected by NPD, may coexist with the long-range ordered FM state at base temperature as well. In order to clarify whether there is short-range ordered AFM state at base temperature, further experiments are needed, such as the muon-spin-relaxation experiment.

For the sample x = 0.11, the reflection (1 0 0) intensity of the small-volume (SV) phase with small unit cell parameter increases upon cooling. This indicates the ferromagnetic state with propagation vector $\boldsymbol{k_F}$ = (0, 0, 0) exist at base temperature. The transition temperature T_C = 160 K is estimated from the temperature dependence of integrated intensity of the FM reflection (1 0 0), as shown in Fig. 3.3.2(a). At base temperature we also observed an appearance of new small peaks strongly separated from the basic peaks described by space group $Pm\bar{3}m$. The additional peaks appearing at base temperature can be well indexed with $2a_p \times 2a_p \times 2a_p$ supercell where a_p is unit cell parameter for the large-volume (LV) phase with larger unit cell parameter. This indicates that the magnetic structure associated with the LV phase is G-type antiferromagnetic structure. The superlattice reflections (1/2 1/2 1/2) initiating at about 170 K upon cooling signify the magnetic ordering with propagation vector $\boldsymbol{k_{AF}}$ = (1/2, 1/2, 1/2). The transition temperature T_N = 164 K is estimated from the temperature dependence of integrated intensity of the AF reflection (1/2 1/2 1/2), as shown in Fig. 3.3.2(b).

Using the $Pm\bar{3}m$ cubic crystal structure and magnetic propagation vector of the two phases, we carried out the symmetry analysis for the magnetic structures based on the representation theory. The non-zero IRs and the corresponding basis vectors for small-volume phase with FM (FSV) and large-volume phase with AFM (AFLV) phase are given in Table 3.3.3 and Table 3.3.4, respectively. Next we carried out the Rietveld refinement using the different combinations of basis vectors so as to determine the magnetic structure. The results for the refinement are listed in Table 3.3.5 and Table 3.3.6. The whole pattern can be refined well by the combination of FSV and AFLV phases with χ^2 = 1.89, as shown in Fig. 3.2.4(b). Finally, the simple FM structure and the G-type AFM structure were found for FSV and AFLV, respectively, as depicted in Fig. 3.3.7(a) and (b). However, the spin orientation cannot be identified from neutron powder diffraction (Table 3.3.5 and 3.3.6). In the simple FM structure all the Co-ion spins point along the same direction, as depicted in Fig. 3.3.7(a). In the G-type AFM structure, every Co ion aligns antiparallelly with the nearest Co neighbors, as shown in

Fig. 3.3.7(b). The estimated magnetic moment is around 1.12 μ_B /Co for the ferromagnetic phase and 1.23 μ_B /Co for the antiferromagnetic phase.

For the sample $La_{0.5}Ba_{0.5}CoO_{3-x}$ (x = 0.13), at base temperature the phase separation of AFLV and FSV phase are observed in the pattern of high-resolution NPD, as shown in Fig. 3.2.5(a). All the nuclear reflections such as (1 1 1), split while the AF reflection (1/2 1/2 1/2) coexists with the F reflection (1 0 0) at base temperatures. The magnetic propagation vector for the AFLV and FSV phases are $\boldsymbol{k_{AF}}$ = (1/2, 1/2, 1/2) and $\boldsymbol{k_F}$ = (0, 0, 0), respectively. Using the $Pm\bar{3}m$ cubic crystal structure and magnetic propagation vector of the two phases, as shown in Table 3.3.3 and Table 3.3.4, we also performed the symmetry analysis for the magnetic structures based on the representation theory. The whole pattern can be refined well by the combination of FSV and AFLV phases (see Fig. 3.2.6(b)) with χ^2 = 1.92. The F and AF structure models are shown in Fig. 3.3.7(a) and (b), respectively. The estimated magnetic moment is around 0.74 μ_B/Co for the ferromagnetic phase and 1.32 μ_B/Co for the antiferromagnetic phase. The transition temperature T_N = 190 K for x = 0.11 are estimated from the temperature dependence of integrated intensity of the AFM reflection (1/2 1/2 1/2), as shown in Fig. 3.3.3.

In contrast to the samples x = 0.11 and x = 0.13, at base temperature the pattern of x = 0.14 shows only one phase. However, the phase separation of LV and SV phase are observed in the pattern of high-resolution NPD from about 95K, as shown in Fig. 3.2.7(a). The superlattice reflections (1/2 1/2 1/2) initiating at about 260 K upon cooling signify the magnetic ordering with propagation vector $\boldsymbol{k}$ = (1/2, 1/2, 1/2). The transition temperature T_N = 260 K for x = 0.14 are estimated from the temperature dependence of integrated intensity of the AFM reflection (1/2 1/2 1/2), as shown in Fig. 3.3.4. The whole pattern at 13K can be refined well by the combination of cubic space group $Pm\bar{3}m$ and G-type AFM structure with χ^2 = 1.85, as shown in Fig. 3.2.8(b). The AFM structure models are shown in Fig. 3.3.7(b). The estimated magnetic moment is about 1.54 μ_B/Co at 13K. As mentioned above, the magnetization data of the x = 0.14 sample suggests that existence of FM component. Throughout the temperature range, we did not observe any ferromagnetic Bragg peak in the NPD pattern, indicating that there is no long-range ordered FM structure. Therefore, we think the FM state occurs in forms of short range ordering together with a long-range ordered AFM state at base temperature.

The NPD patterns of $La_{0.5}Ba_{0.5}CoO_{3-x}$ (x = 0.18) were shown in Fig. 3.2.9. We can observe the superlattice reflections (1/2 1/2 1/2) in the temperature range from 13K to 323K.

The temperature dependence of integrated intensity of the AFM reflection (1/2 1/2 1/2) is shown in Fig. 3.3.5. The transition temperature T_N = 323 K for x = 0.14 are extracted from the temperature dependence of integrated intensity of the AFM reflection (1/2 1/2 1/2). The magnetic propagation vector is $\boldsymbol{k}$ = (1/2, 1/2, 1/2). At 13K the NPD pattern can be fitted well by the combination of cubic space group $Pm\bar{3}m$ and G-type AFM structure (see the Fig. 3.3.7(a)) with χ^2 = 1.27, as shown in Fig. 3.2.10(b). The estimated magnetic moment is about 1.72 μ_B/Co at 13K. However, the phase separation of LV and SV phase are observed in the pattern of high-resolution NPD from about 150K, as shown in Fig. 3.2.9(b). All the patterns can be refined well by the combination of LV phases with G-type AFM structure and LV phase.

The temperature dependence of integrated intensity of the AFM reflection (1/2 1/2 1/2) for $La_{0.5}Ba_{0.5}CoO_{3-x}$ (x = 0.34) reveals that the transition temperature T_N is above room temperature, as shown in Fig. 3.3.6.

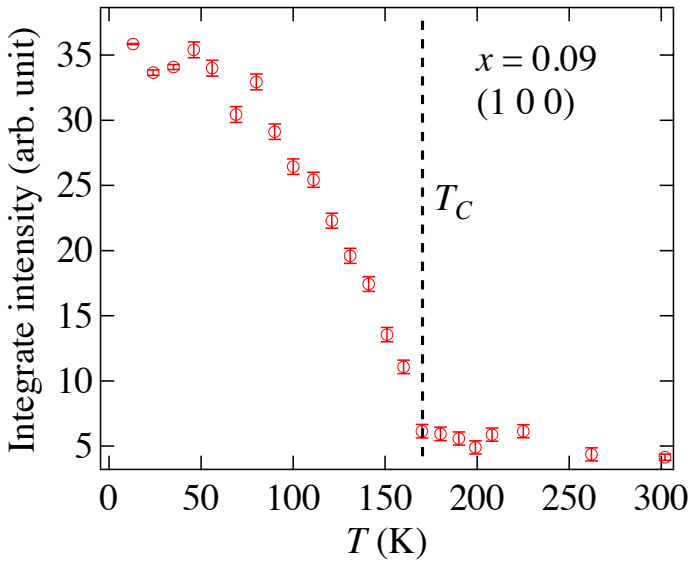

Fig. 3.3.1. The temperature dependence of integrated intensity of the FM reflection (1 0 0) for $La_{0.5}Ba_{0.5}CoO_{3-x}$ (x = 0.09).

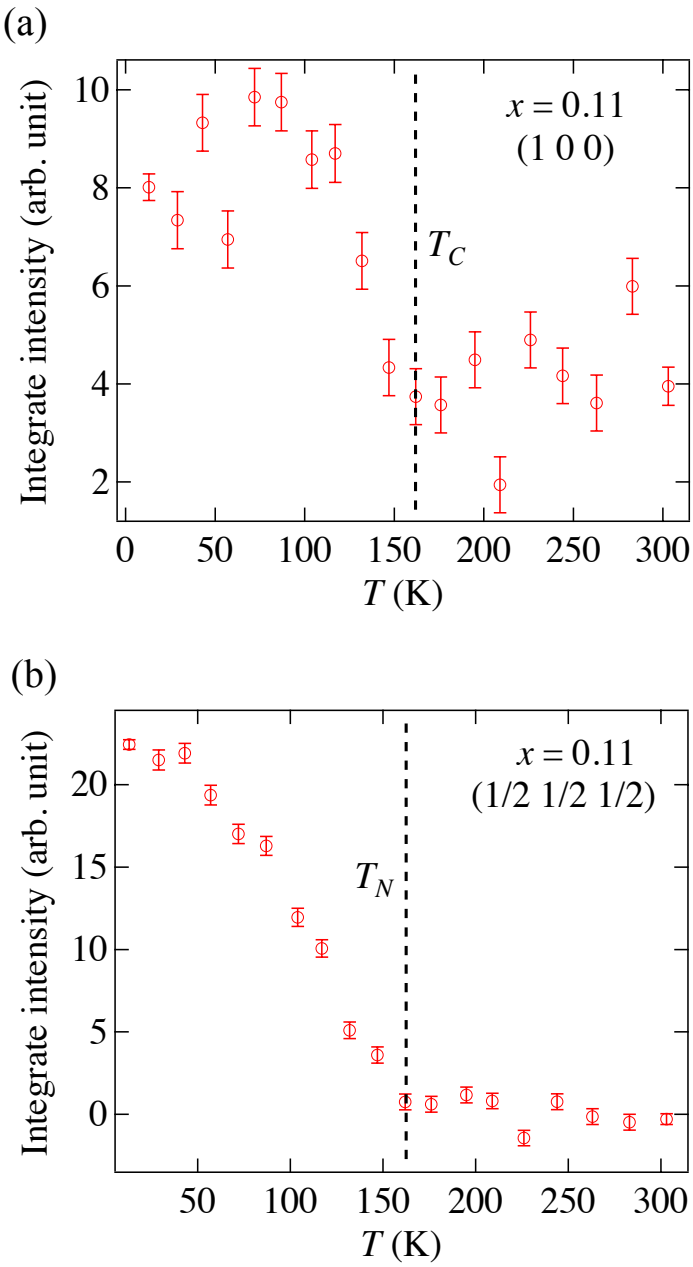

Fig. 3.3.2. The temperature dependence of integrated intensity of (a) the FM reflection (1 0 0) and (b) AFM reflection (1/2 1/2 1/2) for $La_{0.5}Ba_{0.5}CoO_{3-x}$ (x = 0.11).

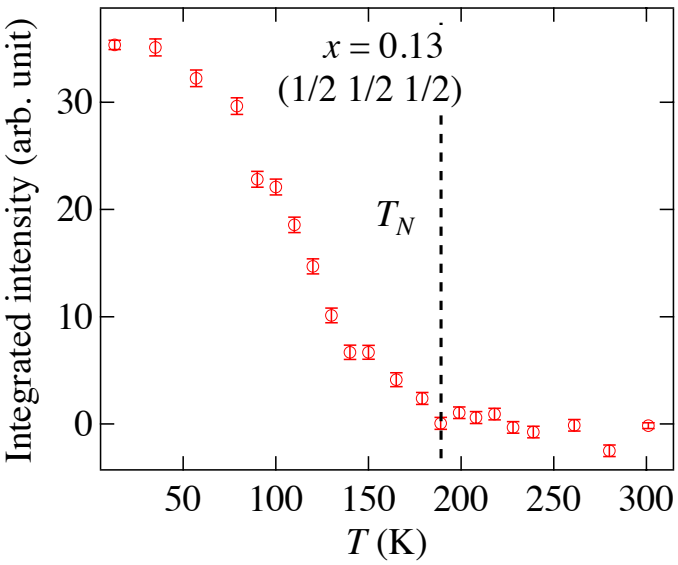

Fig. 3.3.3. The temperature dependence of integrated intensity of the AFM reflection (1/2 1/2 1/2) for $La_{0.5}Ba_{0.5}CoO_{3-x}$ ($x = 0.13$).

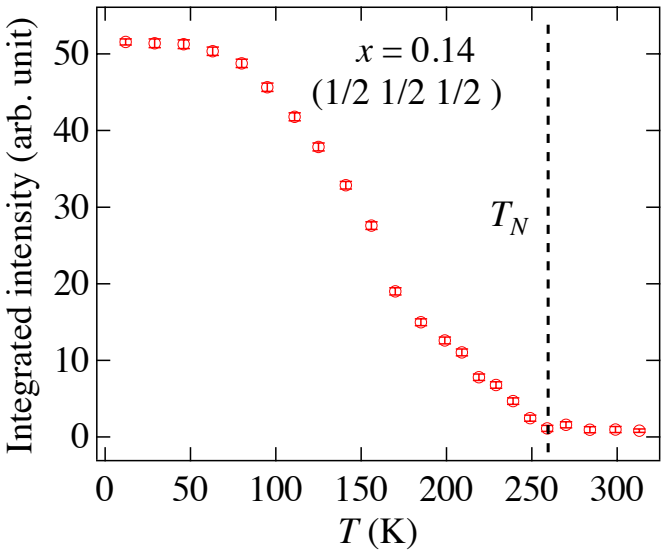

Fig. 3.3.4. The temperature dependence of integrated intensity of the AFM reflection (1/2 1/2 1/2) for $La_{0.5}Ba_{0.5}CoO_{3-x}$ ($x = 0.14$).

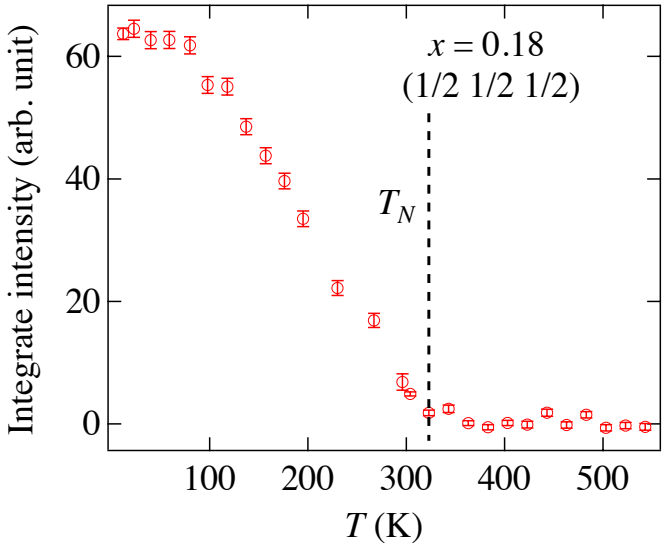

Fig. 3.3.5. The temperature dependence of integrated intensity of the AFM reflection (1/2 1/2 1/2) for $La_{0.5}Ba_{0.5}CoO_{3-x}$ ($x = 0.14$).

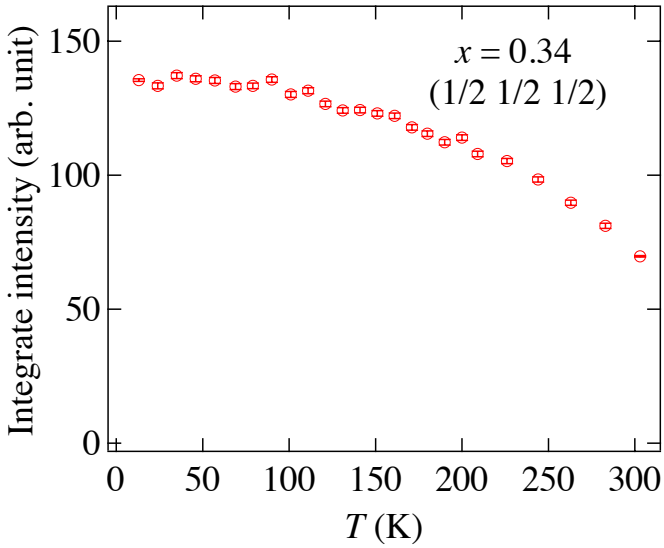

Fig. 3.3.6. The temperature dependence of integrated intensity of the AFM reflection (1/2 1/2 1/2) for $La_{0.5}Ba_{0.5}CoO_{3-x}$ ($x = 0.14$).

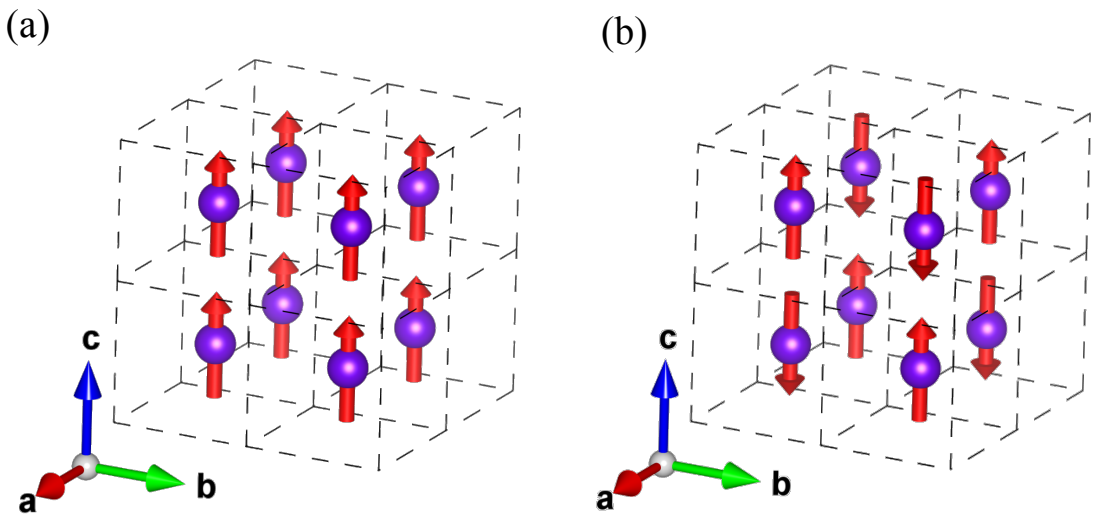

Fig. 3.3.7. The F and AF structure models are shown in Figure (a) and (b), respectively. For clarity only Co is displayed. For clarity only Co is displayed.

Table 3.3.1. The basis vectors of irreducible representations (IRs) for the Co: (0.5, 0.5, 0.5) of the $x = 0.09$ sample. The crystal structure is cubic $Pm\bar{3}m$ and the magnetic propagation vector $\boldsymbol{k}$ is (0, 0, 0).

IRs	Basis Vectors	
	ψ_1	(0 0 1)
Γ_{10}	ψ_2	(1 0 0)
	ψ_3	(0 1 0)

Table 3.3.2. Refined magnetic moments (μ_B) for the Co ion of the $x = 0.09$ sample based on the basis vectors from Table 3.3.1. R_M is the magnetic R factor for Rietveld refinement.

Model	ψ_1	$\psi_1+\psi_2$	$\psi_1+\psi_2+\psi_3$
m_x	0	1.25	1.02
m_y	0	0	1.02
m_z	1.77	1.25	1.02
m_{tot}	1.77	1.77	1.77
R_M (%)	8.40	8.63	8.41

Table 3.3.3. The basis vectors of irreducible representations (IRs) for the Co: (0.5, 0.5, 0.5) of FSV. The crystal structure is cubic $Pm\bar{3}m$ and the magnetic propagation vector $\boldsymbol{k_F}$ is (0, 0, 0).

IRs	Basis Vectors	
	ψ_1	(0 0 1)
Γ_{10}	ψ_2	(1 0 0)
	ψ_3	(0 1 0)

Table 3.3.4. The basis vectors of irreducible representations (IRs) for the Co: (0.5, 0.5, 0.5) of FSV. The crystal structure is cubic $Pm\bar{3}m$ and the magnetic propagation vector $\boldsymbol{k_{AF}}$ is (1/2, 1/2, 1/2).

IRs	Basis Vectors	
	ψ_1	(0 0 1)
Γ_7	ψ_2	(1 0 0)
	ψ_3	(0 1 0)

Table 3.3.5. Refined magnetic moments (μ_B) for the Co ion of AFLV based on the basis vectors from Table 3.3.3. R_M is the magnetic R factor for Rietveld refinement.

Model	ψ_1	$\psi_1+\psi_2$	$\psi_1+\psi_2+\psi_3$
m_x	0	0.79	0.64
m_y	0	0	0.64
m_z	1.12	0.79	0.64
m_{tot}	1.12	1.12	1.12
R_M (%)	31.2	31.1	31.32

Table 3.3.6. Refined magnetic moments (μ_B) for the Co ion of AFLV based on the basis vectors from Table 3.3.4. R_M is the magnetic R factor for Rietveld refinement.

Model	ψ_1	$\psi_1+\psi_2$	$\psi_1+\psi_2+\psi_3$
m_x	0	0.87	0.71
m_y	0	0	0.71
m_z	1.23	0.87	0.71
m_{tot}	1.23	1.23	1.23
R_M (%)	9.80	9.56	9.93

3.4 NTE in $La_{0.5}Ba_{0.5}CoO_{3-x}$

The temperature dependence of volume and thermal expansion coefficient for $La_{0.5}Ba_{0.5}CoO_{3-x}$ (x=0.09) is presented in Fig. 3.4.1. In the whole temperature range the sample x=0.09 remains in single phase and shows positive thermal expansion.

The temperature dependence of unit cell volumes ($a_p \times a_p \times a_p$), mass ratios and thermal expansion coefficient for $La_{0.5}Ba_{0.5}CoO_{3-x}$ (x=0.09, 0.11, 0.13, 0.14 and 0.18) are presented in Fig. 3.4.1 - Fig. 3.4.5. At base temperature, the LV phase with AFM has larger unit cell volume and the SV phase with FM has smaller unit cell volume. They are from the experiment result. The average volume is calculated by $V_{average} = R_{LV} \times V_{LV} + R_{SV} \times V_{SV}$, where R is the mass ratio as shown in the Fig. 3.4.2(b), Fig. 3.4.3(b), Fig. 3.4.4(b) and Fig. 3.4.5(b). For the sample x=0.11, the average volume shrinks as the temperature increase from around 50K to 140K. NTE is observed in the temperature window of about 100 K. At base temperature, the AFLV phase has larger unit cell volume and the FSV phase has smaller unit cell volume. The mass ratio of AFLV and FSV phase is about 69:31. As the temperature increase, the fraction of AFLV phase decreases while the fraction of FSV phase increases. The transition of AFLV phase to FSV phase results in the NTE from around 50K to 140K. From the temperature dependence of thermal expansion coefficient shown in Fig. 3.4.2(c), the largest negative thermal expansion coefficient is $\beta = \frac{dV}{V \times dT}$ =-4.1 $\times 10^{-5}$ K^{-1} at around 70K. This NTE coefficient has the same order of magnitude as the well-known NTE material, such as ZrW_2O_8 (β =−2.7 × 10^{-5} K^{-1}) [16-19], ScF_3 (β =−4.2 × 10^{-5} K^{-1}) [21-23], MnF_3[84]. Moreover, this NTE is isotropic because the cubic structure is maintained down to base temperatures. The other samples (x=0.13, 0.14 and 0.18) shows similar behaviors as the samples x=0.11. They show NTE in the region of coexistence of LV and SV phase. The fraction of AFLV phase decreases while the fraction of FSV phase increases upon heating. The transition of LV phase to SV phase results in the NTE in these samples.

Based on the analysis above, the model of NTE is obtained, shown in Fig. 3.4.6. Both of the LV and SV phases follow the Debye–Grüneisen model [85] which characterizes the phonon contribution. Both of the LV and SV phases display normal positive thermal expansion (PTE) at finite temperatures. The NTE is origin from transition from LV phase to SV phase with increasing temperature.

The temperature dependence of average unit cell volumes and thermal expansion coefficient for the samples $La_{0.5}Ba_{0.5}CoO_{3-x}$ are presented in Fig. 3.4.7. We found NTE in the A-site disordered $La_{0.5}Ba_{0.5}CoO_{3-x}$ samples and the largest NTE is occurred around x = 0.13 with the largest β =-5.7 $\times 10^{-5}$ K^{-1}. This NTE can be tuned by changing the oxygen content. As the oxygen content decreases, the temperature window of the NTE Low thermal expansion (or almost ZTE) is observed in the sample x = 0.18 with a large temperature window from 13K to

room temperature. Furthermore, since these samples remain in cubic structure, the NTE is isotropy. This can be a great advantage. Since the anisotropy NTE will cause microcracking during repeated thermal cycling, the isotropy NTE is more important in the practical use. However, Most of the NTE materials are anisotropic. Thus these samples give us prospect that they can be used in future practical applications.

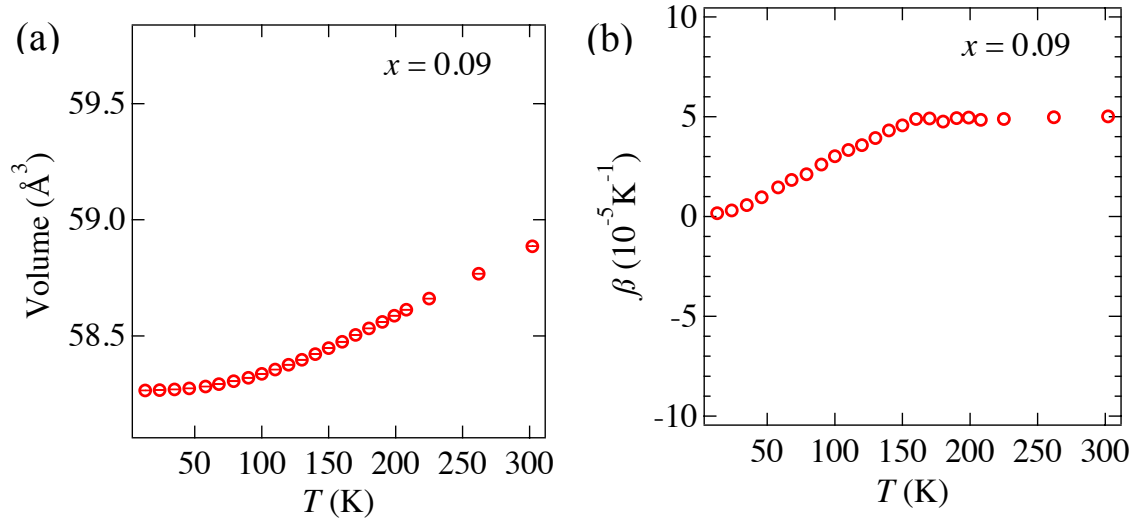

Fig. 3.4.1. The temperature dependence of volume and thermal expansion coefficient for the sample $La_{0.5}Ba_{0.5}CoO_{3-x}$ (x=0.09).

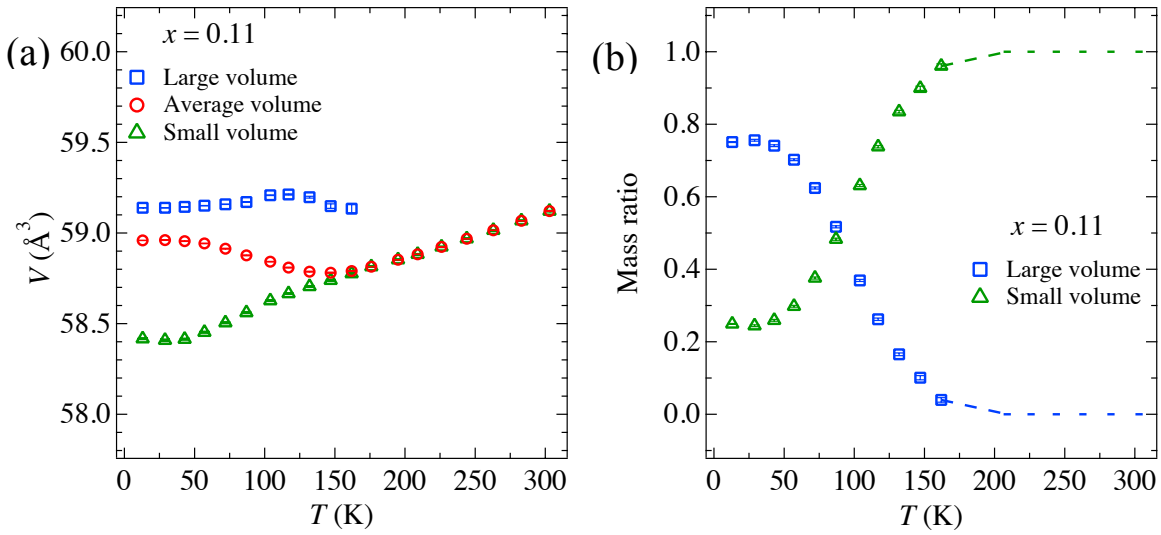

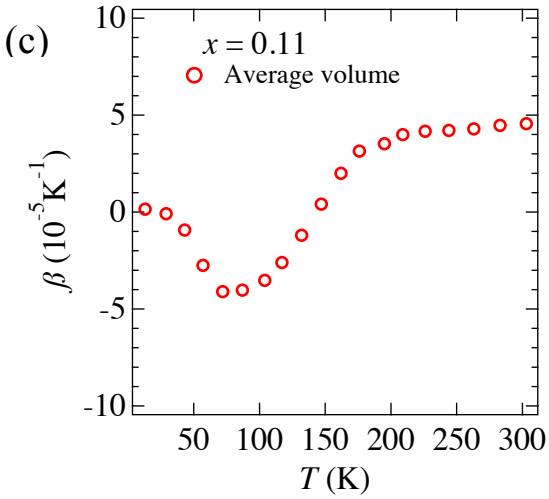

Fig. 3.4.2. The temperature dependence of unit cell volumes (a), mass ratios (b) and thermal expansion coefficient (c) for the sample $La_{0.5}Ba_{0.5}CoO_{3-x}$ (x=0.11).

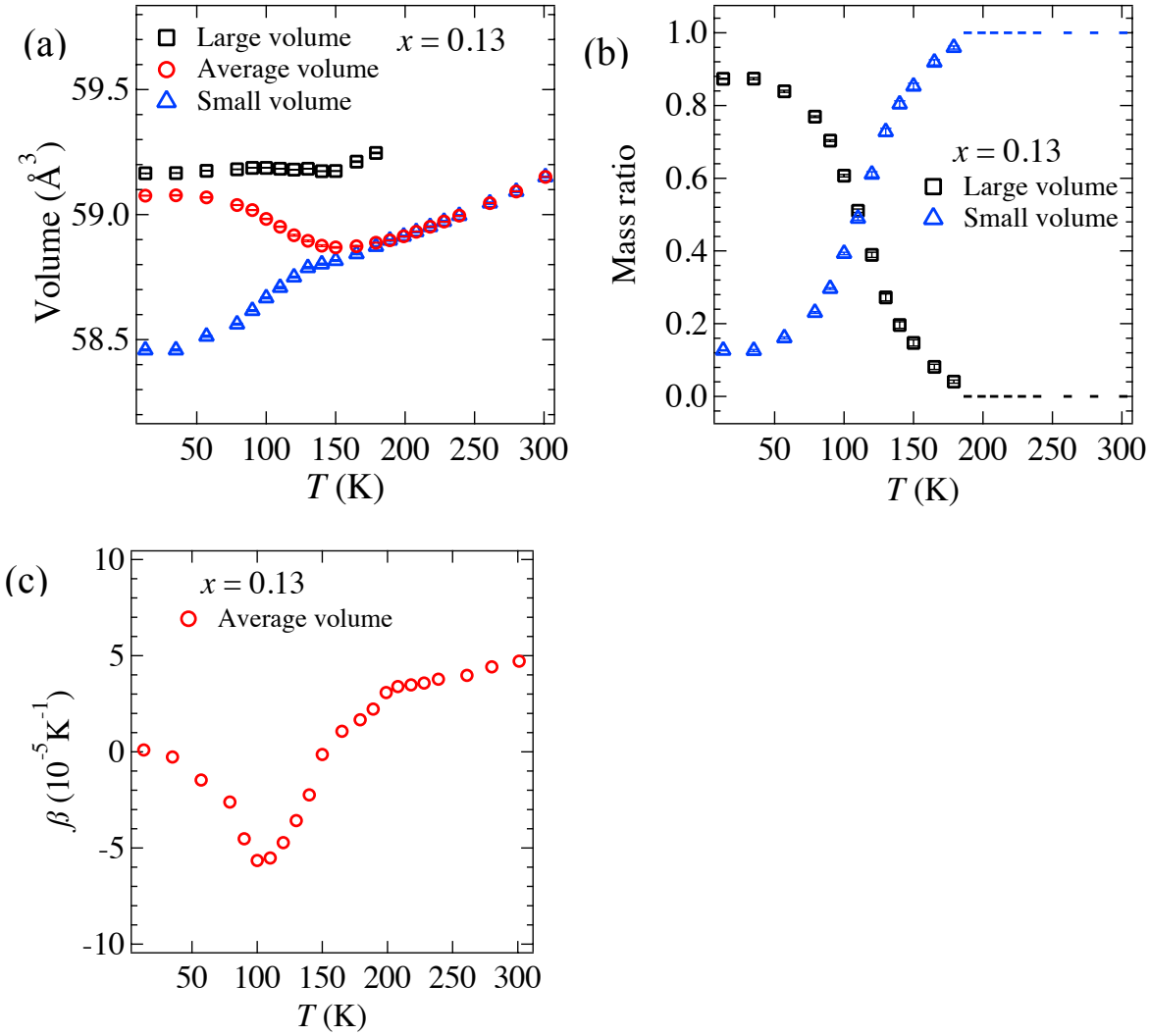

Fig. 3.4.3. The temperature dependence of unit cell volumes (a), mass ratios (b) and thermal expansion coefficient (c) for the sample $La_{0.5}Ba_{0.5}CoO_{3-x}$ (x=0.13).

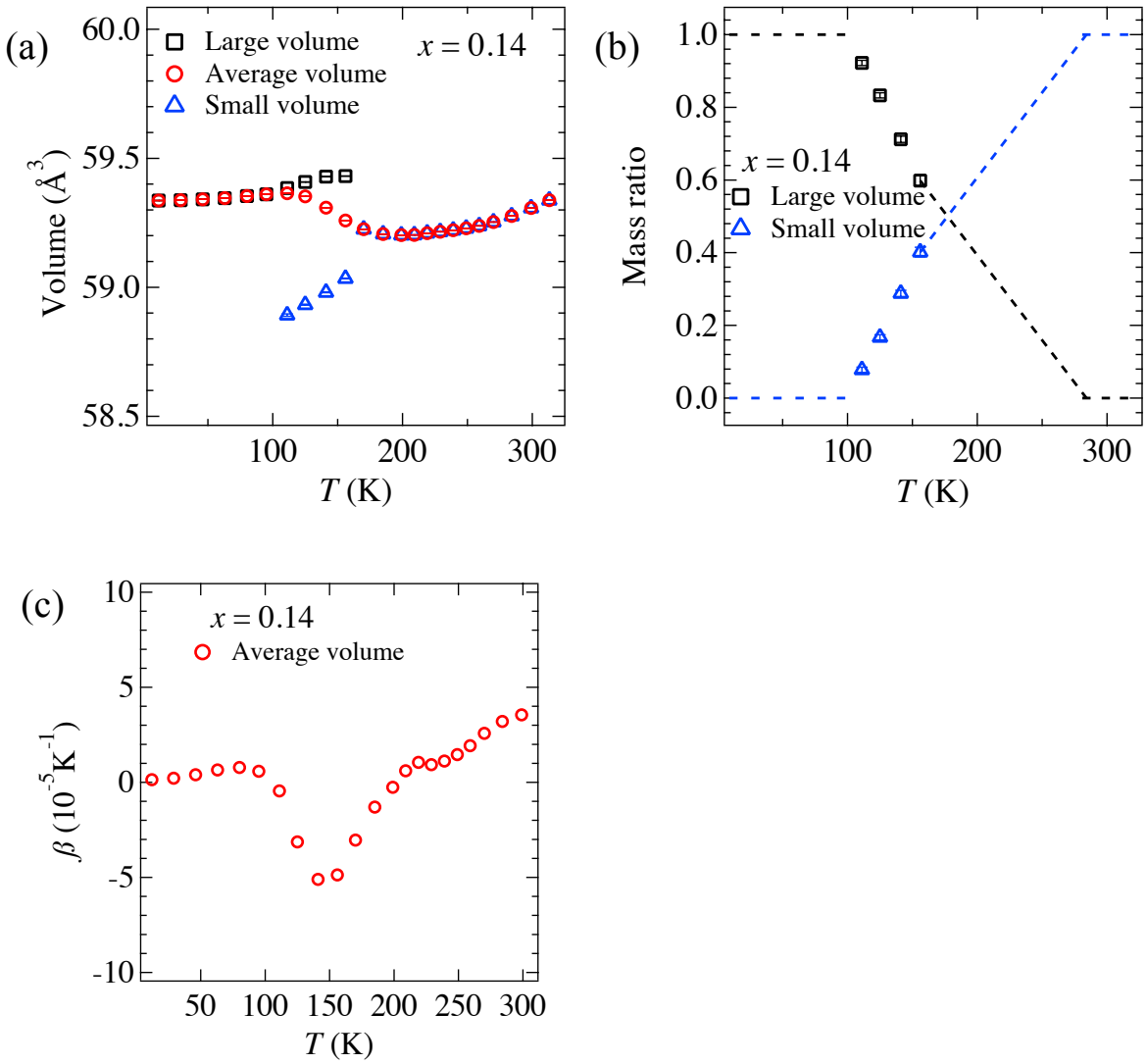

Fig. 3.4.4. The temperature dependence of unit cell volumes (a), mass ratios (b) and thermal expansion coefficient (c) for $La_{0.5}Ba_{0.5}CoO_{3-x}$ ($x = 0.14$).

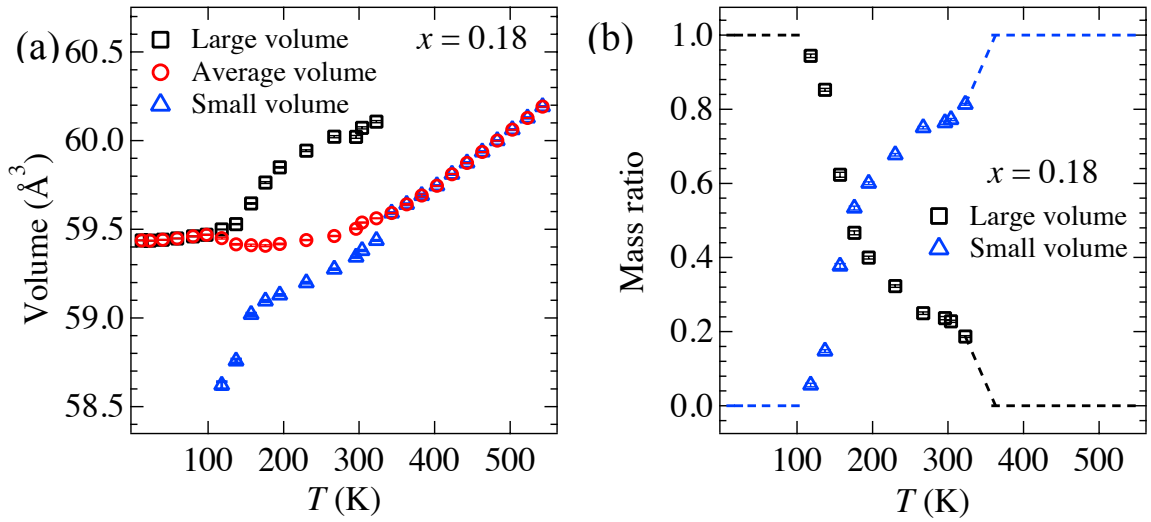

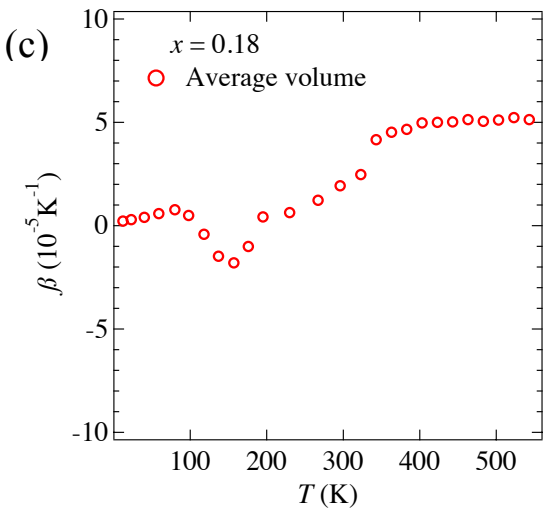

Fig. 3.4.5. The temperature dependence of unit cell volumes (a), mass ratios (b) and thermal expansion coefficient (c) for the sample $La_{0.5}Ba_{0.5}CoO_{3-x}$ (x=0.18).

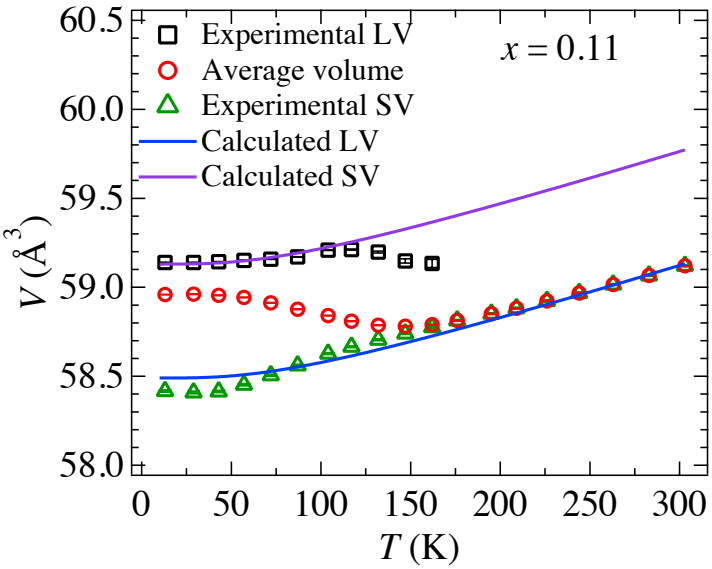

Fig. 3.4.6. The model of NTE for the sample $La_{0.5}Ba_{0.5}CoO_{3-x}$. The blue line and the purple line is calculated by the Debye–Grüneisen model.

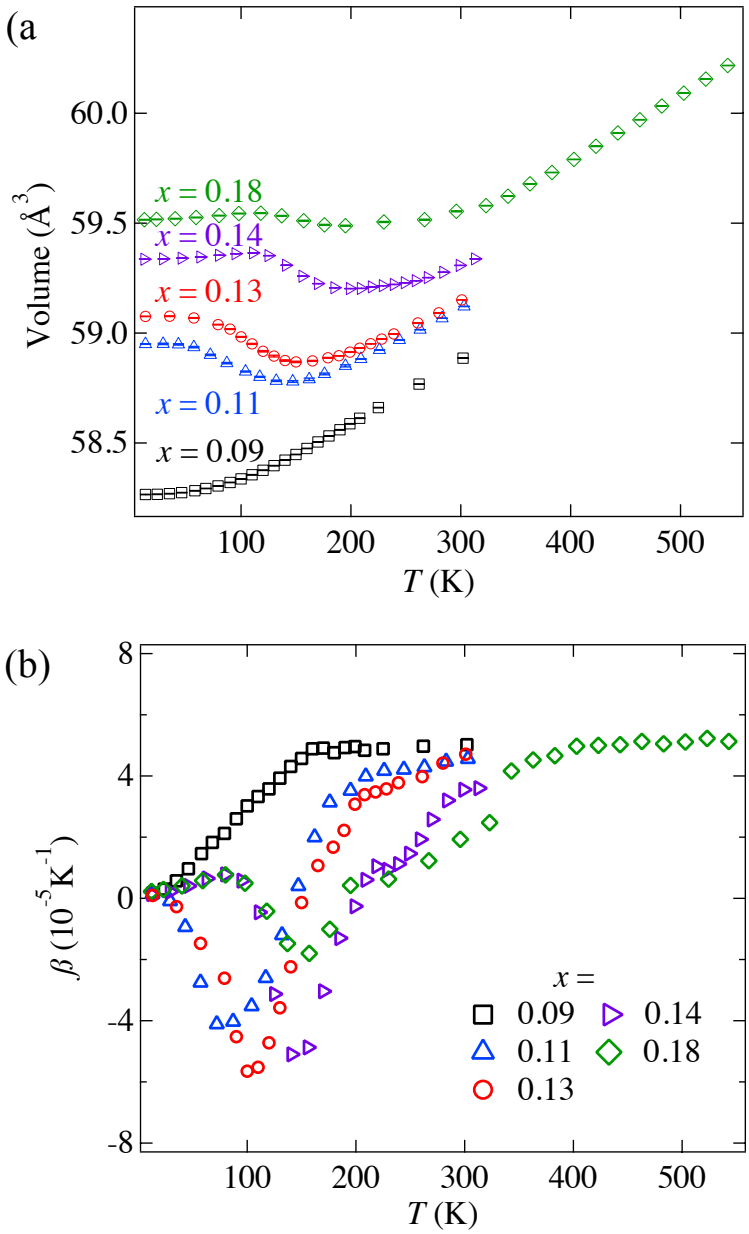

Fig. 3.4.7. The temperature dependence of average unit cell volumes (a) and thermal expansion coefficient (b) for the samples $La_{0.5}Ba_{0.5}CoO_{3-x}$.

3.5 Phase diagram of $La_{0.5}Ba_{0.5}CoO_{3-x}$

Based on the magnetization data and NPD results, the phase diagram figure is obtained, shown in Fig. 3.5.1. At low oxygen content, the ground state of the sample is AFM. At high oxygen content, the ground state of the sample is FM. The sample shows the coexistent of the AFM and FM at the base temperature near the boundary. The phase separation of AFM and

FM state or paramagnetic (PM) state was observed in very large range of oxygen content from 2.82 to 2.89.

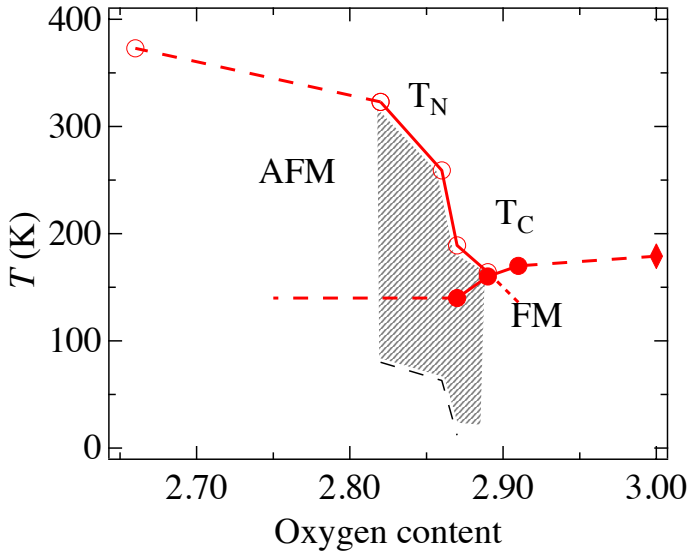

Fig. 3.5.1. Phase diagram for $La_{0.5}Ba_{0.5}CoO_{3-x}$. T_N for oxygen content 3.0 is from reference [81]. AFM and FM represent antiferromagnetic state and ferromagnetic state, respectively. The shadow area represents the range of phase separation.

3.6 Relation of NTE and magnetic ordering

Fig. 3.6.1 show the temperature dependence of experimental and calculated unit cell volumes for the sample $La_{0.5}Ba_{0.5}CoO_{3-x}$ (x=0.09, 0.11, 0.13, 0.14 and 0.18). The experimental volume is determined through Rietveld refinement on high resolution-neutron-powder diffraction data. The calculated volume is based on the Debye-Grüneisen model [85] which represents the phonon contribution. To fit the temperature dependence of the unit cell volume, the following Debye-Grüneisen formula was used:

$$V = V_{0,0}\left(1 + \frac{E(T)}{Q - bE(T)}\right), \qquad Q = \frac{V_{0,0}B_{0,0}}{\gamma}$$

$$b = \frac{1}{2}\left(B'_{0,0} - 1\right)$$

where $V_{0,0}$ is the unit cell volume at base temperature and ambient pressure, γ is a so-called Grüneisen parameter, $B_{0,0}$ is the bulk modulus, $B'_{0,0}$ is the pressure derivative of the bulk

modulus and $E(T)$ is the total phonon energy at a given temperature. I can fit the data with the following parametersV_0 = 58.25Å, θ_d = 300K, Q = 0.395*10^{-17}J and b = 1.5. The difference between experimental and calculated volumes reflects the magnetic contribution. The volumetric order parameter ΔV is calculated by subtracting the phonon contribution from the experimental volume, shown in Fig. 3.6.1(d). The temperature dependence of magnetic moment is shown in Fig. 3.6.2(a). As presented in Fig. 3.6.2(b), the data can be fitted by the linear formula:

$$\Delta V = k \times |M|^2 + \Delta V_0$$

where k = 0.266(3) and ΔV_0 = 0.051(4). The volumetric order parameter ΔV shows a good linear correlation with the square of magnetic moment M, which indicates that the NTE is intimately related to the spontaneous magnetic ordering, known as the magnetovolume effect (MVE) [1, 86]. It is worthwhile to notice that the ΔV is not 0 when $|M| = 0$. This may relate to the short range ordering. Since the short range ordering affects the bonding and leads to the inharmonious of lattice constant.

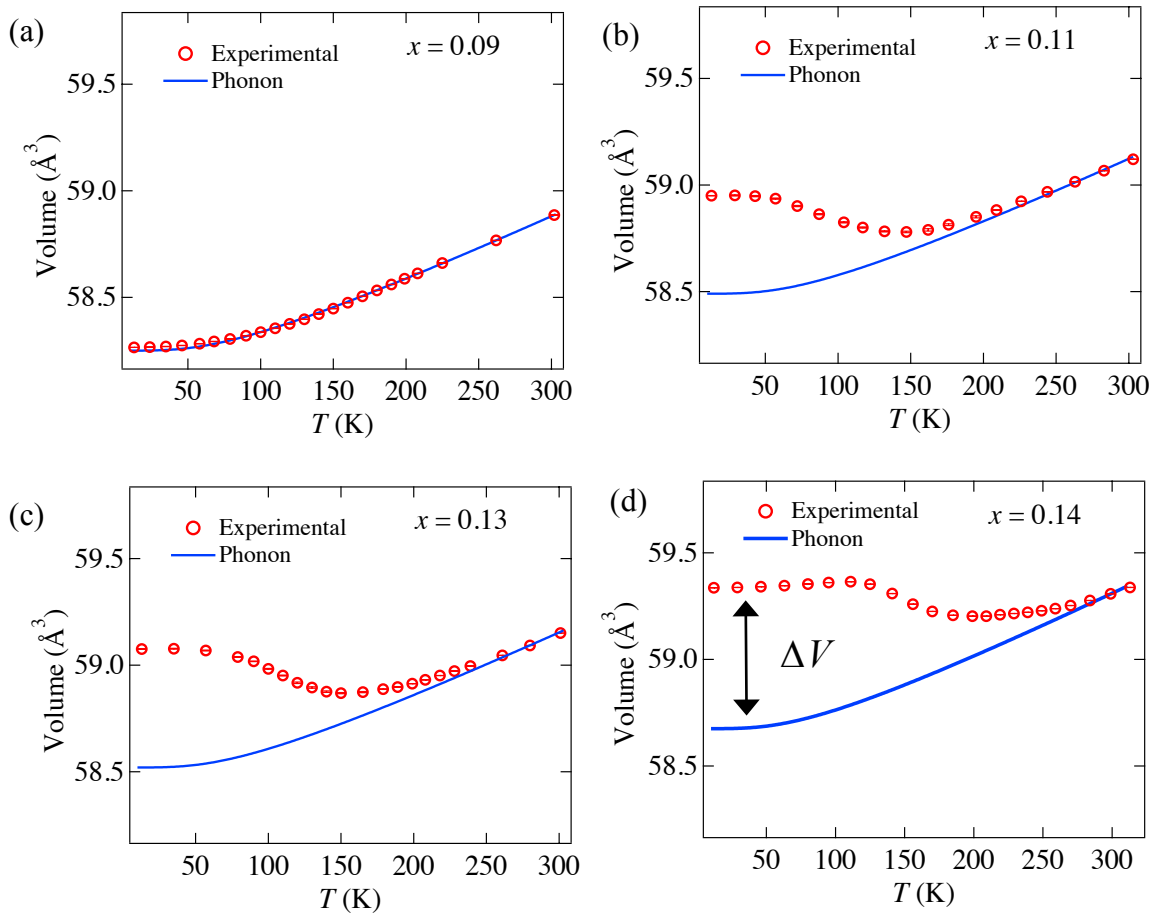

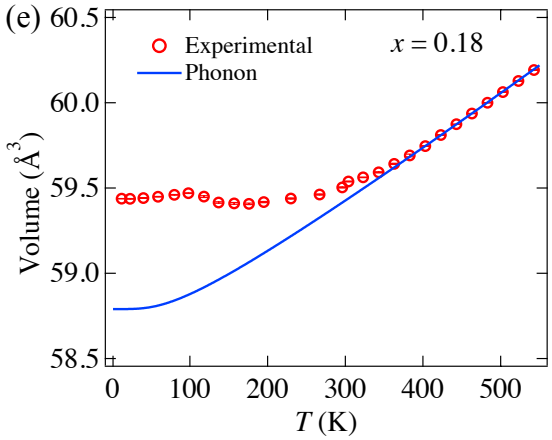

Fig. 3.6.1. The temperature dependence of experimental and calculated unit cell volumes for the sample $La_{0.5}Ba_{0.5}CoO_{3-x}$ (x=0.09, 0.11,0.13, 0.14 and 0.18).

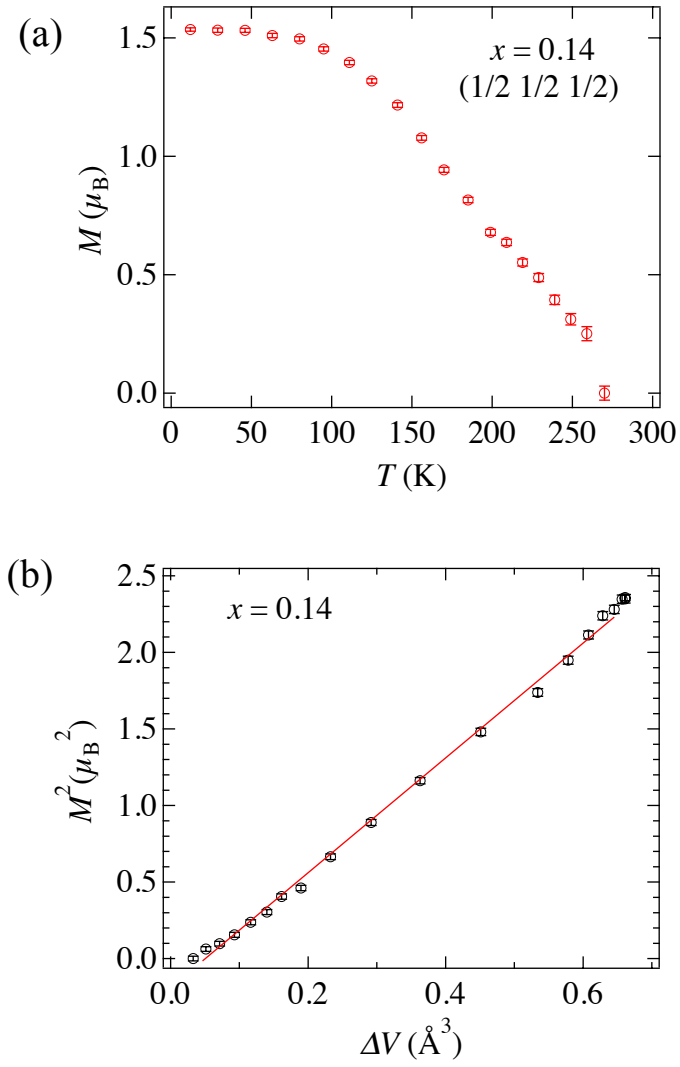

Fig. 3.6.1. (a) Temperature dependence of magnetic moment. (b) The square of the magnetic moment M as a function of the volumetric order parameter ΔV.

3.7 Effect of high magnetic field

We observed strong negative thermal expansion (NTE) in $La_{0.5}Ba_{0.5}CoO_{3-x,}$ which is triggered by changing the oxygen conten. We find this NTE is coupled with the spontaneous antiferromagnetic ordering, which is known as the magnetovolume effect (MVE). And we consider this MVE is closely origin from the transition of LV phase with antiferromagnetic (AFM) to SV phases with the ferromagnetic (FM). Therefore, it is worthwhile to study the magnetism of $La_{0.5}Ba_{0.5}CoO_{3-x}$ under magnetic field which can change the strength of competition between FM and AFM. In this research, we investigate the crystal and magnetic structures by the high-resolution neutron powder diffractometer with newly installed 14 T magnet.

The layered perovskites sample $La_{0.5}Ba_{0.5}CoO_{3-x}$ (x = 0.13) was used to perform the NPD measurement under magnetic field. In this experiment, we first collected the field dependence of diffraction pattern after zero field cooling (ZFC) at 100 K. Then, the temperature dependences of NPD measurements were performed under 14T.

From the result in chapter 2, the Neel temperature (T_N) of x = 0.13 sample is 200 K, so at 100K the sample is in the AFM state. In the NPD pattern of $La_{0.5}Ba_{0.5}CoO_{3-x}$ (x = 0.13) at T = 100 K and H = 0, we observed the superlattice reflections (0.5 0.5 1.5), as shown in Fig. 3.7.1(a), which signifies the AFM magnetic ordering. The magnetic structure has been determined as the G-type AFM structure with propagation vector $\boldsymbol{k}$ = (1/2 1/2 1/2), in which every Co ion spin aligns antiparallelly with the nearest Co neighbors, as shown in Fig. 3.7.1(d). It is hard to distinguish the spin direction because the crystal structure is cubic structure.

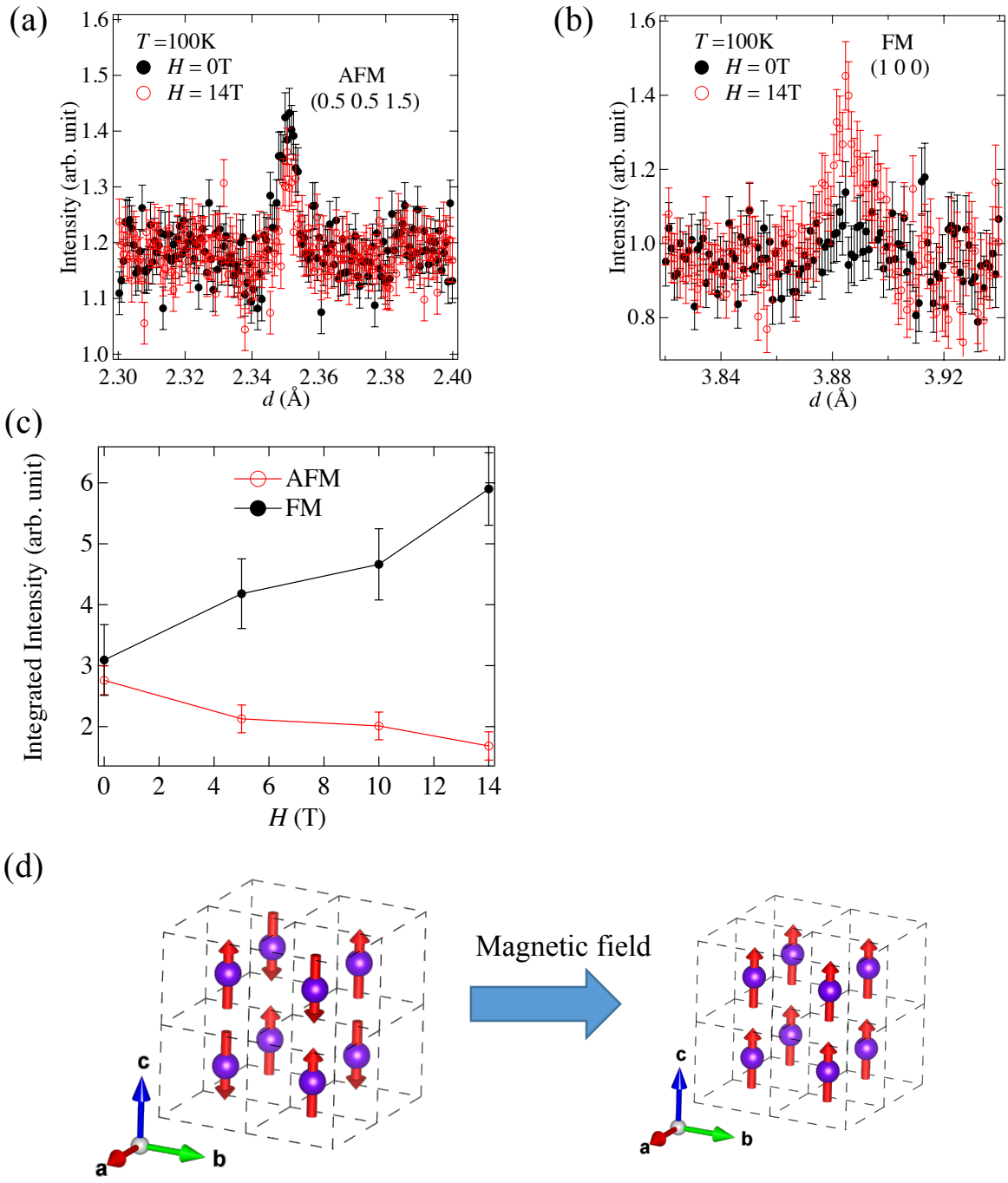

Fig. 3.7.1. The NPD patterns of $La_{0.5}Ba_{0.5}CoO_{3-x}$ (x = 0.13) around (a) AFM peaks and (b) F peaks under 0 T and 14 T at 100 K. The NPD profiles of (c) The integrated intensity of AFM and FM reflection as a function of magnetic field. (d) G-type AFM structure model (left) and FM structure model (right).

Upon applying 14 T magnetic field at T = 100 K, the magnetic reflections [see Fig. 3.7.1(a)] (0.5 0.5 1.5) decrease, suggesting that the AFM order is suppressed. Meanwhile, as shown in Fig. 3.7.1(b), the intensity of reflections (1 0 0) significantly increase under the 14 T magnetic

field. Compared to Fig. 3.7.1(c), we can conclude that the large volume (LV) phase is related to the AFM and small volume (SV) phase is related to the FM. According to discuss in section 3.2, the intensity increase in (1 0 0) correspond to a simple FM ordering with all the Co-ion spins pointing along the same direction [see Fig. 3.7.1(d)]. The integrated intensity of AFM and FM reflection as a function of magnetic field is presented in 3.7.1(d), which shows the AFM increases while the FM decreases as the field increase. Therefore, we draw the conclusion that in x = 0.13 sample, the 14 T magnetic field induces the AFM-to-FM phase transition at T = 100 K. We could not determine the spin direction because the spin orientations with respect to the nuclear crystal lattice from different powder grains are intrinsically inhomogeneous under magnetic field.

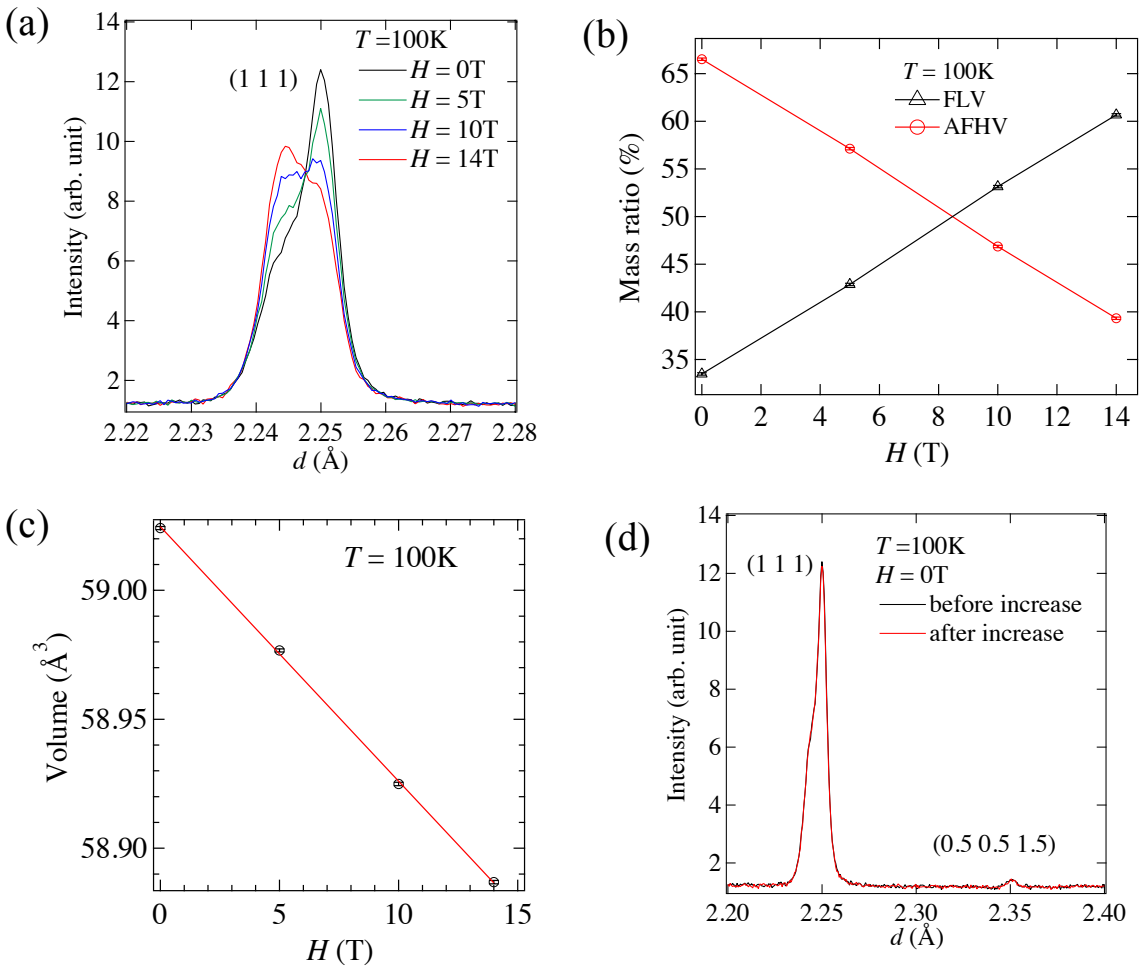

Fig. 3.7.2. (a) The NPD patterns of $La_{0.5}Ba_{0.5}CoO_{3-x}$ (x = 0.13) around nuclear reflection (1 1 1). (b) Mass ration of FSV and AFLV as a function of magnetic field at 100 K. (c) Field dependence of the average unit cell volume. (d) The NPD patterns of $La_{0.5}Ba_{0.5}CoO_{3-x}$ (x = 0.13) collected before increase field and after decrease field at H = 0 T.

In addition to the change of magnetic structure under magnetic field, we also observed that the crystal lattice is contracted. As shown in Fig. 3.7.2(a) and (b), the ratio of large volume phase with AFM (AFLV) decrease while the ratio of small volume phase with FM (FSV) increase as the field increase. This leads to the average unit cell volume decrease as the field increase. The average unit cell volume is calculated by $V_{average} = R_{LV} \times V_{LV} + R_{SV} \times V_{SV}$, where R is the mass ratio as shown in the Fig. 3.7.3(b). By fitting the data, the correlation of $V_{average}$ and magnetic field H is as follow:

$V_{average} = 59.025\text{-}0.0099 * H$

At H = 34T, we can get $V_{average} = V_{SV} = 58.6883$ Å^3. This reveals that the LV phase will convert into SV phase completely under about 34T magnetic field. Fig. 3.7.3(d) shows the NPD patterns of $La_{0.5}Ba_{0.5}CoO_{3-x}$ (x = 0.13) collected before increase field and after decrease field at H = 0 T. The two patterns overlap with each. This reveal that this process is reversible.

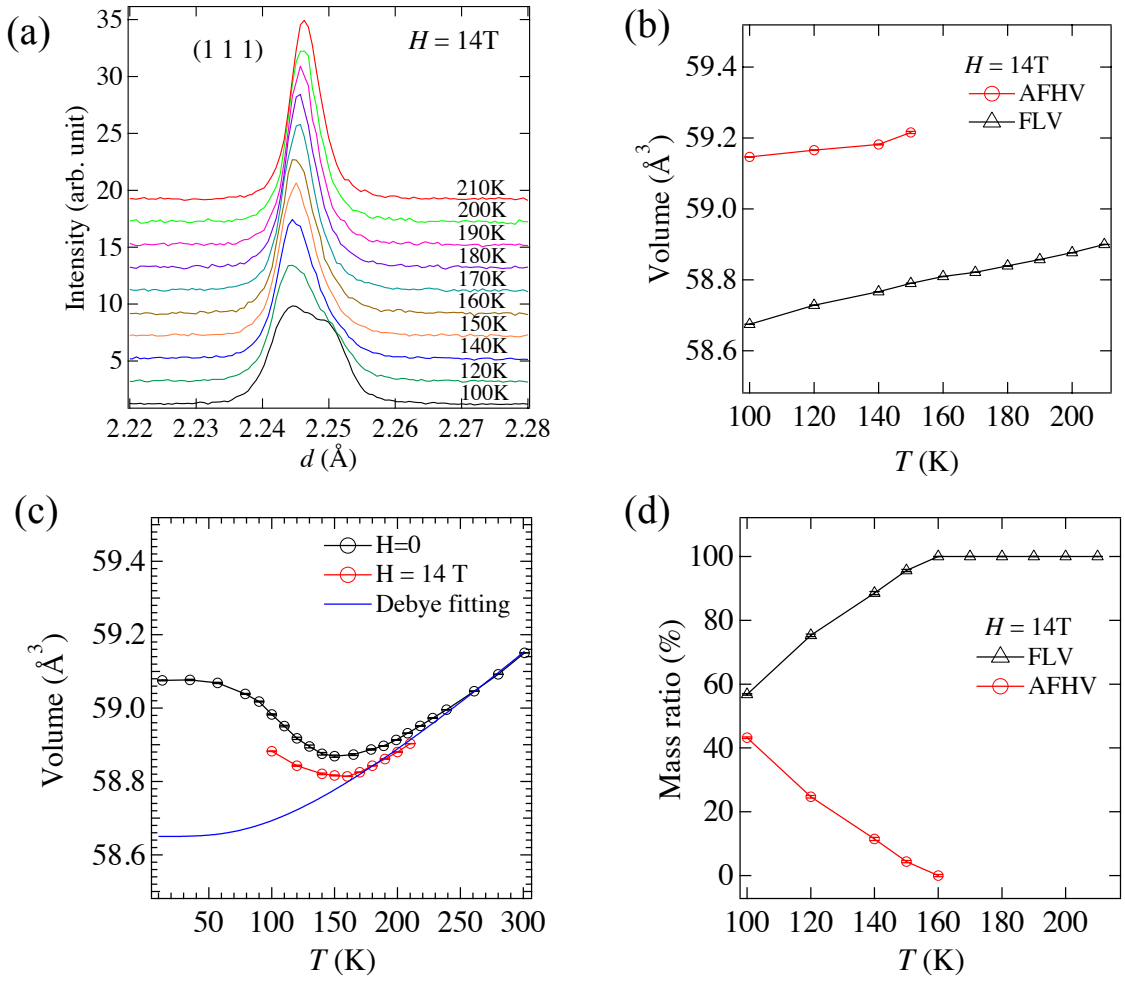

Fig. 3.7.3 (a) Temperature dependence of the NPD patterns of $La_{0.5}Ba_{0.5}CoO_{3-x}$ (x = 0.13) around nuclear reflection (1 1 1). (b) Unit cell volume of FSV and AFLV as a function of temperature under 14 T. (c) The temperature dependence of experimental (blue and red line) and calculated unit cell volumes. The solid blue line represents the anharmonic phonon contribution to thermal expansion. (d) Mass ration of FSV and AFLV as a function of temperature under 14T.

The nuclear reflection (1 1 1) of NPD patterns for $La_{0.5}Ba_{0.5}CoO_{3-x}$ (x = 0.13) at different temperatures are shown in Fig. 3.7.3 (a). The ratio of large volume phase with AFM (AFLV) decrease while the ratio of small volume phase with FM (FSV) increase as the field increase. This leads to the average unit cell volume decrease as the temperature increase. The NTE still can observed initiating at about 170K upon cooling under 14 T. However, compared with the temperature dependence of the unit cell volume at 0 T, which shows the NTE initiates around 230 K upon cooling, we found that the NTE is suppressed much under 14 T magnetic field.

It has been confirmed that at base temperatures the long-range ordered AFM matrix coexists with the short-range ordered FM clusters in $La_{0.5}Ba_{0.5}CoO_{3-x}$ (x = 0.13). The current study suggests that upon applying the magnetic field, the FM clusters start to grow in size at the expense of AFM clusters until the AFM phase disappear thoroughly. The 14 T field does not suffice to fully flip the AFM spins into the FM ones at 100 K, so additional energy is required to fulfill the phase transition. For example, at T = 160 K and H = 14 T, the AFM ordering is completely suppressed with the help of thermal energy.

According to our previous discovery, the NTE at x = 0.13 is coupled with the AFM ordering despite of the existence of FM clusters. The results from magnetic-field study suggest that the NTE may become less robust when the AFM spins are flipped into the FM structure, *i.e.*, the MVE is presumably much weaker under FM ordering. From this study, we found that applying magnetic field can significantly strengthen the FM order, so we are pursuing further study to specify the magnetic-filed effect on the MVE and clarify the underlying mechanism.

In summary, we investigate the magnetic property of $La_{0.5}Ba_{0.5}CoO_{3-x}$ (x = 0.13) by high resolution NPD with a newly installed 14 T magnet. By analyzing the NPD data, we find the magnetic field induces the AFM-FM transition at base temperatures, suggesting the energy of AFM and FM phases is comparable to each other. We also find that NTE is suppressed under magnetic field, which reveals that the NTE can be tune by the magnetic field.

4 Discussion

4.1 Phase diagram in $La_{0.5}Ba_{0.5}CoO_{3-x}$ and $Pr_{0.5}Ba_{0.5}CoO_{3-x}$

The phase diagrams of A-site disordered $La_{0.5}Ba_{0.5}CoO_{3-x}$ and A-site ordered $Pr_{0.5}Ba_{0.5}CoO_{3-x}$ are shown in Fig. 4.1.1. Compare with the phase diagram of the two samples, we can see, at low oxygen content, the ground state of the two samples is AFM state. At high oxygen content, the ground state of the two samples is FM state. Near the boundary of the AFM and FM state, both of the two samples show the coexistent of the AFM and FM state at the base temperature.

In $Pr_{0.5}Ba_{0.5}CoO_{3-x}$ the phase separation only occurs at around 2.875. However, in $La_{0.5}Ba_{0.5}CoO_{3-x}$ the phase separation is observed in much larger range of oxygen content from 2.82 to 2.89. And also we can see that the T_C of the 2 sample is very close. However, the T_N of $La_{0.5}Ba_{0.5}CoO_{3-x}$ is much high than T_N of $Pr_{0.5}Ba_{0.5}CoO_{3-x}$. The phase diagram shows large difference between the two samples. It may come from the different radius of La and Pr. It is also possible from the A-site disordered effect. Further study is necessary to clarify the origin of the large difference in phase diagram between these two samples.

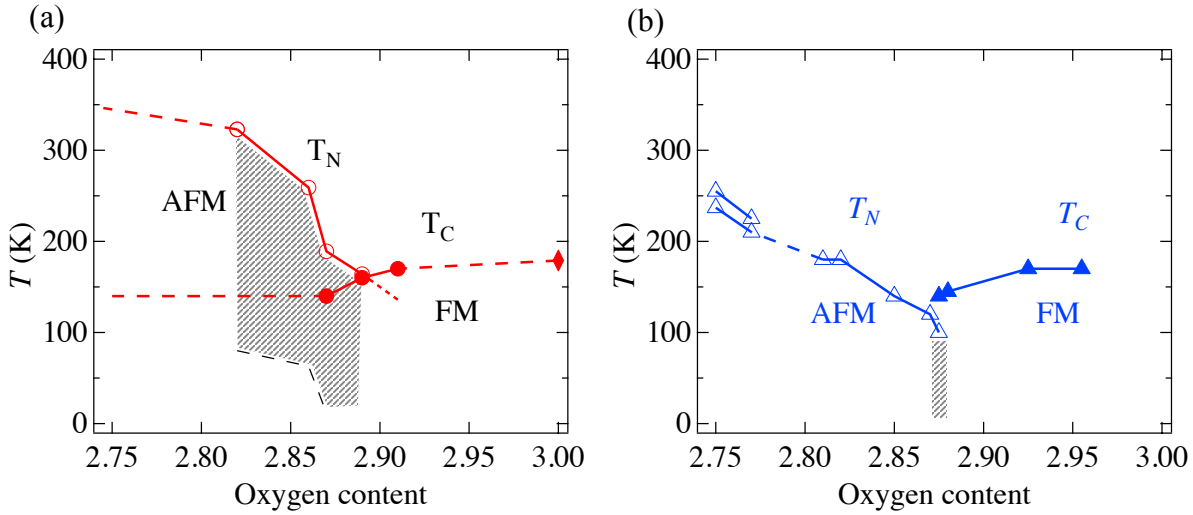

Fig. 4.1.1. Phase diagram for (a) $La_{0.5}Ba_{0.5}CoO_{3-x}$ and (b) $Pr_{0.5}Ba_{0.5}CoO_{3-x}$. AFM and FM represent antiferromagnetic state and ferromagnetic state, respectively. The shadow area represents the range of phase separation.

4.2 $\Delta V_{LV\text{-}SV}/V$ in $La_{0.5}Ba_{0.5}CoO_{3-x}$ and $Pr_{0.5}Ba_{0.5}CoO_{3-x}$

Compare the phase separation of this 2 samples I found that the relative difference of volume between the LV and SV in $La_{0.5}Ba_{0.5}CoO_{3-x}$ is much large than that in $Pr_{0.5}Ba_{0.5}CoO_{3-x}$. The relative difference of volume between the LV and SV in $La_{0.5}Ba_{0.5}CoO_{3-x}$ is about 1.2% while that of $Pr_{0.5}Ba_{0.5}CoO_{3-x}$ is about 0.4%. As mention above, the LV is related to the AFM. The SV is related to the FM. From the Table 4.2.1, we can see that the difference of volume in AFM phase between these two samples is much larger than the difference of volume in FM phase between the two samples. It suggests that the much larger $\Delta V_{LV\text{-}SV}/V$ in $La_{0.5}Ba_{0.5}CoO_{3-x}$ is mainly from the much larger difference of unit cell volume in the AFM between the $La_{0.5}Ba_{0.5}CoO_{3-x}$ and $Pr_{0.5}Ba_{0.5}CoO_{3-x}$. On the other hand, from the phase diagram, we can see that the T_C of the two samples is very close. However, the T_N in $La_{0.5}Ba_{0.5}CoO_{3-x}$ is much high than that of $Pr_{0.5}Ba_{0.5}CoO_{3-x}$. All of these suggest that the much larger $\Delta V_{LV\text{-}SV}/V$ is related to the much stronger AFM in $La_{0.5}Ba_{0.5}CoO_{3-x}$.

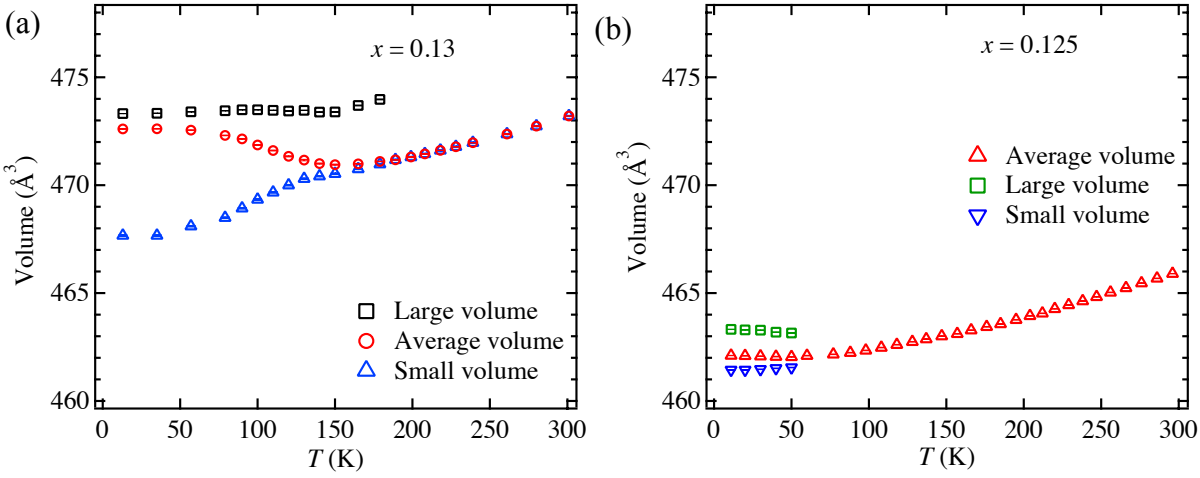

Fig. 4.2.1. The temperature dependence of unit cell volumes for (a) A-site disordered $La_{0.5}Ba_{0.5}CoO_{3-x}$ (x = 0.13) and A-site ordered $Pr_{0.5}Ba_{0.5}CoO_{3-x}$ (x = 0.125).

Table 4.2.1. The volume of unit cell $2a_p \times 2a_p \times 2a_p$ at 10K.

	LV(AFM)	SV(FM)
$La_{0.5}Ba_{0.5}CoO_{3-x}$	473.4	467.7
$Pr_{0.5}Ba_{0.5}CoO_{3-x}$	463.3	461.5
Difference	10.1	6.2

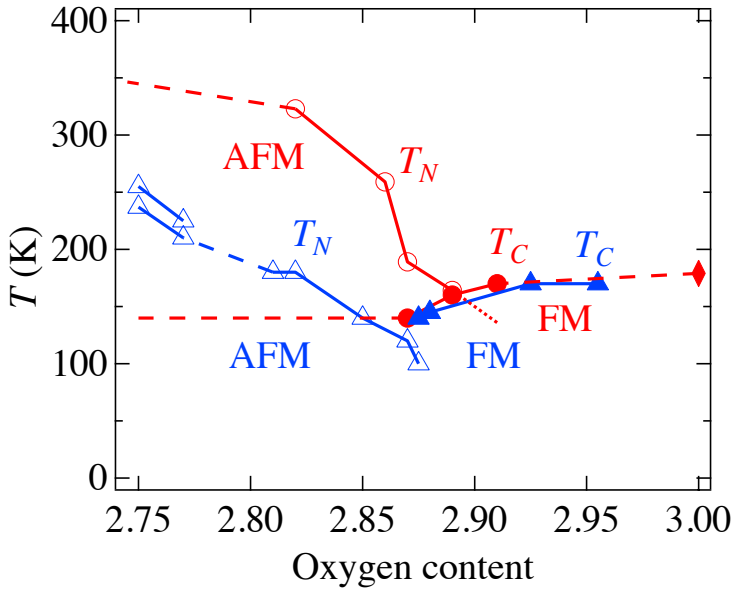

Fig. 4.2.2. Phase diagram for $La_{0.5}Ba_{0.5}CoO_{3-x}$ (red symbol and line) and (b) $Pr_{0.5}Ba_{0.5}CoO_{3-x}$ (blue symbol and line). AFM and FM represent antiferromagnetic state and ferromagnetic state, respectively.

4.3 β in $La_{0.5}Ba_{0.5}CoO_{3-x}$ and $Pr_{0.5}Ba_{0.5}CoO_{3-x}$

The thermal expansion coefficients of volume β as a function of temperature for (a) A-site disordered $La_{0.5}Ba_{0.5}CoO_{3-x}$ and A-site ordered $Pr_{0.5}Ba_{0.5}CoO_{3-x}$ are shown in Fig. 4.3.1. In both of the samples the largest β is occurred at around $x = 0.13$. The largest -β in $La_{0.5}Ba_{0.5}CoO_{3-x}$ is

about 5.7 x 10^{-5} K^{-1}. The largest -β in $Pr_{0.5}Ba_{0.5}CoO_{3-x}$ is about 3.6 x 10^{-5} K^{-1}. The β of $La_{0.5}Ba_{0.5}CoO_{3-x}$ is much larger than that of $Pr_{0.5}Ba_{0.5}CoO_{3-x}$, even though the temperature window of NTE in $La_{0.5}Ba_{0.5}CoO_{3-x}$ is much wider than that in $Pr_{0.5}Ba_{0.5}CoO_{3-x}$. This is attributed to the much larger $\Delta V_{LV\text{-}SV}/V$ in $La_{0.5}Ba_{0.5}CoO_{3-x}$.

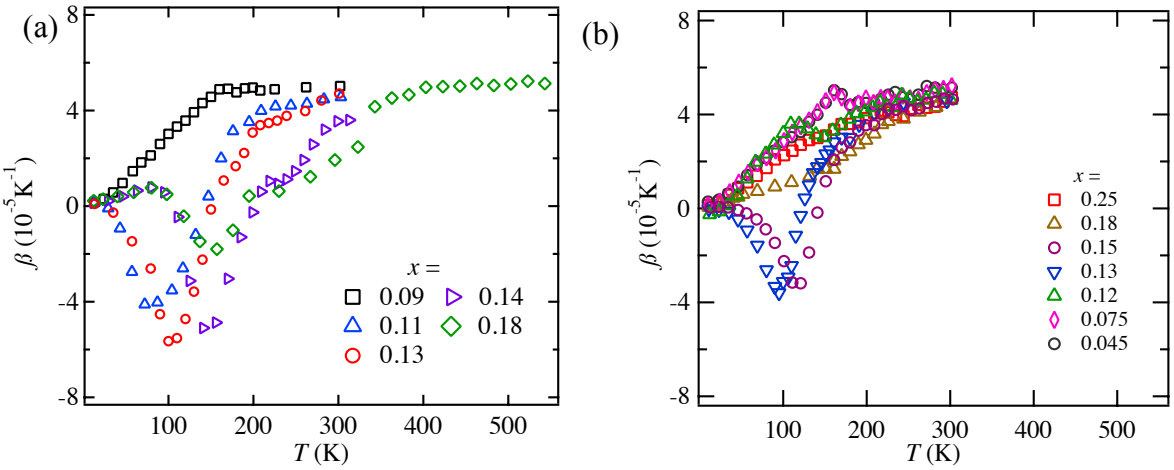

Fig. 4.3.1. The thermal expansion coefficient of volume as a function of temperature for (a) A-site disordered $La_{0.5}Ba_{0.5}CoO_{3-x}$ and (b) A-site ordered $Pr_{0.5}Ba_{0.5}CoO_{3-x}$.

Table 4.3.1. The NTE property of A-site disordered $La_{0.5}Ba_{0.5}CoO_{3-x}$ and A-site ordered $Pr_{0.5}Ba_{0.5}CoO_{3-x}$

$x = 0.13$	$La_{0.5}Ba_{0.5}CoO_{3-x}$	$Pr_{0.5}Ba_{0.5}CoO_{3-x}$
NTE range	50 – 140K	60 – 120K
Largest β	-5.7 x 10^{-5} K^{-1}	-4.0 x 10^{-5} K^{-1}
$\Delta V_{LV\text{-}SV} / V$	1.2%	0.4%

5 Summary and outlook

I prepared high quality $La_{0.5}Ba_{0.5}CoO_{3-x}$ polycrystalline samples by solid-state reaction method and controlled the oxygen content by annealing as-synthesized sample in pure Ar atmosphere at various temperatures. A combination of X-ray powder diffraction (XRD), neutron powder diffraction (NPD) and the superconducting quantum interference device (SQUID) magnetometer (MPMS) was used to investigate the crystal structure and magnetic structure. The crystal structure and magnetic structure are determined by the Z-Rietveld refinement. From the temperature dependence of volume, we observed large NTE in the A-site disordered $La_{0.5}Ba_{0.5}CoO_{3-x}$. This NTE can be tuned by changing the oxygen content and the strongest NTE occurs near the boundary between FM and AFM phases in the phase diagram. The phase separation was observed, which reveal the energy of AFM and FM states is very close. We found that this NTE is related to the magnetic ordering. The AFM to FM or paramagnetic (PM) phase transition results in the transition of large volume to small volume phases, which leads to the NTE. Especially, low thermal expansion (or almost ZTE) is observed in the sample x = 0.18 with a large temperature window from 13K to room temperature.

Since this NTE is related to the magnetic ordering, it is important to further study the mechanism of NTE in $La_{0.5}Ba_{0.5}CoO_{3-x}$ by changing the magnetic structure by magnetic field. We success to change the magnetic structure of $La_{0.5}Ba_{0.5}CoO_{3-x}$ by applying magnetic field. We investigate the magnetic property of $La_{0.5}Ba_{0.5}CoO_{3-x}$ (x = 0.13) by high resolution NPD with a newly installed 14 T magnet. By analyzing the room-temperature NPD data, we find the magnetic field induces the AFM-FM transition at base temperatures, suggesting the energy of AFM and FM phases is comparable to each other. We also find that NTE is suppressed under magnetic field, which reveals that the NTE can be tune by the magnetic field.

From the phase diagram of $La_{0.5}Ba_{0.5}CoO_{3-x}$ and $Pr_{0.5}Ba_{0.5}CoO_{3-x}$, the phase diagram shows large differences in the two samples. It may come from the different radius of La and Pr or from the A-site disordered effect. I also found that the relative difference of volume between the LV and SV ($\Delta V_{LV\text{-}SV}/V$) in $La_{0.5}Ba_{0.5}CoO_{3-x}$ is much larger than that in $Pr_{0.5}Ba_{0.5}CoO_{3-x}$. From the phase diagram and the analysis of the volume in AFM and FM phase between these two samples, it is suggested that the much larger $\Delta V_{LV\text{-}SV}/V$ is related to the much stronger AFM in $La_{0.5}Ba_{0.5}CoO_{3-x}$.

In the future work, the following research plans are being expected to be performed.

Firstly, since the temperature window of the phase transition from LVP to SVP become larger and move to higher temperature as the oxygen content decreases, it is possible to find NTE/ZTE above room temperature with large temperature window by further increasing the x value. And for practical use, ZTE/NTE with temperature window above room temperature is of importance, therefore, we expect to find NTE above room temperature.

Secondly, in order to clarify the origin of the large difference in phase diagram between A-side ordered and disordered cobaltite perovskites, a comprehensive investigation of crystal structures and magnetic structures of the A-site ordered $LaBaCo_2O_{6-2x}$ samples would be desired. I expect to establish the phase diagram of $LaBaCo_2O_{6-2x}$ and compare with that of $La_{0.5}Ba_{0.5}CoO_{3-x}$. My ultimate goal is to obtain deeper understanding of the microscopic origin of NTE in this cobaltite.

References

[1] J. Chen, L. Hu, J. Deng, X. Xing, *Chem. Soc. Rev.* 2015, 44, 3522-3567.

[2] G. D. Barrera, J. A. O. Bruno, T. H. K. Barron, N. L. Allan, *J. Phys.: Condens. Matter*, 2005, 17, R217 - R252.

[3] P. Miao, X. Lin, A. Koda, S. Lee, Y. Ishikawa, S. Torii, M. Yonemura, T. Mochiku, H. Sagayama, S. Itoh, K. Ikeda, T. Otomo, Y. Wang, R. Kadono, and T. Kamiyama, *Adv. Mater.*, 2017, 29, 1605991.

[4] Y. Tokura, Rep. Prog. Phys. 69 (2006) 797–851.

[5] C. Kittel, Introduction to Solid State Physics, 8th edition, John Wiley and Sons, New York 2004.

[6] C. L. Rathmann, G. H. Mann, and M. E. Nordberg, *Appl. Opt*. 1968, 7, 819.

[7] Y. Namba, H. Takehara, and Y. Nagano, *Ann. CIRP*. 2001, 50, 239.

[8] Z. C. Du, M. R. Zhu, Z. G. Wang, and J. G. Yang, *Compos. Struct*. 2016, 152, 693.

[9] R. Roy, D. K. Agrawal and H. A. Mckinstry, *Annual Review of Materials Science*,1989, 19, 59-81.

[10] Taylor, R. E. Thermal expansion of solids, *ASM International*,1998.

[11] R. S. Krishnan, R. Srinivasan, S. Devanarayanan, Thermal expansion of crystals, *Pergamon press: Oxford*, 1979.

[12] P. Mohn, *Nature*, 1999, 400, 18-19.

[13] C. E. Guillaume, C. R. Hebd. *Seances Acad. Sci.*, 1897, 125, 235.

[14] F. A. Hummel. *Journal of the American Ceramic Society*, 1951, 34, 235-239.

[15] A. W. Sleight *Inorg. Chem.*, 1998, 37 2854

[16] T. A. Mary, J. S. Evans, T. Vogt, A. W. Sleight, *Science* 1996**,** 272, 90.

[17] J. S. O. Evans, T. A. Mary, T. Vogt, M. A. Subramanian and A. W. Sleight, *Chem. Mater.*, 1996, 8, 2809

[18] A. K. A. Pryde, K. D. Hammonds, M. T. Dove, V. Heine, J. D. Gale and M. C. Warren, *J. Phys.: Condens. Matter*, 1996, 8, 10973.

[19] M. Azuma, K. Oka and K. Nabetani, *Sci. Technol. Adv. Mater.*, 2015, 16, 034904.

[20] J. S. O. Evans, Z. Hu, J. D. Jorgensen, D. N. Argyriou, S. Short, A. W. Sleight. Compressibility, Phase Transitions, and Oxygen Migration in Zirconium Tungstate, ZrW2O8. *Science*, 1997, 275:61.

[21] B. K. Greve, K. L. Martin, P. L. Lee, P. J. Chupas, K. W.Chapman and A. P. Wilkinson, *J. Am. Chem. Soc.*, 2010, 132, 15496.

[22] J. P. Attfield, *Nature*, 2011, 480, 465.

[23] C. R. Morelock, B. K. Greve, L. C. Gallington, K. W. Chapman and A. P. Wilkinson, *J. Appl. Phys.*, 2013, 114, 213501.

[24] J. S. O. Evans, *J. Chem. Soc.*, Dalton Trans., 1999, 3317.

[25] A. E. Phillips, A. L. Goodwin, G. J. Halder, P. D. Southon and C. J. Kepert, *Angew. Chem. Int. Edn Engl.*, 2008, 47, 1396.

[26] J. Chen, X. R. Xing, R. B. Yu and G. R. Liu, *J. Am. Ceram. Soc.*, 200, 88, 1356.

[27] J. Chen,X. Xing, C. Sun, P. Hu, R. Yu, X. Wang and L. Li, *J. Am. Chem. Soc.*, 2008, 130, 1144.

[28] P. Hu, H. Kang, J. Chen, J. Deng and X. Xing, *J. Mater. Chem.*, 2011, 21, 16205.

[29] J. Chen, K. Nittala, J. S. Forrester, J. L. Jones, J. Deng, R. Yu and X. Xing, *J. Am. Chem. Soc.*, 2011, 133, 11114.

[30] J. Chen, L. Fan, Y. Ren, Z. Pan, J. Deng, R. Yu and X. Xing, *Phys. Rev. Lett.*, 2013, 110, 115901.

[31] J. Chen, F. Wang, Q. Huang, L. Hu, X. Song, J. Deng, R. Yu and X. Xing, *Sci. Rep.*, 2013, 3, 2458.

[32] Y. W. Long, N. Hayashi, T. Saito, M. Azuma, S. Muranaka and Y. Shimakawa, *Nature*, 2009, 458, 60.

[33] Y. W. Long and Y. Shimakawa. *New J. Phys.*, 2010, 12, 063029.

[34] I. Yamada, S. Marukawa, M. Murakami and S. Mori. *Appl. Phys. Lett.*, 2014, 105, 231906.

[35] I. Yamada, K. Siro, K. Oka, M. Azuma and T. Irifune. *J. Ceram. Soc. Japan*, 2013, 121, 912.

[36] I. Yamada, K. Tsuchida, K. Ohgushi, N. Hayashi, J. G. Kim, N. Tsuji, R. Takahashi, M. Matsushita, N. Nishiyama, T. Inoue, T. Irifune, K. Kato, M. Takata and M. Takano. *Angew. Chem.*, Int. Ed., 2011, 50, 6579.

[37] R. J. Weiss, *Proc. Phys. Soc.*, 1963, 82, 281.

[38] T. Moriya, & K. Usami, *Solid State Commun.*, 1980, 34, 95.

[39] M. Hayase, M. Shiga and Y. Nakamura, *J. Phys. Soc. Japan* 1973, 34, 925

[40] K. Takenaka and H. Takagi, *Appl. Phys. Lett.*, 2005, 87, 261902.

[41] K. Takenaka, K. Asano, M. Misawa and H. Takagi, *Appl. Phys. Lett.*, 2008, 92, 011927.

[42] C. Wang, L. H. Chu, Q. R. Yao, Y. Sun, M. M. Wu, L. Ding, J. Yan, Y. Y. Na, W. H. Tang, G. N. Li, Q. Huang and J. W. Lynn, *Phys. Rev. B: Condens. Matter Mater. Phys.*, 2012, 85, 220103.

[43] R. Fruchart, R. Madar, M. Barberon, E. Fruchart and M. G. Lorthioir, *J. Phys. (Paris)*, 1971, 32, C1-982

[44] S. Iikubo, K. Kodama, K. Takenaka, H. Takagi and S. Shamoto, *Phys. Rev. B*, 2008, 77, 020409.

[45] K. Takenaka, *Sci. Technol. Adv. Mater.*, 2012 13, 013001.

[46] D. Tahara, Y. Motome and M. Imada, *J. Phys. Soc. Japan*, 2007, 76, 013708.

[47] B. Qu, H. He and B. Pan, AIP ADVANCES, 2016, 6, 075122.

[48] R. Mahendiranand, A. K. Raychaudhuri, *Phys. Rev. B*, 1996, 54, 16044.

[49] M. Kriener, M. Braden, H. Kierspe, D. Senff, O. Zabara, C. Zobel, and T. Lorenz, *Phys. Rev. B*, 2009, 79, 224104.

[50] M. A. Señarís-Rodriguez and J. B. Goodenough, *J. Solid State Chem.*, 1995, 116, 224.

[51] T. Saitoh, T. Mizokawa, A. Fujimori, M. Abbate, Y. Takeda, and M. Takano, *Phys. Rev. B*, 1997, 55, 4257.

[52] K. Asai, A. Yoneda, O. Yokokura, J. M. Tranquada, G. Shirane, and K. Kohn, *J. Phys. Soc. Jpn.*, 1998, 67, 290.

[53] A. Maignan, C. Martin, D. Pelloquin, N. Nguyen, and B. Raveau, *J. Solid State Chem.*, 142, (1999) 247.

[54] F. Fauth, E. Suard, V. Caignaert and I. Mirebeau, *Phys. Rev. B*, 2002, 66, 184421.

[55] C. Frontera, J. L. García-Muñoz, A. Llobet, and M. A. G. Aranda, *Phys. Rev. B*, 2002, 65, 180405(R).

[56] J. L. García-Muñoz, C. Frontera, A. Llobet, A. E. Carrillo, A. Caneiro, M. A. G. Aranda, M. Respaud, C. Ritter and E. Dooryee, *J. Magn. Magn. Mater.*, 2004,272–276, 1762.

[57] D. Chernyshov, V. Dmitriev, E. Pomjakushina, K. Conder, M. Stingaciu, V. Pomjakushin, A. Podlesnyak, A. A. Taskin, and Y. Ando, *Phys. Rev. B*, 2008, 78, 024105.

[58] P. Miao, X. Lin, S. Lee, Y. Ishikawa, S. Torii, T. Ueno, N. Inami, K. Ono, Y. Wang, T. Kamiyama, *Phys. Rev. B*, 2017, 95, 125123.

[59] E. Dagotto, T. Hotta, A. Moreo, *Physics Reports*, 2011, 344, 1-153

[60] M. Kriener, M. Braden, H. Kierspe, D. Senff, O. Zabara, C. Zobel, and T. Lorenz, *Phys. Rev. B*, 2009,79, 224104.

[61] M. Kriener, C. Zobel, A. Reichl, J. Baier, M. Cwik, K. Berggold, H. Kierspel, O. Zabara, A. Freimuth, and T. Lorenz, *Phys. Rev. B*, 2004, 69, 094417.

[62] T. Nakajima, M. Ichihara, *Y. Ueda, J. Phys. Soc. Jpn.*, 2005, 74, 1572–1577.

[63] F. Fauth, E. Suard, and V. Caignaert, *Phys. Rev. B*, 2001, 65, 060401(R).

[64] V. Sikolenko, V. Efimov, I.O. Troyanchuk, D.V. Karpinsky, M.V. Bushinsky and D. Sheptyakov, *J. Phys. Conf. Ser.*, 2012, 391, 012106.

[65] I.O. Troyanchuk, M.V. Bushinsky, V. Sikolenko, V. Efimov, C. Ritter, T. Hansen, and D.M. Többens, *Eur. Phys. J. B*, 2013, 86, 435.

[66] I.O. Troyanchuk, D.V. Karpinsky, M.V. Bushinsky, V. Sikolenko, V. Efimov, A. Cervellino and B. Raveau, *J. Appl. Phys.*, 2012, 112, 013916.

[67] I. O. Troyanchuk, D. V. Karpinsky, M. V. Bushinsky, V. Sikolenko, V. Efimov, and A. Cervellino, *JETP Lett.*, 2011, 93, 139.

[68] H. Masuda, T. Fujita, T. Miyashita, M. Soda, Y. Yasui, Y. Kobayashi and M. Sato: *J. Phys. Soc. Jpn.*, 2003, 72, 873.

[69] D. L. Price, and K. Skold, Introduction to Neutron Scattering, *Methods in Experimental Physics*, Academic Press, 1986, 23(Part A), 1–97

[70] A. Furrer, J. Mesot and T. Strässle, Neutron scattering in condensed matter physics. *World Scientific*, Singapore, 2009.

[71] L. A. Feigin, D. I. Svergun and G. W. Taylor, Principles of the theory of X-ray and neutron scattering. In Structure Analysis by Small-Angle X-Ray and Neutron Scattering, *Springer*, Boston, 1987.

[72] T. Chatterji, Neutron scattering from magnetic materials. Gulf Professional Publishing, *Elsevier Science*, 2005.

[73] W. H. Bragg, W. L. Bragg, The reflection of X-rays by crystals, *Proc. R. Soc. Lond.* A, 1913,88(605), 428-438.

[74] A.-J. Dianoux, G. Lander, Neutron Data Booklet (Second Edition), *Institut Laue-Langevin*, Grenoble(France), 2003.

[75] E. H. Kisi and C. J. Howard, Applications of Neutron Powder Diffraction. *Oxford Univeristy Press*, New York, 2008.

[76] S. Torii, M. Yonemura, T. Y. S. P. Putra, J. Zhang, P. Miao, T. Muroya, R. Tomiyasu, T. Morishima, S. Sato, H. Sagehashi, Y. Noda and T. Kamiyama, *J. Phys. Soc. Jpn.*, 2011, 80, SB020.

[77] S. Torii, M. Yonemura, T. Y. S. P. Putra, J. Zhang, P. Miao, T. Muroya, R. Tomiyasu, T. Morishima, S. Sato, H. Sagehashi, Y. Nodai and T. Kamiyama, *J. Phys. Conf. Ser.*, 2014, 502, 012052.

[78] R. Oishi, M. Yonemura, Y. Nishimaki, S. Torii, A. Hoshikawa, T. Ishigaki, T. Morishima, K. Mori, and T. Kamiyama, *Nucl. Instrum. Methods Phys. Res.*, Sect. A, 2009, 600, 94.

[79] R. Oishi-Tomiyasu, M. Yonemura, T. Morishima, A. Hoshikawa, S. Torii, T. Ishigaki, and T. Kamiyama, *J. Appl. Crystallogr.*, 2012, 45, 299.

[80] J. RodrÌguez-Carvajal, *Physica B (Amsterdam, Neth.)*, 1993, 192, 55.

[81] E. Rautama, P. Boullay, A. K. Kundu, V. Pralong, M. Karppinen, B. Raveau, *Chem. Mater.*, 2008, 20, 2742.

[82] A. Wills, *Physica B (Amsterdam, Neth.)*, 2000, 278, 680. 18.

[83] Devendra Kumar and A Banerjee, *J. Phys.: Condens. Matter*, 2013, 25, 216005.

[84] B. A. Hunter, B. J. Kennedy and T. Vogt, *Phys. Rev. B*, 2004, 69, 020410.

[85] D. C. Wallace, Thermodynamics of crystals, Dover Pbulications, New York, 1998.

[86] Y. Takahashi, H. Nakano, *J. Phys. Condens. Matter*, 2006, 18, 521–556.

Acknowledgement

I would like to express my deep gratitude to all those who have offered cordial and selfless support in writing this thesis. Firstly, I am extremely grateful to my supervisor, Prof. Takashi Kamiyama. He guides me, influences me and helps me in the process of my PhD. research studies.

Secondly, I should give my hearty thanks to all the other faculty members for their patient instructions in various courses and their precious suggestions for my study here.

Thirdly, I would also like to thank Dr. Ping Miao, Dr. Masato Hagihara, Dr. Yoshihisa Ishikawa, Dr. Shuki Torii, and Dr. Sanghyun Lee for their kind support and advice. I also thank Namba Kaoru and Masahiro Shioya for their assistance during my experiments. I also greatly appreciate the assistance from all my colleagues, Widya Rika Puspita, Nur Ika Puji Ayu, Wu Peng, and Seungyub Song for providing me help during my experiment.

Finally, I also want to thank to my family, for their understanding and love in life.